Faculty of Engineering

University of Southern Denmark

Vibration-based SHM of a laboratory-scale wind turbine blade

Master thesis

Author:

Casper Aaskov Drangsfeldt

Supervisor:

Ass. Prof. Luis David Avendaño-Valencia

Version Number

February 6, 2023

Preface

The thesis is written by Casper Aaskov Drangsfeldt and is a part of the Master's program in Structural Engineering at the University of Southern Denmark. The thesis is based on the accessibility of experimental data of a laboratory-scale wind turbine blade. Therefore, gratitude for this work is acknowledged. Furthermore, the supervision from Luis David Avendaño-Valencia throughout the thesis was invaluable. Last, but not least, the author hopes the reader will find as much interest in reading the thesis as the author had during the work.

Casper Aaskov Drangsfeldt

Signature

Date

Abstract

The necessity of the green transition is today more extensive than ever before. Consequently, wind turbines along with wind farms are compelled to grow rapidly to encounter the obligation of a sustainable source of energy. Facing extensive expenses associated with maintenance, the exploration of a well-functional *Structural Health Monitoring* (SHM) system is crucial. Hence, by utilizing data from a laboratory-scale wind turbine blade in a controlled environment, numerous *Damage Sensitive Features* (DSFs) along with several techniques to mitigate the effect of *Environmental and Operational Variability* (EOV) are investigated. In this work, we consider DSFs originating from *Vector Auto-Regressive* (VAR) models, including natural frequencies and damping ratios as a physical quantity, and the parameters of the models as a non-physical quantity. The inevitable obscuring of the DSFs caused by EOV is mitigated by utilizing two distinct approaches. Bayesian non-linear regression models and the *Principal Component Analysis* (PCA) methodology, designated as an explicit and implicit approach respectively. In addition, a novel approach combining the implicit and explicit methodology is proposed. Through a comparative analysis, various considerations of interest were derived. The applicability of the various DSFs was measured in terms of correctly detected damages utilizing the multivariate squared Mahalanobis distance as a one-class classifier. The derivation was that the usage of the non-physical quantity did show prominent applicability. Generally, the combined implicit-explicit methodology showed superior efficiency. Despite the acknowledgement regarding complicating aspects entering an uncontrolled environment, the conviction of efficiency is preserved yet reduced to some extent.

Contents

List of Figures

Introduction

Nowadays wind farms are expanding while wind turbines are growing in size owing to the quest of sustainable energy sources. Additionally, the necessity for harvesting wind energy is forecasted to grow even more [16]. Typically, some of the best locations for harvesting wind energy are also some of the most remote locations, embracing offshore locations. Due to the remoteness of these locations, extensive expenses are associated with shutdowns. Therefore, the maintenance and service are tightly scheduled and established on experience. The objective of a meticulously thought out service and maintenance schedule is to minimize the cost associated with both transport and downtime. In addition, the profit is also enhanced by minimizing downtime. Yet, up to one-third of the energy cost is comprised by operation and maintenance costs including spare parts, repair costs and loss of production due to shutdowns [30]. While service and maintenance are carefully scheduled to enhance the probability of a well-functional wind turbine, the risk and cost of unexpected breakdown cannot be avoided. In this sense, the service and maintenance schedule of wind turbines can be optimized by implementing a *Structural Health Monitoring* (SHM) system [28, 24].

Providing and constructing an SHM system for an operating wind turbine comes along with a range of challenges. Among these challenges is the influence of environmental changes during monitoring [2]. A common strategy for constructing an SHM system is to trace any variability in the natural frequency of the structure. Structural damage will change the stiffness of the structure and thereby the natural frequency. In this sense, the natural frequency of a structure may be deemed as a *Damage Sensitive Feature* (DSF). [19, 26, 27]. Challenges arise, since the structural stiffness depends on the temperature as well. In addition, precipitations could cause variability in the natural frequency since there will be a change in the mass density. Thus, changing environmental conditions will have an effect in the natural frequency as well. [4].

Various DSFs can be extracted from vibration-based data and utilized for detection of damages. However, the manifestation of the effect of environmental changes is almost inevitable [13, 32]. Therefore, it is important to develop methods to quantify and compensate *Environmental and Operational Variability* (EOV), minimizing the variability caused by non-damaged conditions. Currently, the development of such methods is one of the most relevant topics within the field of SHM. Those methodologies developed is designated as either explicit or implicit approaches. Explicit approaches comprise characteristics of measured parameters while implicit approaches utilize the recognition of patterns in the DSFs [17, 27]. Beside mitigating the effect of EOV, the ability to detect small damages highly depends on the choice of DSF [9, 25]. Thus, the requirements of DSF comprise sensitivity towards damages along with minimum sensitivity to the effect of EOV.

The main objective of this study comprises the selection of appropriate DSFs along with most effective EOV compensation methods. The selection of appropriate DSFs is to be analyzed thoroughly to obtain features highly sensitive towards damages. Within this framework, this investigation includes a study on the utility of modal parameters as DSF, in contrast to non-physical quantities, presently in the form of the coefficients of parametric time-series models. Moreover, the most effective EOV compensation method is derived from a comparative analysis of several methods. The comparative analysis includes explicit, implicit and joint implicit/explicit compensation strategies.

The work in this study is focused on experimental vibration data originating from a small-scale wind turbine blade set in a controlled environment. The controlled parameters comprise the ambient temperature and humidity. Additionally, the excitation of the blade is conducted with a shaker fixed near the blade root. On this setup, a variety of testing within a grid of temperature and humidity set points was performed. For each environmental configuration, multiple experiments have been conducted to enhance the statistical certainty, while three conditions were assessed: healthy, and two types of damage [18].

With the accessibility of these data, an efficient damage detection methodology shall be analyzed through various DSFs (modal parameter estimates and coefficients of time-series models). Furthermore, effective mitigation of the controlled environmental changes shall be investigated through statistical approaches and pattern recognition. The effectiveness, and thereby the suitableness of the approach, is determined in terms of increased detectability. In preparation for future work and to strengthen the accessibility of the outcome of this study, the SHM system of this laboratory-scale wind turbine blade is based solely on AOMA (the measured excitation is neglected). Due to the experimental nature of the data, considerations regarding the adaption for an operational environment will be deliberated.

In association with the above, a former study regarding the identification of the laboratory-scale wind turbine blade was performed aiming at optimizing various model structures and reducing the uncertainty of modal parameter estimates, which in the present work are used as DSFs [1].

State of the art

As stated before, one of the main challenges related to the development of a SHM system is the effect of environmental changes. The DSF used to distinguish a reference state from damages, are also impacted by the effect of EOV. Since this issue may be the one with the highest relevance within this scientific field, a thorough investigation of the state of the art is crucial. A vast amount of approaches to mitigate the variability in DSFs caused by EOV are currently available [17, 27, 35, 36].

Some approaches to mitigating the effect of EOV are presented in [27]. The main approach to mitigate the effect of EOV on the natural frequencies of a bridge is by the use of *Second Order Blind Identification* (SOBI), an implicit approach. It is stated if measurements of the *Environmental and Operational Parameters* (EOPs) are available, regression analysis is the most straightforward process, an explicit approach. Therefore, a comparative analysis of the implicit and explicit approach is conducted to assess the effectiveness while two EOPs are available. The effectiveness of the implicit approach did show a perceptible advantage in the compensation of EOV. Vast amounts of different environmental and operational conditions are present in the vibration-based data of the bridge, some more severe to the natural frequencies than others. Furthermore, variability in the EOPs can occur between the different locations of the measured responses or measurements of important EOPs are not available [26, 36]. Therefore, implicit approaches to mitigate the effect of EOV, such as SOBI, can be crucial to removing the influence of EOV, since no requirements of measured EOPs are present.

Another implicit approach to mitigate the effect of EOV, properly more used than SOBI [27], is *Principal Component Analysis* (PCA). The utility of PCA to mitigate the effect of EOV is employed in [36], where the DSF comprise the residual error of the PCA model obtained. To validate the performance of the proposed method, testing on both numerical and experimental data is conducted. For both examples, the main attribution to EOV was temperature changes, yet for the experimental data, other EOPs might have been present. The PCA methodology to mitigate the effect of EOV present in this study proved to be effective and convenient since the method does not require the measurements of any EOPs.

The aforementioned studies did infer more effective mitigation of EOV using an implicit method to mitigate the influence of EOV. In [17], both an implicit and explicit method for compensating the effect of EOV are investigated. The explicit method is a multivariate nonlinear regression, based on *Least Square* (LS) regression, and the implicit method comprises an *Artificial Neural Network* (ANN). Each method is implemented on data from a wind turbine at an operational speed of 43rpm. Furthermore, the measured EOPs comprise temperature, wind speed and the azimuth angle. Also, the standard deviation and maximum amplitude of the response closest to an actuator excitation are used as EOPs. The *True Positive Rate* (TPR) is increased significantly after mitigating the effect of the 5 EOPs used, both for the implicit and explicit method. Yet, the *False Negative Rate* (FNR) is increased for the implicit method after compensation. An interesting aspect is the increment of the *False Positive Rate* (FPR) for the testing data when explicitly compensating for the EOPs. As discussed in the study this might be due to the effect of overcompensating since the EOV differ from the training set to the testing set. Regardless of the increment of the FPR while explicitly mitigate of the influence of EOV, this study showed better damage detectability using an explicit method to mitigate the effect of EOV.

In [4], the effect of a set of measured EOPs is mitigated by the use of *Gaussian Process* (GP) time-series methodology, on low-frequency and high-frequency data. The data originates from multiple acceleration measurements of a wind turbine. In low frequency, the vibration response develops from natural ambient excitation, while for the high-frequency range, the excitation arises from an actuator installed in the blade. The advantage of excitation with an actuator is the ability to excite higher-order modes due to its dynamics. Due to the subsets of data with various behaviour, different DSFs are used. The DSF of the low-frequency content is the coefficients of *Linear Parameter Varying Vector Auto-Regressive model* (LPV-VAR). The DSF of the high-frequency content is chosen as the components in the *Morlet Continuous Wavelet Transform* (CWT). Since the DSF chosen are highly correlated, PCA is conducted to achieve an orthogonal representation of the DSF. In addition, the PCA ensure a dimensionality reduction of the DSF. Subsequently, the *Principal Components* (PCs) are evaluated individually where each of them represents the response of the *Gaussian Process Regression* (GPR) with the input being the different EOPs. By the use of the GP time-series model, the effect of each EOP is analyzed for feature normalization and thereby enhancing the detectability of damages. The main objective of using the coefficients of the parametric system identification method can prove to be useful, since extraction of modal parameters from time-series models comes with some challenges, such as separating physical modes from spurious modes [3].

A similar approach with the use of coefficients from time-series modelling is presented in [29]. The proposed methodology for damage detection and localization is based on the use of coefficients from *Auto-Regression with Exogenous Variable* (ARX) models as DSF. One of four available responses is used to model the input since the governing equation showed that the coefficients then directly relate to the structural stiffness of a numerical shear building. With the use of the Kolmogorov-Smirnov test statistical distance of the ARX-model residual error, the localization of damages was possible. The methodology was also tested experimentally with the presence of damping, noise and multiple damages to prove the ability to localize damages. Undoubtedly, the coefficients from time-series modelling as DSF are influenced by the effect of EOV, which is not studied thoroughly in this study. Yet the main approach of using the coefficients as DSF is shared with the aforementioned study.

Several studies utilize the modal parameters as DSFs instead of the aforementioned utilization of coefficients from time-series modelling [9, 10, 19, 26]. One possible drawback when utilizing the modal parameters is that not all modes of interest can be identified simultaneously under changing ambient environmental conditions [35]. In [11] a vibration-based damage detection approach of a real steel truss bridge is based on the modal parameters estimated by *Auto-Regressive* (AR) models. The bridge is only used for experiments and is equipped with eight accelerometers. Five on the side where the damages are artificially introduced, and three on the opposite side. By the use of stabilization plots to obtain accurate estimates of the modal parameters, the use of natural frequencies as DSF yielded accurate results in detecting damages, especially the first three modes showed high sensitivity. The *Modal Assurance Criterion* (MAC) and *Coordinate Modal Assurance Criterion* (COMAC) as DSF also proved to have high sensitivity towards the damages if a sufficient amount of modes were considered. Although the usage of the MAC and COMAC proved to have high damage sensitivity, the requirement of a sufficient amount of modes can be complicated if high-order modes are not excited.

A challenging aspect associated with the estimation of the modal parameters, especially for AOMA, is the estimation of accurate damping ratios [5, 12], yet their influence on structural behaviour is extensive [22]. The usage of damping as DSF are investigated in [9] for two types of infrastructures, namely reinforced concrete structures and composites. The acknowledgement of the complexity related to identifying the damping is of minor significance with the statement of damping being more sensitive to damages than natural frequency. The usage of damping as DSF is shared in [14] where two experimental setups are utilized. First a small two-dimensional concrete frame, and secondly a three-dimensional aluminium frame, both excited with seismic base excitation. Despite the high potential of utilizing damping for damage detection shared in the aforementioned studies, the investigation hereof is less extensive compared to the usage of natural frequencies.

In previous work [1], numerous non-parametric and parametric system identification methods were tested on a *Finite Element* (FE) representation of the laboratory-scale wind turbine blade used for this study. The objective was to highlight methods with superior accuracy of the estimated modal parameters for a numerical model of the laboratory-scale wind turbine blade. The numerical model was subjected to white Gaussian noise as excitation since random environmental loads can be modelled as white noise [8]. The results showed noticeably higher accuracy for AR models, especially for AOMA where the input is absent. Therefore, simultaneous with the investigation of state of the art approaches, a comparative analysis of the utility of different features for damage detection should be performed. Namely the natural frequencies, damping ratios, and AR coefficients. Furthermore, both implicit, explicit, and a combination should be explored to mitigate the effect of EOV, mainly caused by temperature changes. The basis for the explicit method is Bayesian non-linear regression whereas the implicit method is based on PCA.

Methodology

The overall methodology appraised in this work is presented in Figure 1.1, where the main methodological components are displayed for each step of the methodology. Subsequently, this chapter is devoted to clarifying the processes leading to the main objective of this work, damage detection.

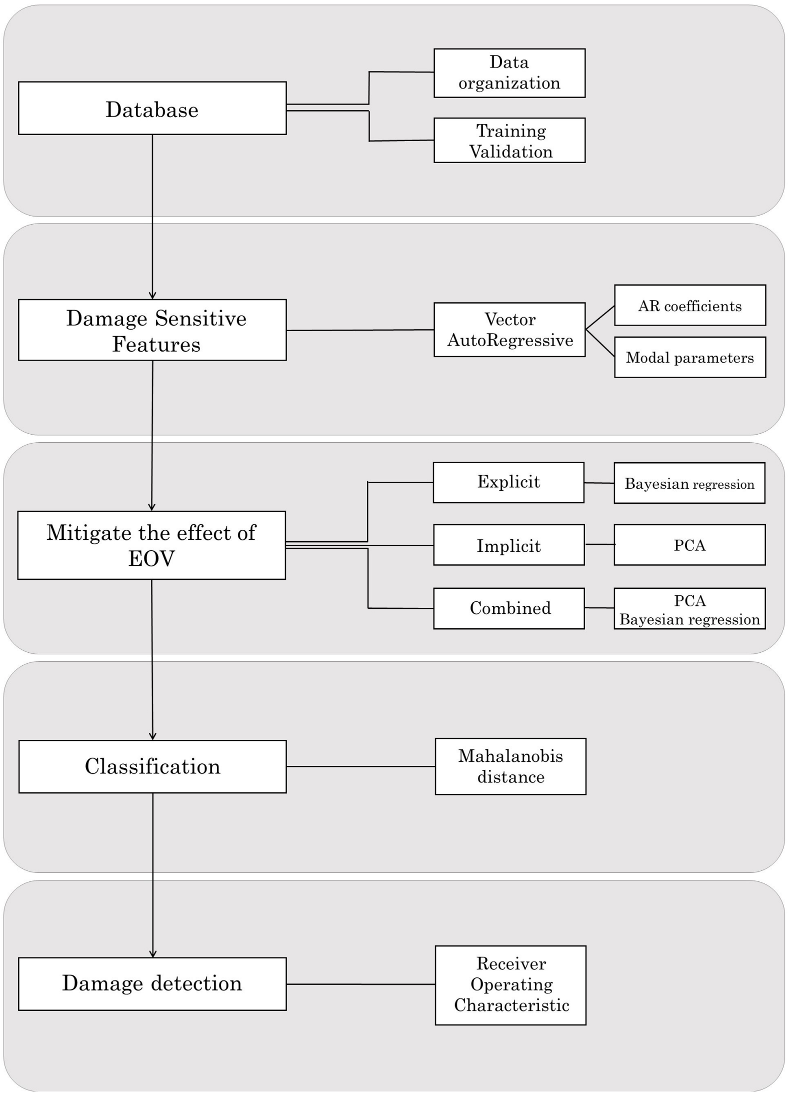

Figure 1.1: Flow chart of the methodology adopted throughout this study

1.1 Database

A brief description of the setup and the various dataset are provided before a further investigation to clarify the origin of the database utilized. A laboratory-scale representation of a wind turbine blade has been manufactured for the purpose of testing in a controlled environment (temperature and humidity). The experimental design and data acquisition were performed in the Stochastic Mechanical Systems Laboratory of the University of Patras, Greece. A more detailed description of the experiment can be found in [18]. The root of the blade is clamped. Hence, the setup is comparable to a cantilevered setup. A shaker is attached to the fixture at the blade root with the purpose of excitation of the blade, Figure 1.2b. For measurements of the response, four accelerometers have been mounted along the blade, as depicted in Figure 1.2a.

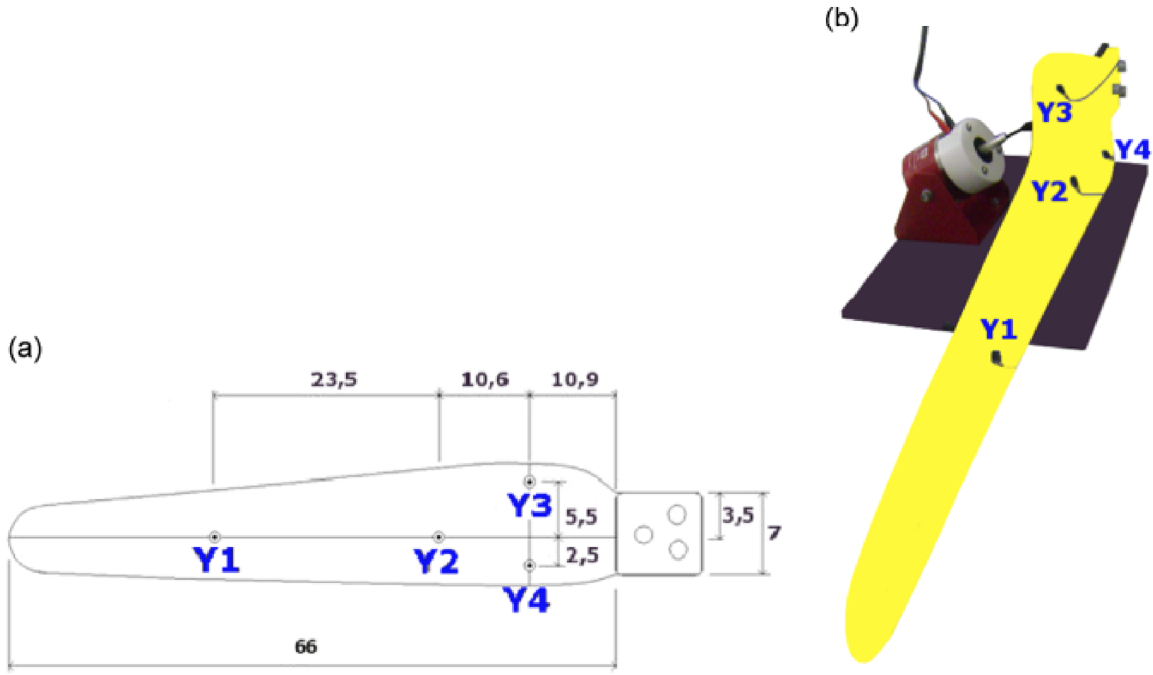

Figure 1.2: Setup of the laboratory-scale wind turbine blade. (a) The location of each accelerometers (distances in cm). (b) An overview of the setup including the shaker. [18]

The specifications of both the accelerometers used and the shaker are presented in Table 1.1. The excitation is assumed to be a random stationary force. Furthermore, the excitation is assumed to have a flat spectrum inside the specified bandwidth.

	Accelerometer	Shaker
Type	PCB ICP 352C22	PCB M288D01
Bandwidth	0.003-10kHz	20-2000Hz
Sensitivity	1.052mV/m/s^2	98.41mV/lb

System specification	
Sampling frequency, f_s	5120Hz
Sampling time, t	6.4 seconds
Blocksize, N	32768

Table 1.1: Specifications of accelerometer, shaker and system setup.

During the experiments, the environmental variabilities consist of temperature variation and for some of the experiments, water has been sprayed onto the blade to simulate rainy conditions. For each condition of the blade at each temperature setting 40 experiments have been conducted, Table 1.2.

Condition	Temperature span	ΔT
Healthy	$[-22°C;+20°C]$	$2°C$
Healthy Water	$[-20°C;+20°C]$	$4°C$
Damage 1	$[-20°C;+20°C]$	$4°C$
Damage 2	$[-20°C;+20°C]$	$2°C$
Damage 2 Water	$[-20°C;+20°C]$	$4°C$

Table 1.2: The available temperature setting for each of the 5 conditions of the blade. The index *Water* indicates the spraying of water to simulate rainy conditions

Pertaining to the damages in Table 1.2, Damage 1 and Damage 2, one damage with two levels of severeness has been introduced to the blade, Figure 1.3. Damage 1 comprises a small drilling hole in the trailing edge of the blade. Damage 2 comprises an elongation of damage 1 where the drilling hole is extended.

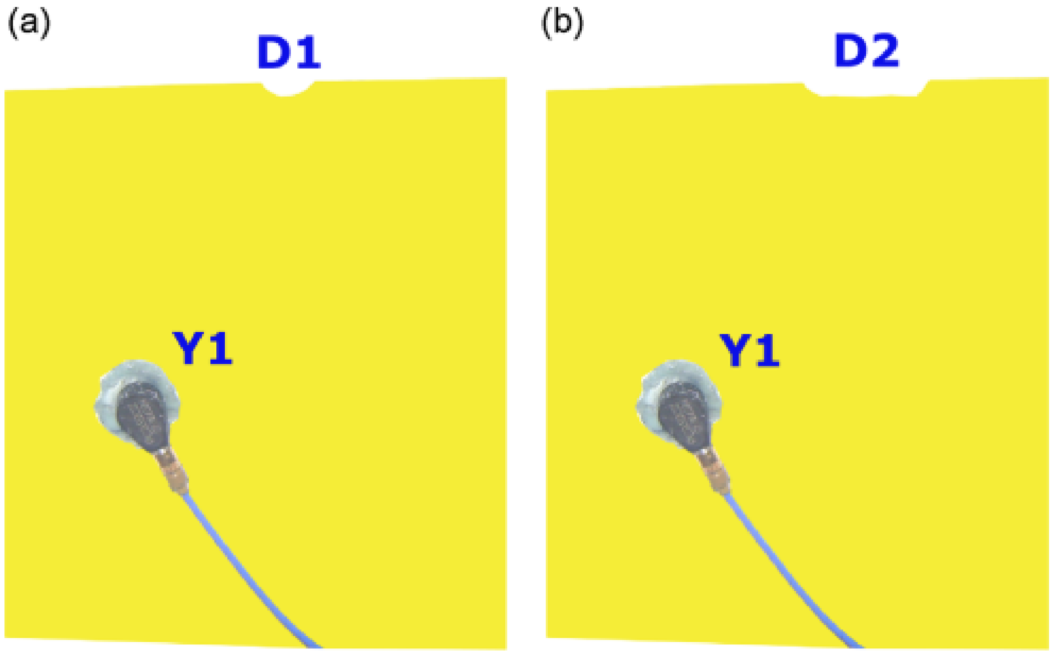

Figure 1.3: Overview of the inflicted damages. (a) Damage 1 (D1) comprises a semicircular hole with a diameter of 5mm in the trailing edge. (b) Damage 2 (D2) comprises an enlargement of damage 1 to a total length of 15mm where the width is retained. [18]

Throughout the study, different models are trained with the data obtained from the healthy state of the blade. Furthermore, some of the data should be used for validation of the training phase. Therefore, the data is divided into training, validation, and testing alone, Table 1.3. The training data are chosen such that 36 out of 40 datasets for each temperature in the range $T = [-20°C; 4°C; 20°C]$ are randomly chosen for the healthy state and healthy state with water applied. Still, data from the healthy state condition with water are not utilized for training regression models. One dataset consists of four measured responses, each with a blocksize of 32 768 [18].

Healthy			Healthy water		D1	D2	D2 water
Training	Validation	Testing	Training	Testing	Testing	Testing	Testing
396	44	440	396	44	440	840	440

Table 1.3: Subset of the dataset used for training, validation and testing

The database referred to throughout this study is formed by all the available data in a single three-dimensional matrix where the first dimension comprises all experiments, the second dimension comprises the four measured responses, and the third dimension comprise the data points within the four measured responses:

$$\text{Database} = \begin{bmatrix} \text{Healthy} \in \begin{bmatrix} n_{-22^\circ C} & n_{-20^\circ C} & \dots & n_{20^\circ C} \end{bmatrix}^T \\ \text{Healthy Water} \in \begin{bmatrix} n_{-20^\circ C} & n_{-16^\circ C} & \dots & n_{20^\circ C} \end{bmatrix}^T \\ \text{Damage 1} \in \begin{bmatrix} n_{-20^\circ C} & n_{-16^\circ C} & \dots & n_{20^\circ C} \end{bmatrix}^T \\ \text{Damage 2} \in \begin{bmatrix} n_{-20^\circ C} & n_{-18^\circ C} & \dots & n_{20^\circ C} \end{bmatrix}^T \\ \text{Damage 2 Water} \in \begin{bmatrix} n_{-20^\circ C} & n_{-16^\circ C} & \dots & n_{20^\circ C} \end{bmatrix}^T \end{bmatrix}_{[3040\times 4\times 32768]} \tag{1.1}$$

Where:

$n =$ Comprise 40 samples (1 sample is equal to four measured responses with the specified blocksize) within each temperature configuration

Throughout the study, especially in Chapter 2, reference to the i^{th} dataset comprise the rows of the Database where $i = 1, 2, 3, \dots, 3040$ which are used for calculation of the relevant DSF.

Since the objective of this study is the detection of known damages through AOMA, the measured excitation will not be utilized. In real-life structures the excitation usually consist of different EOPs where available measurements are confined, [4, 8, 17]. Therefore, the accessibility of the outcome of this study may be strengthened if only the measured responses are used.

1.2 Damage Sensitive Features

As stated previously the damage detection should be based on several features assumed to be sensitive to the damages introduced, Section 1.1. Three types of features should be extracted from the data, namely the natural frequencies, the damping ratios, and the coefficients of AR-models. The achievement of such features is investigated in the following section.

1.2.1 Vector Auto-Regressive models

Since Auto-Regressive (AR) models were found to have an appreciable accuracy for a FE representation of the setup that has been used throughout this study, the system identification is based on the *vector AR* model (VAR). [1].

First, the theory of the VAR model is examined to enhance the knowledge concerning the use of the model. In general, AR models are used to predict future values of a time series with the knowledge of previous data points. Given m responses as column vectors, $\boldsymbol{y}(n)$:

$$\boldsymbol{y}(n) = -\sum_{i=1}^{n_a} \boldsymbol{A}_i \cdot \boldsymbol{y}(n-i) + \boldsymbol{w}(n) \tag{1.2}$$

where the multivariate innovations, comprise the part that cannot be predicted by previous data, are *Normally and Independently Distributed* (NID) with a zero mean and covariance matrix, $\boldsymbol{\Sigma}_w$:

$$\boldsymbol{w}(n) \sim NID(\boldsymbol{0}, \boldsymbol{\Sigma}_w) \tag{1.3}$$

and the AR coefficients, $\boldsymbol{A}$, are gathered in the parameter matrix:

$$\boldsymbol{\Theta} = \begin{bmatrix} \boldsymbol{A}_1 & \boldsymbol{A}_2 & \dots & \boldsymbol{A}_{n_a} \end{bmatrix}_{m \times m \cdot n_a} \tag{1.4}$$

Obtaining the parameter matrix is an optimization problem to yield the best fit of the available observations. One of the most common approaches, also adopted through this study, is based on the *Least Square* (LS) criterion, based on the one-step-ahead *Prediction Error* (PE). The one-step-ahead PE is defined as:

$$\hat{\boldsymbol{e}}(n) = \boldsymbol{y}(n) - \hat{\boldsymbol{y}}(n) \tag{1.5}$$

The one-step-ahead prediction can be written as (based on Equation (1.2)):

$$\hat{\boldsymbol{y}}(n) = -\sum_{i=1}^{n_a} \boldsymbol{A}_i \cdot \boldsymbol{y}(n-i) \tag{1.6}$$

subsequently, the one-step-ahead PE takes the form:

$$\hat{\boldsymbol{e}}(n) = \boldsymbol{y}(n) + \sum_{i=1}^{n_a} \boldsymbol{A}_i \cdot \boldsymbol{y}(n-i) \tag{1.7}$$

which commonly is re-written in the regression form:

$$\hat{\boldsymbol{e}}(n) = \boldsymbol{y}(n) - \boldsymbol{\phi}(n)^T \cdot \boldsymbol{\Theta} \tag{1.8}$$

The regression matrix, also referred to as design matrix, is defined as:

$$\boldsymbol{\phi}(n) = \begin{bmatrix} -\boldsymbol{y}^T(n-1) & \dots & -\boldsymbol{y}^T(n-n_a) \end{bmatrix}^T \tag{1.9}$$

The use of PE of the signal to time instance n does not assess the complete model. To assess the entire signal of length N, the LS error is used which, combined with the regression form, is defined as:

$$V_N(\boldsymbol{\Theta}, \boldsymbol{Z}^N) = \frac{1}{N} \sum_{n=1}^{N} (\boldsymbol{y}(n) - \hat{\boldsymbol{y}}(n))^2 = \frac{1}{N} tr\left\{(\boldsymbol{Y}_N - \boldsymbol{\Theta} \cdot \boldsymbol{\Phi}_N) \cdot (\boldsymbol{Y}_N - \boldsymbol{\Theta} \cdot \boldsymbol{\Phi}_N)^T\right\} \tag{1.10}$$

Where:

tr = the sum of the diagonal of the matrix $\left\{(\boldsymbol{Y}_N - \boldsymbol{\Theta} \cdot \boldsymbol{\Phi}_N) \cdot (\boldsymbol{Y}_N - \boldsymbol{\Theta} \cdot \boldsymbol{\Phi}_N)^T\right\}$
$\boldsymbol{Z}^N$ = Dataset of input and output

The regression matrix defined in Equation (1.9) is for the signal at time instance n. The regression matrix for the complete signal is defined as:

$$\boldsymbol{\Phi}_N = \begin{bmatrix} \boldsymbol{\phi}(1) & \boldsymbol{\phi}(2) & \dots & \boldsymbol{\phi}(N) \end{bmatrix} \tag{1.11}$$

Moreover, the response matrix, $\boldsymbol{Y}_N$, is defined as:

$$\boldsymbol{Y}_N = \begin{bmatrix} \boldsymbol{y}(1) & \boldsymbol{y}(2) & \dots & \boldsymbol{y}(N) \end{bmatrix} \tag{1.12}$$

Henceforth, the LS error in Equation (1.10) should be minimized to obtain the best fit. This can be expressed as:

$$\hat{\boldsymbol{\Theta}}_{LS} = \arg\max_{\boldsymbol{\Theta}} V_N(\boldsymbol{\Theta}, \boldsymbol{Z}^N) \tag{1.13}$$

Since the proposed model is linear, the optimization follows a simple methodology. Calculate the derivative of Equation (1.10) with respect to the AR-coefficients in the parameter matrix $\boldsymbol{\Theta}$ given in Equation (1.4), set to zero for local minimum and solve for $\boldsymbol{\Theta}$, yielding the following:

$$\hat{\boldsymbol{\Theta}}_{LS} = \boldsymbol{Y}_N \boldsymbol{\Phi}_N^T \left(\boldsymbol{\Phi}_N \boldsymbol{\Phi}_N^T\right)^{-1} \tag{1.14}$$

Subsequently, when $\hat{\boldsymbol{\Theta}}_{LS}$ is obtained, a state space representation of the VAR model, Equation (1.2), leads to the state matrix:

$$\boldsymbol{A}_d = \begin{bmatrix} -\boldsymbol{A}_1 & -\boldsymbol{A}_2 & \dots & -\boldsymbol{A}_{n_a-1} & -\boldsymbol{A}_{n_a} \\ \boldsymbol{I} & 0 & \dots & 0 & 0 \\ 0 & \boldsymbol{I} & \dots & 0 & 0 \\ \vdots & \vdots & \ddots & \vdots & \vdots \\ 0 & 0 & \vdots & \boldsymbol{I} & 0 \end{bmatrix} \tag{1.15}$$

and through eigenvalue decomposition of the state matrix $\boldsymbol{A}_d$, modal analysis can be performed. The eigenvalue decomposition is defined as:

$$(\mu_n \boldsymbol{I} - \boldsymbol{A}_d)\, \boldsymbol{\psi}_n = 0 \tag{1.16}$$

and since the defined system is in discrete time and not a continuous system, the relationship between the poles and the modal parameters is defined as: [3, 23]

$$\omega_n = \left| \frac{\ln \mu_n}{T_s} \right| \tag{1.17}$$

$$\zeta_n = -\cos(\angle \ln \mu_n) \tag{1.18}$$

Where:

$T_s =$ Sample period

1.2.1.1 Selection of suitable model structure

An important consideration is the selection of the best model structure, n_a in Equation (1.2). As n_a increases the PE decreases, but it is not desirable to let n_a tend to a high value for several reasons.

- Numerical issues are increased for very complex model structures.
- The stability of the estimated modal parameters, Equation (1.16), deteriorates at some point, leading to poor estimates.
- Complex model structures are computationally heavy.

Therefore, the choice of n_a should be based on high model accuracy without too complex a model structure. The choice is established by a thorough analysis of the *Residual Sum of Squares over the Series Sum of Squares* (RSS/SSS),

$$RSS/SSS = \frac{\sum_{i=1}^{N}(y_i - \hat{y}_i)^2}{\sum_{i=1}^{N} y_i^2} \tag{1.19}$$

the *Bayesian Information Criterion* (BIC),

$$BIC = N \ln \widehat{\sigma}_w^2 + d \ln N \tag{1.20}$$

Where:

$d =$ The size of $\boldsymbol{\Theta}$ containing the AR coefficients

the *Samples Per Parameter* (SPP),

$$SPP = \frac{N \cdot m}{N_\Theta} \tag{1.21}$$

Where:

$N_\Theta =$ Number of AR coefficients
$m \;\; =$ Number of responses

and the frequency stabilisation plot. The RSS/SSS is an explanation of how much of the signal can be explained by the model. The analysis of the RSS/SSS can not stand alone since it does not measure the adaptation of different datasets. The BIC can be used as a supplement since it includes a penalization term which penalizes the model complexity. Furthermore, for reliable estimates of the modal parameters, a sufficient amount of SPP should be present. Lastly, an investigation of a frequency stabilization plot can provide the basis for choosing n_a. The content of the frequency stabilization plot is all the modes determined by the modal analysis, Equation (1.16-1.18). Some of them are spurious modes and others are physical modes, where the physical modes should tend to stabilize as n_a increases. Commonly, the frequency stabilization plot is compared to the *Power Spectral Density* (PSD). This gives the visual ability for analyzing if the consistent frequencies are matching the corresponding peaks in the PSD. [3].

For choosing a suitable model order, a single data set from the healthy state of the blade is used at a temperature of $0°C$. The frequency stabilization plot hereof for $n_a \in [1, 100]$ is shown in Figure 1.4. Especially for low-order models, many of the modes are not stable up until a model order of 60-65. Another potential issue is the increment of spurious modes for a high value of n_a. Based solely on the frequency stabilization plot in Figure 1.4, a model order of 65 appears to be suitable.

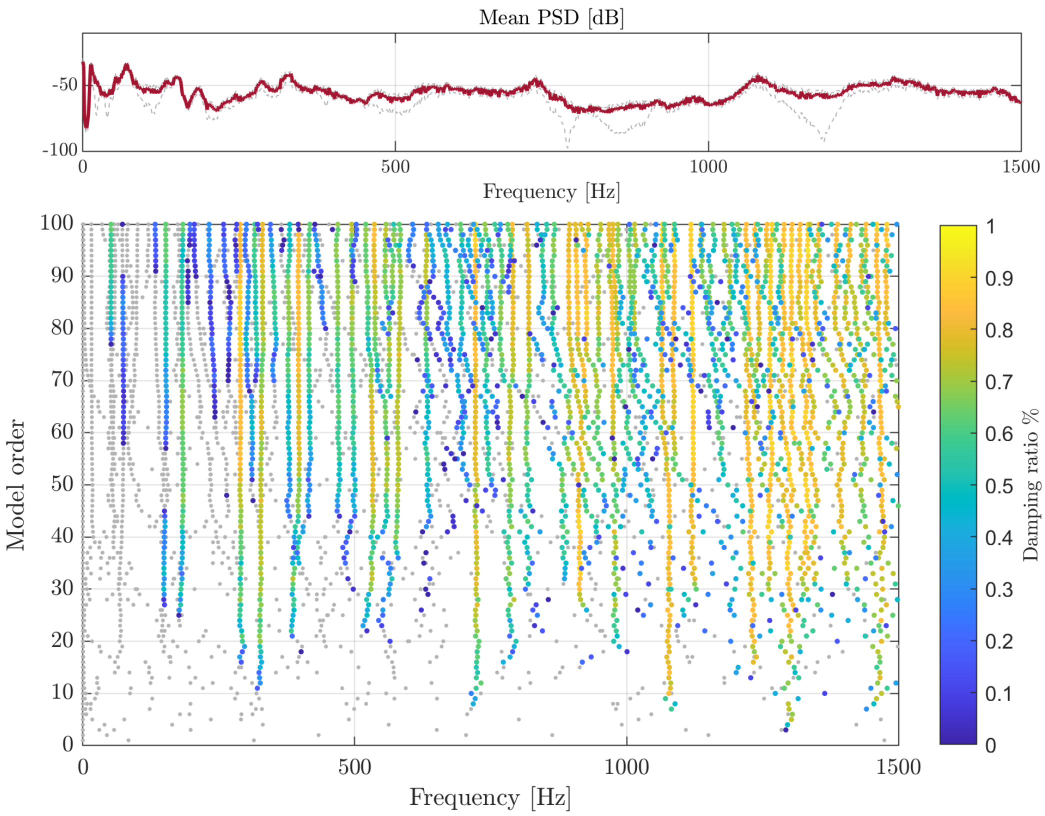

Figure 1.4: Frequency stabilization plot for $n_a \in [1, 100]$. The dataset used origins from the healthy state of the blade.

For validating the choice of model order, an analysis of RSS/SSS, BIC and SPP is required. The analysis can be seen in Figure 1.5. For a model order of 65, the SPP is approximately 17 which is assumed to be sufficient. Furthermore, the RSS/SSS decrease and then stabilize from a model order of 50. The BIC does not seem to stabilize but increases as n_a increases. Due to the penalization term in Equation (1.20), the choice of n_a should be aimed to reduce the value of the BIC. Since the low-order modes do not stabilize until a model order of 60-65, a lower value of the BIC can be difficult to obtain. Therefore, a model order of 65 is chosen.

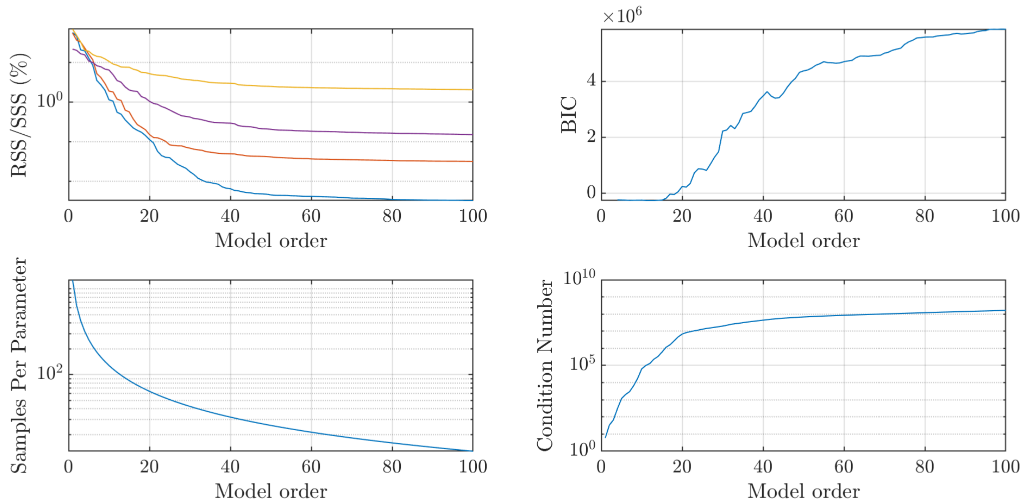

Figure 1.5: RSS/SSS, BIC, SPP and the conditions number for increasing n_a

1.2.1.2 Extracting the natural frequencies of interest

After calculating the frequencies according to Equation (1.16-1.18) at a specific model order, a vital procedure of the VAR model as system identification is the extraction of not at least the physical modes but also those of interest. The number of frequencies determined by Equation (1.16-1.18) correspond to the chosen model order, n_a, times the number of responses. Figure 1.6 is an overview of all frequencies at a specific model order of 65. These frequencies can be categorized as either frequencies of a physical mode or frequencies of a spurious mode. Spurious modes are not related to the structural dynamics yet a result of a numerical resolution. Therefore, the challenging aspect is to quantify and extract the physical frequencies instead of the spurious frequencies in Figure 1.6.

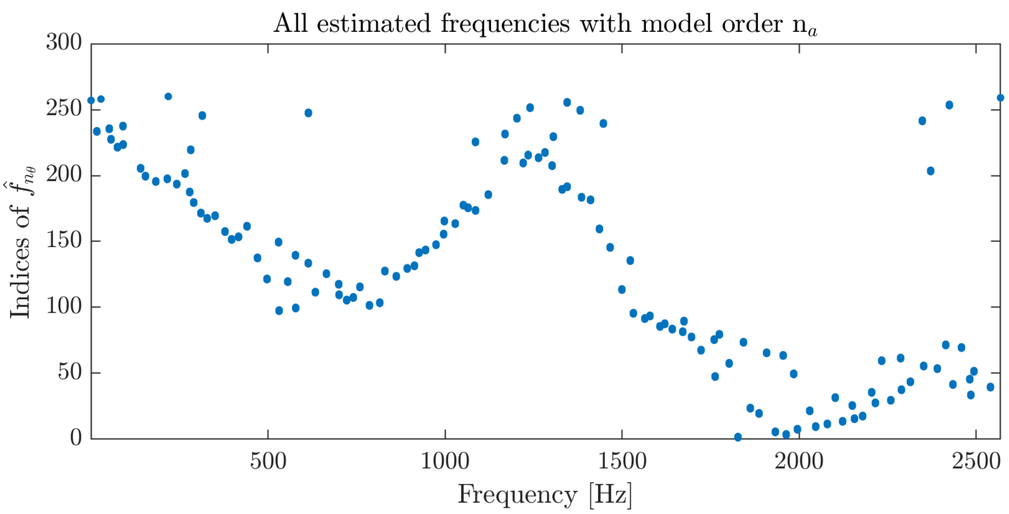

Figure 1.6: All frequencies of the VAR model at a specific model order of 65

One method of extracting the natural frequencies is the usage of the Euclidean distance between a reference frequency and those obtained from the VAR model [15]. The reference frequencies may originate from peak picking of the PSD or other non-parametric methods. Initially, all possible resonance peaks in the PSD are chosen, Figure 1.7.

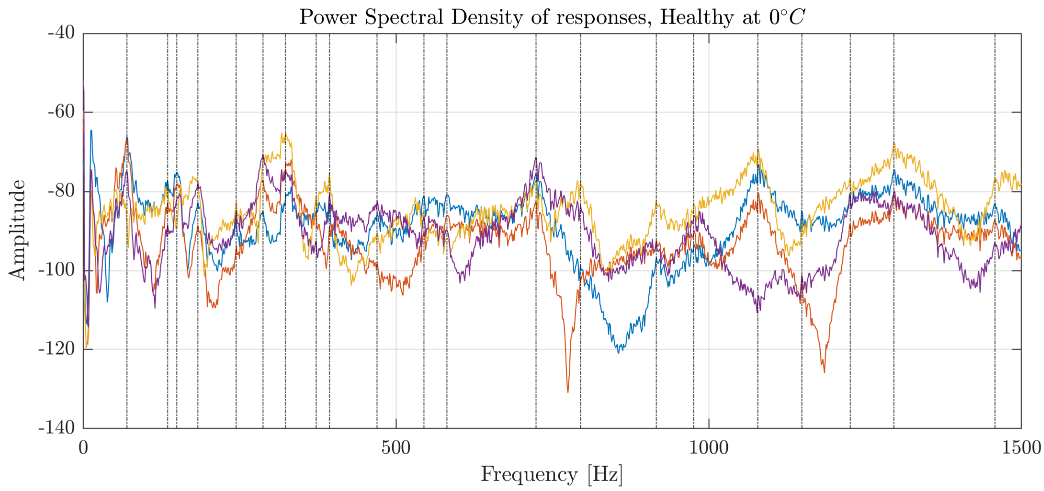

Figure 1.7: Power Spectral Density of all four responses. The black lines are the chosen peaks. The dataset used origins from the reference state at a temperature of $0°C$

Then, the Euclidean distance can be calculated between the frequencies determined by Equation (1.17), $\hat{\boldsymbol{x}}_j$, and those obtained from the PSD, $\boldsymbol{x}_r$ [20]:

$$d(\boldsymbol{x}_r,\hat{\boldsymbol{x}}_j) = \left(\sum_{i=1}^{n} (x_{r_i} - \hat{x}_{j_i})^2 \right)^{1/2} \tag{1.22}$$

Afterwards, those frequencies from the VAR model closest to the reference are kept with their corresponding mode shape and damping ratio, Equation (1.16) and (1.18). To enable which natural frequencies are of interest, an analysis of each mode should be conducted. The estimated mode shapes determined by Equation (1.16) can be simulated to identify the natural frequency of interest. To ease the simulation of the mode shapes, the mode shapes are normalized with respect to the maximum of the imaginary part:

$$\overline{\boldsymbol{\psi}} = \frac{\boldsymbol{\psi}}{\max\{|\mathrm{Im}\{\boldsymbol{\psi}\}|\}} \tag{1.23}$$

and with the knowledge of the location of the accelerometers, a grid for the blade can be created, Figure 1.8.

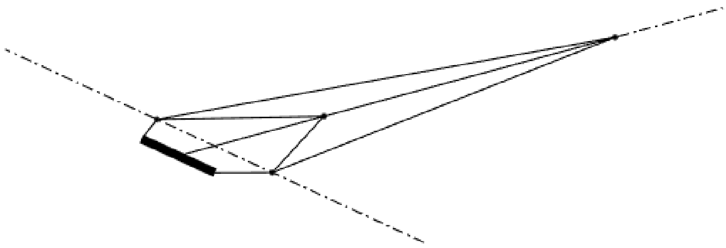

Figure 1.8: Created grid of the blade with the location of the accelerometers. The black dots represent the locations according to Figure 1.2. The black solid line represent the restraint of the blade.

The purpose of the simulation is to divide the modes into three categories of motion. With no knowledge of the excitation (since the basis of this study is AOMA), the estimated modes can be highly affected by the dynamics of the excitation [7]. Therefore, the modes that do not fit within these categories are rejected. The three categories can be seen in Figure 1.9.

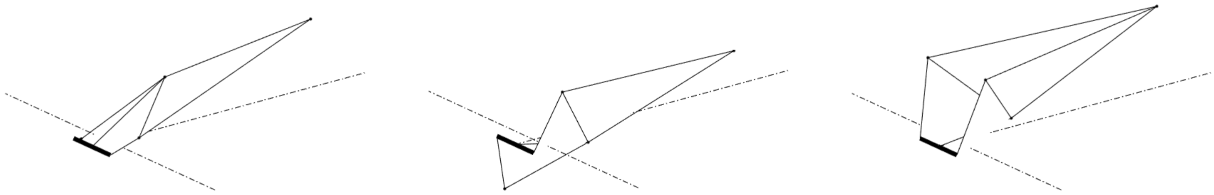

(a) **(b)** **(c)**

Figure 1.9: The three categories of mode shapes. (a) Bending mode in the flapwise direction. (b) Mode dominated by torsional deflection. (c) Mode dominated by flapping motion.

After carefully evaluating the mode shapes in Equation (1.23) for all the estimated natural frequencies, the categorization led to nine natural frequencies of interest:

Bending	Torsion	Flapping
$\hat{f}_{b_1} = 70$	$\hat{f}_{t_1} = 180$	$\hat{f}_{f1} = 240$
$\hat{f}_{b_2} = 148.75$	$\hat{f}_{t_2} = 287.5$	$\hat{f}_{f_2} = 482.5$
$\hat{f}_{b_3} = 985$	$\hat{f}_{t_3} = 326.26$	$\hat{f}_{f_3} = 726.25$

Table 1.4: First three natural frequencies of the three categories. All estimated natural frequencies are stated in Hz. Furthermore, the frequencies origins from the healthy state at $0°C$

1.3 Mitigating the effect of Environmental and Operational Variability

Independent of the chosen DSF, it can be altered by EOV. If the effect of EOV is not mitigated, it can be interpreted as an effect of damage in the system. Therefore, it is essential to mitigate the effect of EOV before any damage detection. This process is also referred to as data normalization and can be accomplished by several methods. The overall process of data normalization is allocated in two main approaches, an explicit method and an implicit method. Explicit methods use available measurements of different EOPs to enhance the possibility of compensating, typically by the use of regression models to track the trend caused by the EOPs. Implicit methods are based solely on the observed pattern for a reference state. One such approach is projection methods where a projection of the DSF into a specific space aid the process of mitigating the effect of EOV. [15, 17].

1.3.1 Explicit method

To explicit mitigate the effect of EOV, measurements of at least one EOP are required. By the assumption that a given cause, the EOP, affects the DSF, a functional relationship with the EOP as input can be established. Several methods for building a functional relationship exist. Mainly, two general models can be utilized, either deterministic models or stochastic models. The deterministic models comprise classical regression models such as LS regression. The disadvantage of utilising classical regression models is the sensitivity to outliers. On the other hand, stochastic models seek to represent the observed trend and the associated uncertainty. Stochastic models comprise Bayesian regression models where the regression model is obtained by the posterior distribution (the probability of the regression model given the observations). [17].

1.3.1.1 Bayesian regression

To obtain knowledge of how the DSF changes without any form of damage, regression models of the DSF extracted from the healthy state of the blade can be used (The specified training data of the healthy state without water applied, Table 1.3). Then these regression models should track the change in the specific DSF due to the EOP (the temperature in this case) since they are trained with data that do not have any damages introduced.

The simplest regression model is based on the *Ordinary Least Square* (OLS) method. The methodology is simply minimizing the sum of squared differences between the observed data and the response of the regression model. Considering a linear relationship between the input and output:

$$\boldsymbol{Y} = \beta_0 + \beta_1\boldsymbol{X} + \boldsymbol{\varepsilon} = \boldsymbol{\Phi}\boldsymbol{\beta} + \boldsymbol{\varepsilon} \tag{1.24}$$

Where:

$$\begin{aligned}
\boldsymbol{\Phi} &= \begin{bmatrix} 1 & \boldsymbol{X} \end{bmatrix}, \boldsymbol{\beta} = \begin{bmatrix} \beta_0 \\ \beta_1 \end{bmatrix} \\
\boldsymbol{\varepsilon} &= \text{Errors of the observations where } \varepsilon_i \sim N(0,\sigma^2) \\
\boldsymbol{X} &= \text{Column vector with input observations} \\
\boldsymbol{Y} &= \text{Column vector with the output observations}
\end{aligned}$$

Since the residual error is independent and identically normally distributed, the likelihood function corresponds to a similar distribution:

$$p(\boldsymbol{Y}|\boldsymbol{\Phi},\boldsymbol{\beta},\sigma^2) \propto (\sigma^2)^{-\frac{n}{2}} \exp\left(-\frac{1}{2\sigma^2}(\boldsymbol{Y}-\boldsymbol{\Phi}\boldsymbol{\beta})^T(\boldsymbol{Y}-\boldsymbol{\Phi}\boldsymbol{\beta})\right) \tag{1.25}$$

For a single set of input and output, the residual can be written as:

$$\varepsilon_i = y_i - \hat{y}_i = y_i - \boldsymbol{\Phi}(x_i)\boldsymbol{\beta} \tag{1.26}$$

and by sum up all of the residuals squared, the *Residual Sum of Squares* (RSS) can then be expressed as:

$$RSS = \varepsilon_1^2 + \varepsilon_2^2 + \ldots + \varepsilon_n^2 = \sum_{i=1}^{n} (y_i - \boldsymbol{\Phi}(x_i)\boldsymbol{\beta})^2 \tag{1.27}$$

which should be minimized. By calculus similar to minimizing the residual errors in Section 1.2.1 the estimated parameters can then be calculated as:

$$\hat{\boldsymbol{\beta}} = (\boldsymbol{\Phi}^T\boldsymbol{\Phi})^{-1}\boldsymbol{\Phi}^T\boldsymbol{Y} \tag{1.28}$$

The regression model in (1.24) is with the assumption of a linear relationship between the input and output. The regression model can be modified to the assumption of a non-linear relationship between the input and output. By the use of polynomials the non-linear relationship can be written as:

$$\boldsymbol{Y} = \beta_0 + \beta_1\boldsymbol{X} + \beta_2\boldsymbol{X}^2 \ldots \beta_p\boldsymbol{X}^p + \boldsymbol{\varepsilon} = \boldsymbol{\Phi}\boldsymbol{\beta} + \boldsymbol{\varepsilon} \tag{1.29}$$

Where:

$$\boldsymbol{\Phi} = \begin{bmatrix} 1 & \boldsymbol{X} & \boldsymbol{X}^2 & \cdots & \boldsymbol{X}^p \end{bmatrix}, \boldsymbol{\beta} = \begin{bmatrix} \beta_0 \\ \beta_1 \\ \beta_2 \\ \vdots \\ \beta_p \end{bmatrix}$$

The parameters of the regression model in (1.29) can be calculated as (1.28). [20, 34]. The obtained estimate of the parameters, $\boldsymbol{\beta}$, relies heavily on the number of observations. Furthermore, the estimate of $\boldsymbol{\beta}$ relies on the assumption that the observations are specific points rather than originating from a distribution. Since the available training data is limited and the observed response must be a consequence of a distribution, the likelihood function in (1.25) can be supplemented with a prior belief of the parameter distribution. This is known as Bayesian regression. The posterior distribution of the parameters can be written as:

$$p(\boldsymbol{\beta},\sigma^2|\boldsymbol{Y}\boldsymbol{\Phi}) \propto p(\boldsymbol{Y}|\boldsymbol{\Phi},\boldsymbol{\beta},\sigma^2)p(\boldsymbol{\beta}|\sigma^2)p(\sigma^2) \tag{1.30}$$

Where:

$p(\boldsymbol{Y}|\boldsymbol{\Phi},\boldsymbol{\beta},\sigma^2) =$ Likelihood of $\boldsymbol{Y}$ given the input observations, $\boldsymbol{\Phi}$, and the parameters, $\boldsymbol{\beta}$ and σ^2

$p(\boldsymbol{\beta}|\sigma^2) =$ Normal distribution of the parameter, $\boldsymbol{\beta}$, given the variance of the residual errors, the prior belief of the mean values and precision matrix (Inverse of the covariance matrix)

$p(\sigma^2) =$ Inverse-Gamma distribution of the variance of the residual error given the prior belief of the shape and scaling factors

The posterior mean can be expressed by the OLS estimate, $\hat{\boldsymbol{\beta}}$, and the prior mean, $\boldsymbol{\mu}_0$, weighted by the prior precision matrix, $\boldsymbol{\Lambda}_0$:

$$\boldsymbol{\mu_n} = \left(\boldsymbol{\Phi}^T\boldsymbol{\Phi}+\boldsymbol{\Lambda}_0\right)^{-1}\left(\boldsymbol{\Phi}^T\boldsymbol{\Phi}\hat{\boldsymbol{\beta}}+\boldsymbol{\Lambda}_0\boldsymbol{\mu}_0\right) \tag{1.31}$$

then with some re-arrangement, the posterior can be expressed as:

$$p(\boldsymbol{\beta},\sigma^2|\boldsymbol{Y}\boldsymbol{\Phi}) \propto p(\boldsymbol{\beta}|\sigma^2,\boldsymbol{Y},\boldsymbol{\Phi})p(\sigma^2|\boldsymbol{Y},\boldsymbol{\Phi}) \tag{1.32}$$

Where:

$p(\boldsymbol{\beta}|\sigma^2,\boldsymbol{Y},\boldsymbol{\Phi}) =$ $N(\mu_n,\sigma^2\Lambda_n^{-1})$

$p(\sigma^2|\boldsymbol{Y},\boldsymbol{\Phi}) =$ Inverse-Gamma distribution given the shape factor and scaling factor, a_n and b_n

The posterior mean values and the precision matrix are weighted by the prior belief as:

$$\boldsymbol{\Lambda}_n = \left(\boldsymbol{\Phi}^T\boldsymbol{\Phi}+\boldsymbol{\Lambda}_0\right) \tag{1.33}$$

$$\boldsymbol{\mu_n} = (\boldsymbol{\Lambda}_n)^{-1}\left(\boldsymbol{\Phi}^T\boldsymbol{\Phi}\hat{\boldsymbol{\beta}}+\boldsymbol{\Lambda}_0\boldsymbol{\mu}_0\right) \tag{1.34}$$

Similarly, the posterior shape and scaling factor of the Inverse-Gamma distribution is weighted by the prior belief and the posterior mean values and precision matrix:

$$a_n = a_0 + \frac{n}{2} \tag{1.35}$$

$$b_n = b_0 + \frac{1}{2}\left(\boldsymbol{Y}^T\boldsymbol{Y} + \boldsymbol{\mu}_0^T\boldsymbol{\Lambda}_0\boldsymbol{\mu}_0 - \boldsymbol{\mu}_n^T\boldsymbol{\Lambda}_n\boldsymbol{\mu}_n\right) \tag{1.36}$$

One of the advantages of the Bayesian approach is the ability of updating the prior belief with the posterior until the parameters converge. Thereby, the impact of the lack of observations is not as severe as seen for the OLS approach. [33].

1.3.1.2 Assessing the performance

When a model of the training observations is obtained, several measurements can be conducted to assess the accuracy. An important consideration is the complexity of the model. As the complexity increase, the training error decrease. But a highly complex model can have decreased predictability to observations different from the training observations. Therefore, it is essential to assess the performance of both training observations and validation observations, with the latter being of substantial importance.

Determination of the model complexity can be based on the *Mean Squared Error* (MSE) of the training and validation observations respectively. The MSE is simply a measurement of how close the predicted value is to the given observation:

$$MSE = \frac{1}{n}\sum_{i=1}^{n}\left(y_i - \hat{f}(x_i)\right)^2 \tag{1.37}$$

As the complexity increase, the MSE of training and validation data decrease. But at some point, the MSE of validation data will increase due to the effect of overfitting the model towards the training data, Figure 1.10. Therefore, the model complexity should be chosen to obtain the minimum MSE for both the training and validation data.

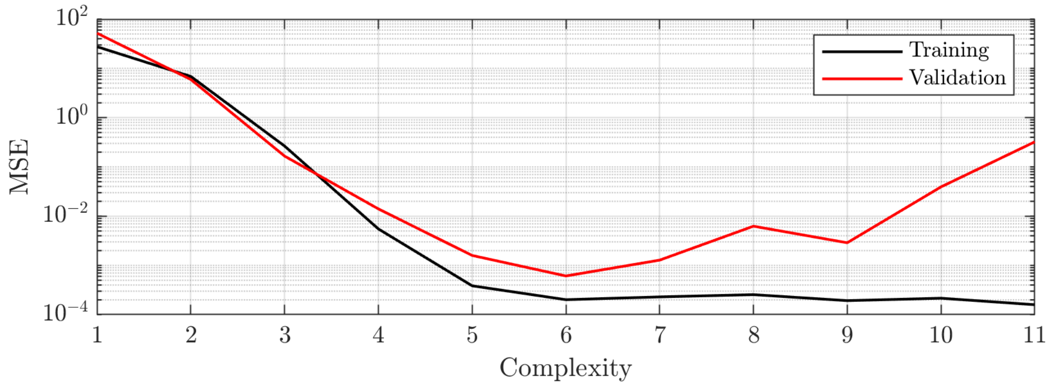

Figure 1.10: MSE of both training and validation data for increasing model complexity. For this simple example, the polynomial order of the regression model, p in Equation (1.29), should be chosen to be six.

After the selection of the model complexity, other statistical measurements of how well the model fits the data should be conducted. The coefficient of determination, or simply R^2, is a ratio between how much of the variance that can be explained by the model and the total variance:

$$R^2 = \frac{TSS - RSS}{TSS} = 1 - \frac{\sum_{i=1}^{n} (y_i - \hat{y}_i)^2}{\sum_{i=1}^{n} (y_i - \bar{y})^2} \tag{1.38}$$

Where:

$$\begin{aligned} TSS &= \text{Total Sum of Squares} \\ \bar{y} &= \text{Mean value of observed responses} \end{aligned}$$

The R^2 value ranges from 0 to 1. If R^2 equals one, all the variance in the observed responses can be explained by the obtained model. A low R^2 value does not indicate a poor model necessarily, since significant variance of the observations can be present.

Another statistical procedure is to check if there is a relationship between the predictor and the response, $\boldsymbol{X}$ and $\boldsymbol{Y}$ in Equation (1.29) respectively, also referred to as the hypothesis test. The null hypothesis is defined as no relationship between the predictor and the response:

$$H_0 : \beta_1 = \beta_2 = \beta_3 = \ldots = \beta_p = 0 \tag{1.39}$$

and the alternative hypothesis defined as a relationship between the predictor and the response is present (at least one of the parameters, β_j, is different from 0):

$$H_a : \beta_j \neq 0 \tag{1.40}$$

To determine whether the null hypothesis, H_0, should be rejected or not, the F-statistic is calculated. An F-statistic larger than one indicates evidence against the null hypothesis. If a vast amount of data is used to determine the F-statistic (n), a value close to one provides evidence enough to reject H_0. Otherwise, an F-statistic significance larger than one is required. [20]. The F-statistic is defined as:

$$F = \frac{(TSS - RSS) \cdot (n - p - 1)}{RSS \cdot p} \tag{1.41}$$

1.3.1.3 Regression matrix

To build the nonlinear regression matrix in the Bayesian regression approach, $\boldsymbol{\Phi}$ in Equation (1.29), several approaches can be pursued. The approach in Equation (1.29) can be prone to instability for high orders. If a vast-ranging input exists high orders regressors tend to a significantly small value, and therefore, are sensitive to numerical calculations. To avoid numerical instability, a variety of different polynomials exist. Among these is Legendre Polynomials:

$$P_n(x) = \sum_{m=0}^{M} (-1)^m \cdot \frac{(2n - 2m)!}{2^n m! (n - m)! (n - 2m)!} x^{n-2m} \tag{1.42}$$

Where:

$M = \frac{n}{2}$ or $\frac{n-1}{2}$ depending on which is an integer.

Legendre polynomials are defined within the space of $[-1,1]$, Figure 1.11. [21]. The Bayesian nonlinear regression models obtained throughout this study will be based on Legendre Polynomials.

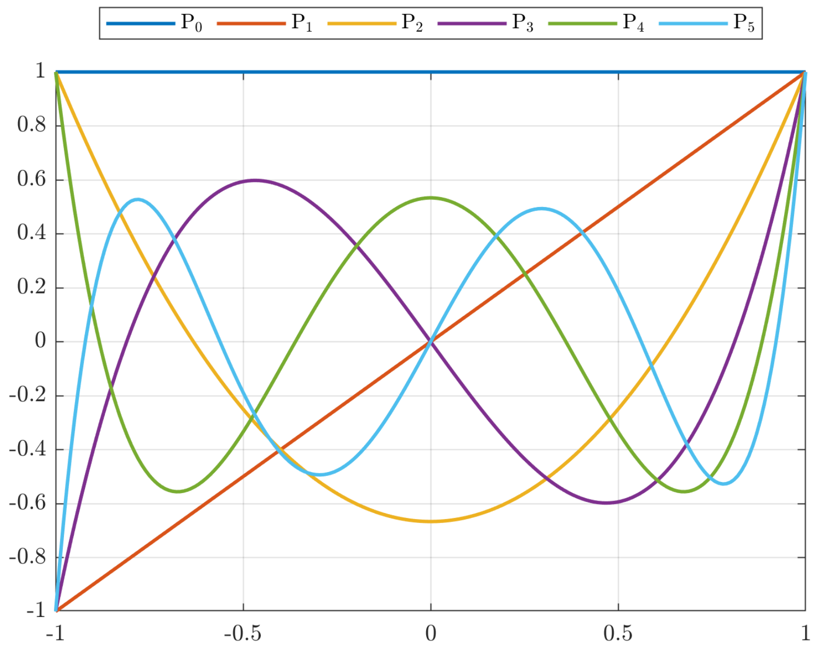

Figure 1.11: First six Legendre polynomials

1.3.1.4 Procedure

Given the hypothesis test in Section 1.3.1.2 an analysis whether a relationship between the EOP and the variability in the DSF exist of not can be conducted. If the null hypothesis is rejected, it can be assumed that the given EOP is causing the variability in the DSF. [17].

Initially, if the DSF are shown versus a given EOP, namely the temperature, a visual inspection whether the cause have an effect can be conducted. Figure 1.12 illustrate three of the estimated natural frequencies versus the temperature. Clearly, the temperature is affecting the natural frequency to some extent. Furthermore, almost a linear relationship is observed.

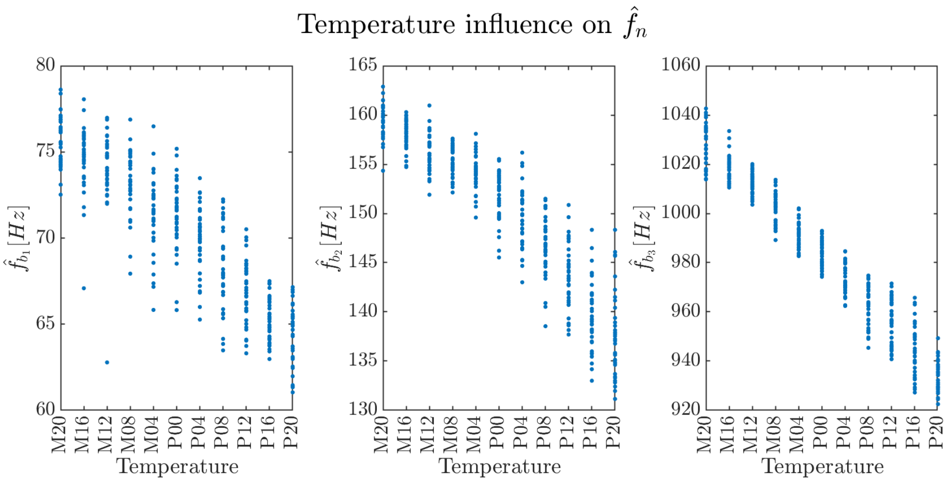

Figure 1.12: Visualization of the three bending modes estimated natural frequency versus the temperatures. Only training data are shown, Table 1.3. All nine estimated natural frequencies are shown in Appendix A.2.

Different observations can be noticed when three of the AR coefficients, Equation (1.14), are illustrated versus the temperature, Figure 1.13. Some influence by the temperature can be observed, but the tendency can be unclear. However, a non-linear tendency is observed, definitely.

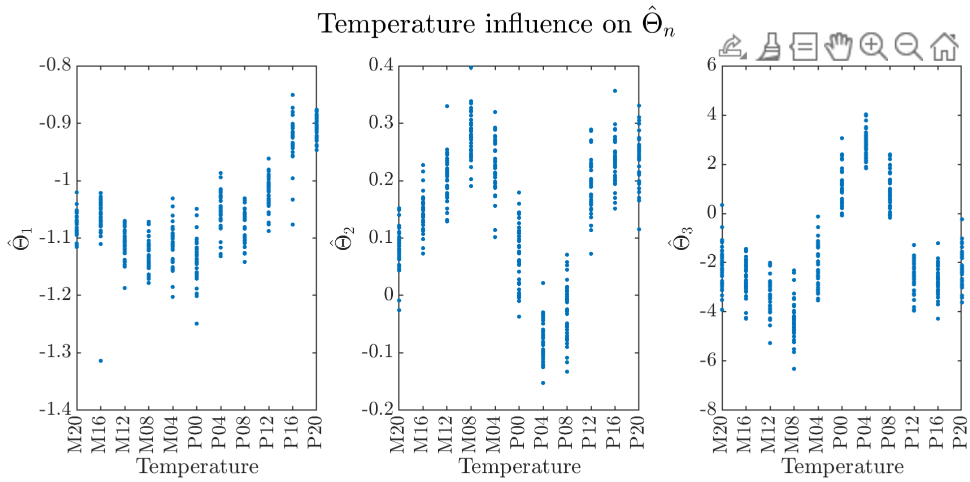

Figure 1.13: Visualization of the three first estimated AR coefficients versus the temperatures. Only training data are shown, Table 1.3.

Lastly, when the estimated damping ratios are shown versus the temperature, Figure 1.14, significant variability is observed. Some might be caused by the temperature, but the majority is caused by poor estimates [1].

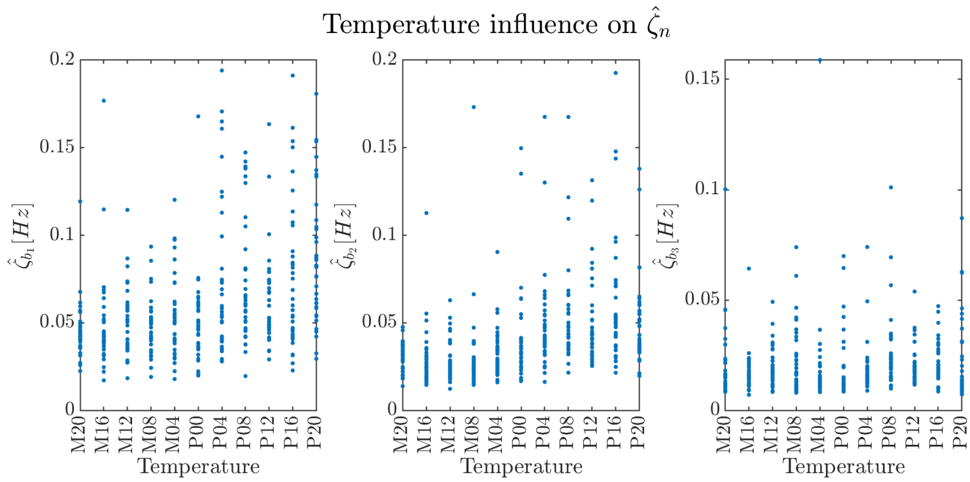

Figure 1.14: Visualization of the three bending modes estimated damping ratios versus the temperatures. Only training data are shown, Table 1.3. All nine estimated damping ratios are shown in Appendix A.3

.

The observed trends in the estimated natural frequencies are traced using Bayesian regression models, Section 1.3.1.1, where the polynomial order is selected by a thorough investigation of the MSE, Section 1.3.1.2. The posterior parameters, Equation (1.33-1.36), are updated 20 times since the parameters converged. The traced trends for the three bending modes in Figure 1.12 are shown in Figure 1.15.

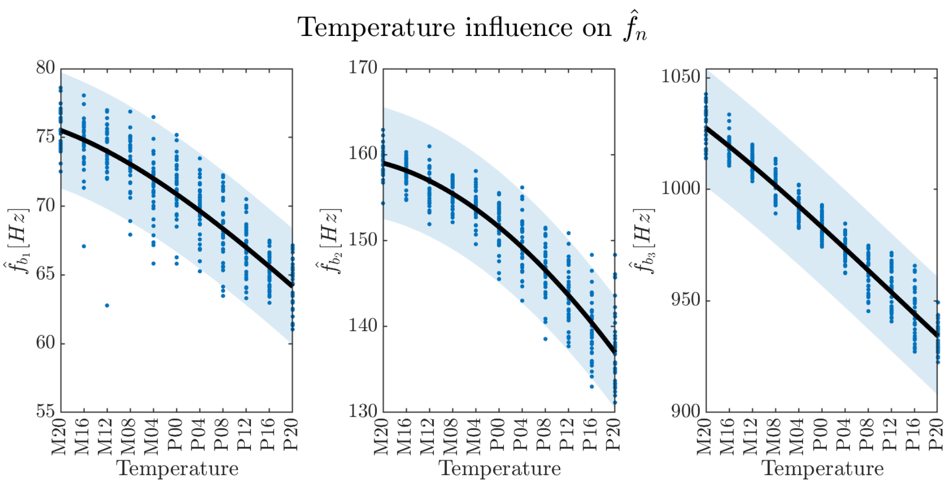

Figure 1.15: Bayesian regression model to trace the observed trend in the three bending modes estimated natural frequencies including the uncertainty bounds. The regression models are trained using the training data specified in Table 1.3.

A similar approach is pursued for the AR coefficients and the estimated damping ratios to trace the observable trend caused by the temperature. The traced trend for the first three AR coefficients and estimated damping ratios of the three bending modes are shown in Figure 1.16 and 1.17.

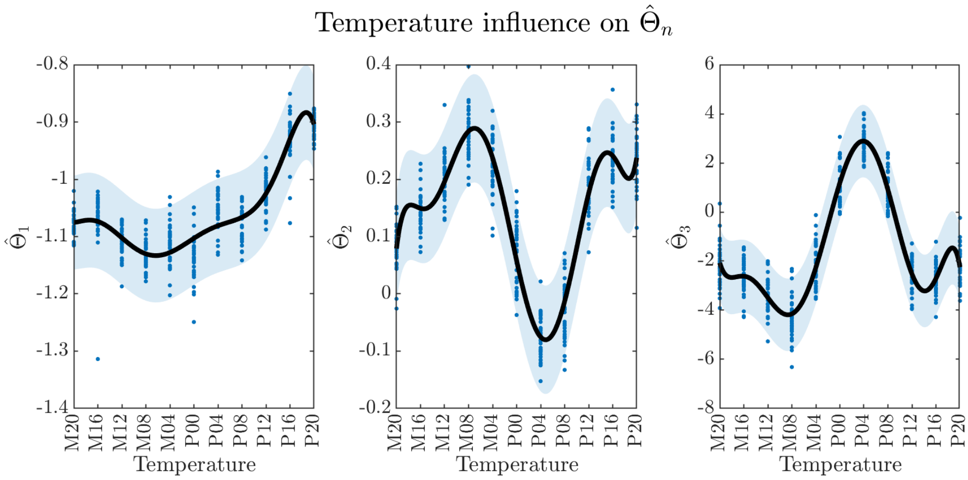

Figure 1.16: Bayesian regression model to trace the observed trend in the AR coefficients including the uncertainty bounds. The regression models are trained using the training data specified in Table 1.3.

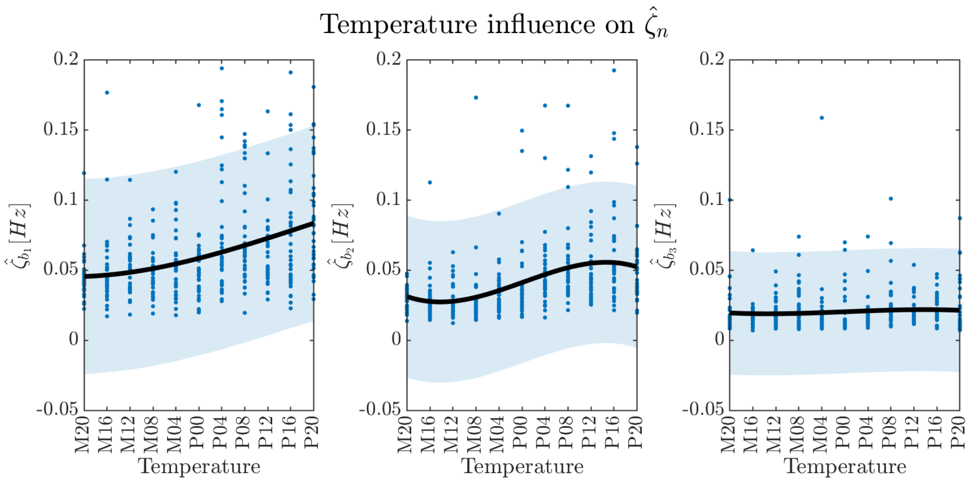

Figure 1.17: Bayesian regression model to trace the observed trend in the estimated damping ratios of the three bending modes including the uncertainty bounds. The regression models are trained using the training data specified in Table 1.3.

In the context of explicitly mitigate the variability caused by the temperature, those DSFs that are found to accept the regression models, with sufficient high F-statistic to reject the null hypothesis in Section 1.3.1.2, are adjusted according to the regression model:

$$\tilde{f}_i = f_i - \hat{f}_i(T) \tag{1.43}$$

$$\tilde{a}_i = a_i - \hat{a}_i(T) \tag{1.44}$$

$$\tilde{\zeta}_i = \zeta_i - \hat{\zeta}_i(T) \tag{1.45}$$

and those DSFs that reject the regression models, sufficient low F-statistic, are kept as original, yet normalized by the mean value obtained from the training set used for the regression models. The adjusted DSF, Equation (1.43-1.45), comprises the error between the estimated DSF and the traced trend rather than the original DSF.

1.3.2 Implicit method

The implicit methods comply with another approach where only the effect on the DSF are captured. Hence no measurements of EOPs are necessary. The approach relies solely on capturing the different patterns in the DSF of the reference state. One of the implicit approaches can be categorised as projection methods. The main proposition of projection methods is the projection of the DSF into a space where the effect of EOV can be eliminated more straightforwardly, to some extent. One such projection method is PCA. [17].

1.3.2.1 Principal Component Analysis

The PCA is a method to project the DSF into a new set of Cartesian coordinates with the dimension p, $(z_1, z_2, z_3, \ldots, z_p)$. The properties of the new coordinates, the *Principle Components* (PCs), is that the first PC is a linear combination of the original DSF which accounts for most of the variance. The second PC then explicate most of the remaining variance, and so forth for the dimension p, Figure 1.18. The main proposition is that the main part of the variance associated with the features originates from the EOV. Therefore, the first PCs are assumed to carry most of the influence caused by EOV.

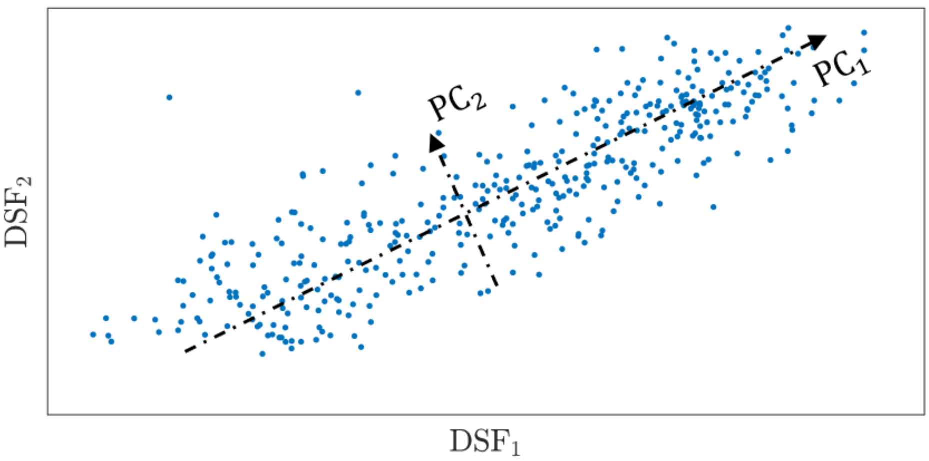

Figure 1.18: Visualization of two PCs of a set of two DSF. The first PC is a linear combination of the two originals DSF and accounts for most of the variance. The second PC is orthogonal to the first PC and accounts for most of the remaining variance. [15]

The transformation of the original DSF into the p-dimensional space are conducted by *Singular Value Decomposition* (SVD) of the covariance matrix of the DSF, defined as:

$$\boldsymbol{\Sigma} = \boldsymbol{X}^T \boldsymbol{X} \tag{1.46}$$

Where:

$\boldsymbol{X}$ = DSF matrix

The SVD of the DSF matrix can be expressed as:

$$\boldsymbol{X} = \boldsymbol{U} \cdot \begin{bmatrix} \boldsymbol{\Lambda} \\ 0 \end{bmatrix} \cdot \boldsymbol{V}^T \tag{1.47}$$

Where:

$\boldsymbol{U}$ = Left singular vector matrix
$\boldsymbol{V}$ = Right singular vector matrix
$\boldsymbol{\Lambda}$ = Diagonal singular matrix, $\boldsymbol{\Lambda}$ =diag$(\lambda_1, \lambda_2, \ldots, \lambda_p)$

By replacing the SVD of the DSF into the expression for the DSF covariance matrix, Equation (1.46), the following expression for the covariance matrix can be made:

$$\boldsymbol{\Sigma} = \boldsymbol{V} \cdot \begin{bmatrix} \boldsymbol{\Lambda} & 0 \end{bmatrix} \cdot \boldsymbol{U}^T \cdot \boldsymbol{U} \cdot \begin{bmatrix} \boldsymbol{\Lambda} \\ 0 \end{bmatrix} \cdot \boldsymbol{V}^T \tag{1.48}$$

which can be reduced due to orthogonality ($\boldsymbol{U}^T \cdot \boldsymbol{U} = \boldsymbol{I}$):

$$\boldsymbol{\Sigma} = \boldsymbol{V} \cdot \boldsymbol{\Lambda}^2 \cdot \boldsymbol{V}^T \tag{1.49}$$

It can be deduced from Equation (1.49) that the DSF covariance matrix has identical left and right singular vector matrices, which is equivalent to the right singular vector matrix. From Equation (1.46) and (1.49) an expression for the diagonal singular matrix takes the form of:

$$\boldsymbol{\Lambda}^2 = (\boldsymbol{X}\boldsymbol{V})^T \boldsymbol{X}\boldsymbol{V} \tag{1.50}$$

Then the transformed variables can be defined as:

$$\boldsymbol{Z}^T \boldsymbol{Z} = \boldsymbol{\Lambda}^2 \tag{1.51}$$

and combining Equation (1.50) and (1.51), the transformed variables, the PCs, can be calculated. [15, 20].

$$\boldsymbol{Z} = \boldsymbol{X} \cdot \boldsymbol{V} \tag{1.52}$$

1.3.2.2 Procedure

Since the first PCs, the PCs with the highest eigenvalue, carry most of the variance which are assumed to originate from EOV mainly, the first PCs should be removed before damage detection. If the cumulative variance according to the PCs is analyzed, Figure 1.19, it can be observed that many of the first PCs hold most of the total variance, and therefore, should be removed. Furthermore, the PCs with the lowest eigenvalue are assumed to contain noise mostly and should also be removed. [15, 31].

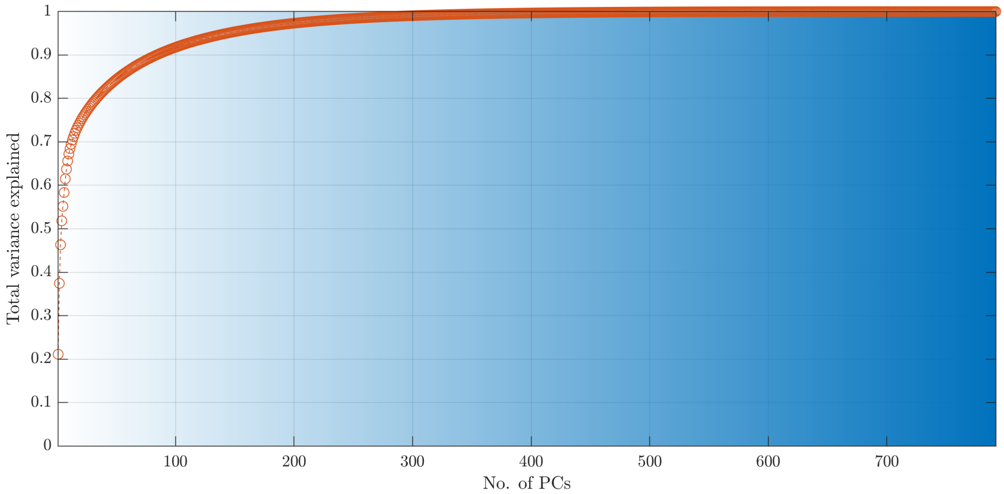

Figure 1.19: Cumulative variance plot according to the PCs, where the PCs are obtained from PCA of the AR coefficients.

The challenges arise when choosing the number of PCs to reject. Less literature exists guiding the removal of the first PCs, yet one approach is to select those PCs which constitute 95% of the total variance [4]. Another suggestion is to select those PCs which constitute at least 70% of the total variance [6].

1.3.3 Combined method

While several methods exist for mitigating the effect of EOV, e.g Bayesian regression as an explicit method and PCA as an implicit method, each has some disadvantages. A disadvantage of the explicit methods is the lack of measured EOPs. Furthermore, even if measured EOPs are available, it is not certain that the EOPs explain the variance of the DSF. A disadvantage of the implicit methods, the projection methods, is the consequence of an unsupervised/semi-supervised approach where the EOV not necessarily are removed from the damage state. Furthermore, in PCA, the removal of those PCs assumed to be sensitive to the EOV may contain information about damages. [15, 17]. Therefore, a proposed method combining the aforementioned approaches should be investigated. The main objective of the combined method is initially to follow the PCA methodology. To trace the variability in the PCs caused by the EOP, assumably the first PCs, Bayesian regression models are utilized. Those PCs which accept the proposed regression models are adjusted and the remaining are kept as original. The acceptance of the regression models is according to the F-statistic.

First, PCA of the DSF matrix, $\boldsymbol{X}$, are conducted by SVD as described in Section 1.3.2:

$$\boldsymbol{X} = \boldsymbol{U} \cdot \begin{bmatrix} \boldsymbol{\Lambda} \\ 0 \end{bmatrix} \cdot \boldsymbol{V}^T \tag{1.53}$$

$$\boldsymbol{Z} = \boldsymbol{X} \cdot \boldsymbol{V} \tag{1.54}$$

where the variability of the first three PCs with respect to the temperature is shown in Figure 1.20. Next, regression models for each PC, z_i, are trained with the known temperature as input:

$$z_i = \beta_0 + \beta_1 \cdot T + \beta_2 \cdot T^2 + \ldots + \beta_p \cdot T^p + \varepsilon_i \tag{1.55}$$

where the polynomial order of the regression model is chosen through an analysis of the MSE, Section 1.3.1.2. The trained regression models for the first three PCs are shown in Figure 1.21.

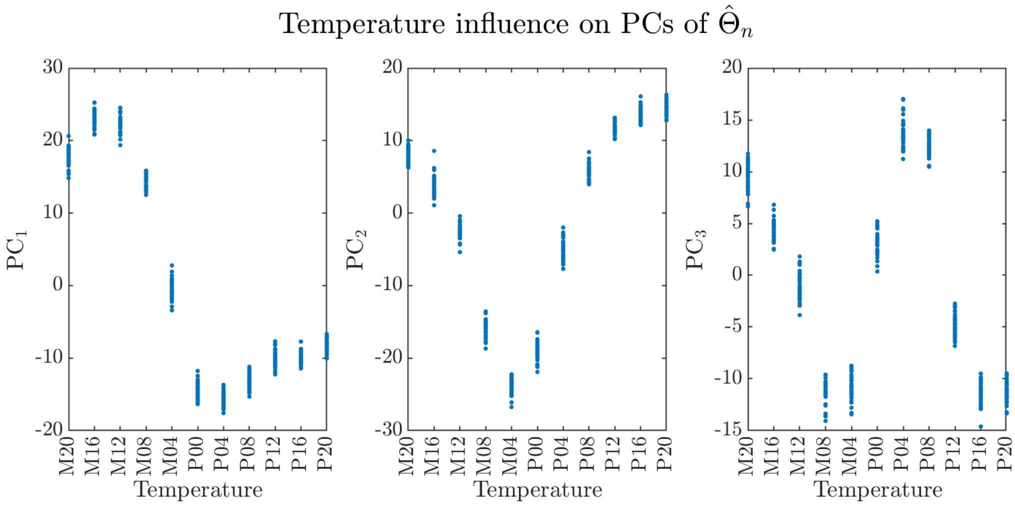

Figure 1.20: Effect on the first three PCs caused by the temperature. The PCs are the transformed coordinates of the AR coefficients.

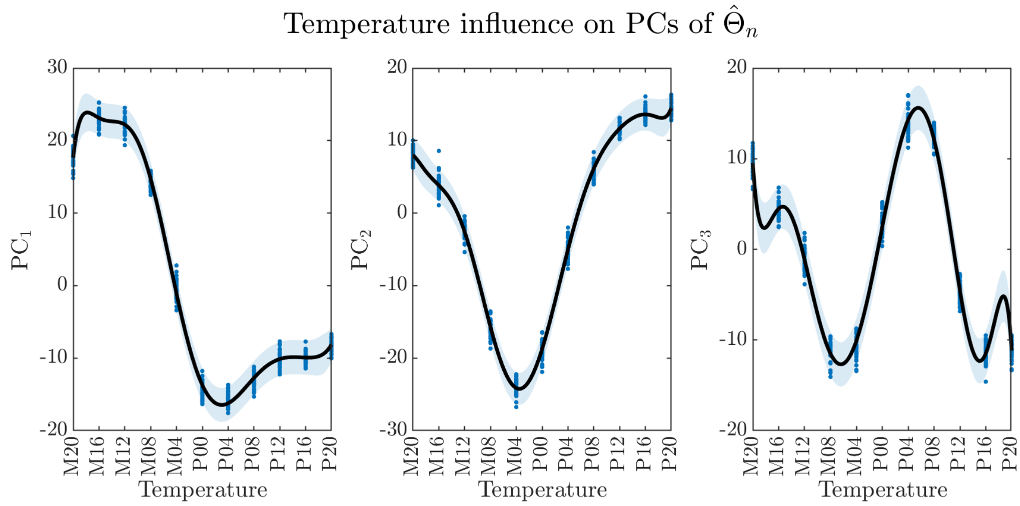

Figure 1.21: Bayesian nonlinear regression to trace the variability in the PCs. Here shown for the first three PCs of Figure 1.20

The regression models of each PC are evaluated individually. The null hypothesis is based on no evident correlation between the temperature and the PC. In opposition, the alternative hypothesis is defined as a comprehensible relationship being established. Therefore, if the F-statistic is above a certain threshold, the null hypothesis is rejected:

$$F = \frac{(TSS - RSS) \cdot (n - p - 1)}{RSS \cdot p} > \vartheta \tag{1.56}$$

Where:

ϑ = Threshold in the F-statistic to reject the null hypothesis

and if the null hypothesis is rejected, a possible correlation between the EOP and the PC exists. Therefore, the PC is adjusted with the obtained regression model:

$$\tilde{z}_i = z_i - \hat{z}_i \tag{1.57}$$

and those PCs where the null hypothesis is not rejected are kept as original.

1.4 Classification

After extracting the DSF and mitigating the effect of EOV according to the observed pattern in the training data of the healthy state, Table 1.3, an outliers analysis is essential to determine the state of the blade. Consequently, the data should be either classified as healthy or damaged. Since the conditions of the blade are known, a comparative analysis of the proposed methods for mitigating the effect of EOV can be performed. For the multivariate data, a vector comprising of the selected DSF for a specific dataset, the i^{th} dataset, the squared Mahalanobis distance is utilized to assess the condition of the blade as a one-class classifier [15, 17]. The squared Mahalanobis distance is calculated for each DSF vector, where each DSF vector comprises a set of selected DSF obtained from the i^{th} dataset:

$$d^2\left(\tilde{\boldsymbol{X}},\hat{\boldsymbol{\Sigma}}_u\right) = \tilde{\boldsymbol{X}}^T \hat{\boldsymbol{\Sigma}}_u^{-1} \tilde{\boldsymbol{X}} \tag{1.58}$$

Where:

$\tilde{\boldsymbol{X}}$ = Vector of corrected (or original) DSF according to Section 1.3.1, 1.3.2 and 1.3.3.

$\hat{\boldsymbol{\Sigma}}_u$ = Covariance matrix of the corrected (or original) DSF obtained from the training data.

The condition of the blade is then assessed by comparing the squared Mahalanobis distance, Equation (1.58), to a predefined threshold, ϑ. Consequently, written as the following hypotheses, which are comparable to the null hypothesis. Hypothesis H_u indicates that no damage is present, whereas the hypothesis H_d assesses that a damage is present:

$$\mathrm{H}_u : d^2\left(\tilde{\boldsymbol{X}},\hat{\boldsymbol{\Sigma}}_u\right) \leq \vartheta \rightarrow \text{Healthy} \tag{1.59a}$$

$$\mathrm{H}_d : d^2\left(\tilde{\boldsymbol{X}},\hat{\boldsymbol{\Sigma}}_u\right) > \vartheta \rightarrow \text{Damaged} \tag{1.59b}$$

Several approaches to setting a suitable threshold can be taken to estimate whether or not the given squared Mahalanobis distance indicates a damaged state of the blade. The approach taken throughout this study is derived in the ensuing section.

1.5 Damage detection

To classify whether or not the indices of the squared Mahalanobis distances belong to the healthy class or the damaged class, the hypotheses in Equation (1.59), a threshold, ϑ, is required. One approach is to obtain the optimum threshold by examining the level of correct classified indices, namely *True Positive* (TP) alarms and *True Negative* (TN) alarms, versus the false classified indices, *False Positive* (FP) alarms and *False Negative* (FN) alarms, for a vast range of thresholds. However, a more analytical approach exists comprised using the squared Mahalanobis distances sorted from the lowest value to the highest as a threshold vector for the actual distances. Subsequently, counting the TP alarms and FP alarms for each index of the threshold vector yields the rate of FP alarms versus the rate of TP alarms. Due to simplicity and to eliminate the risk of biasing the result towards a high rate of TP alarms with a high rate of FP alarms, the latter approach is utilized for classification, where the classification is performed for the healthy state versus the different conditions of the blade individually.

First, after the calculation of the squared Mahalanobis distances, Equation (1.58), a sorting ranking from the lowest value to the maximum defines the threshold vector for the given conditions individually. Therefore, four threshold vectors in total for each damage detection technique (the chosen DSF with a specific method to mitigate the effect of EOV) are defined. The four threshold vectors comprise classification between healthy versus damage 1, healthy versus damage 2, healthy versus damage 2 with water applied, and healthy versus all conditions, Figure 1.22.

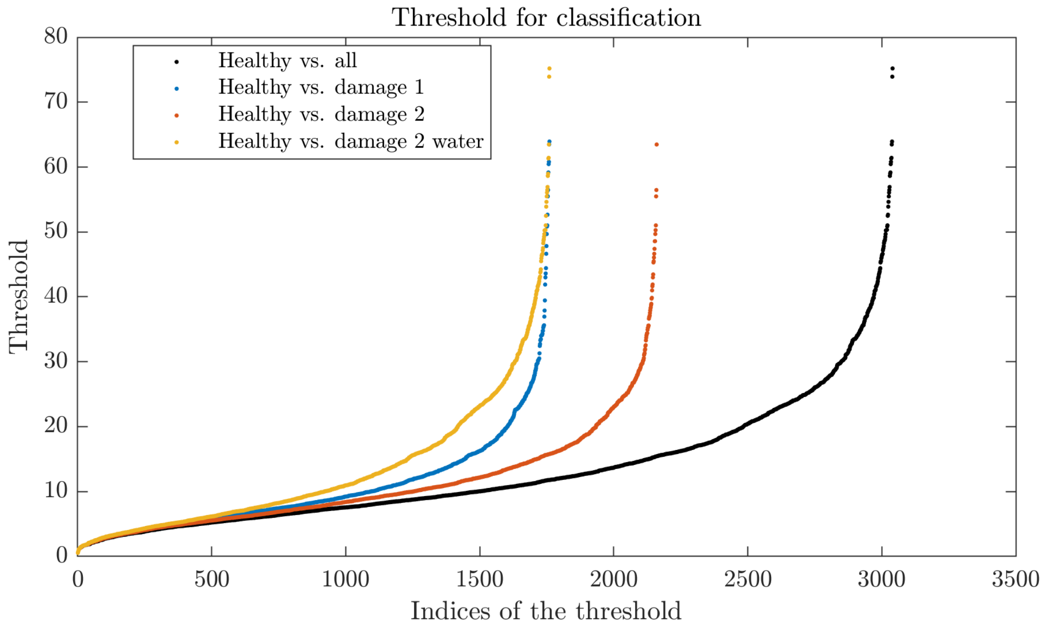

Figure 1.22: Threshold vector used for classification of the four conditions

The classification procedure involves the knowledge of the actual conditions. The procedure is then to analyze the squared Mahalanobis distances for each index of the threshold vector, Figure 1.22. Those distances that are known to belong to the damaged class and are above the current index of the threshold vector, are classified as TP alarms. Opposite to those distances that are known to belong to the healthy class but are above the current index of the threshold vector which then is classified as FP alarms. Subsequently, the performance of the damage detection approach can easily be assessed by analyzing the rate of TP alarms versus the rate of FP alarms for the defined threshold vector. This graphical illustration is known as the *Receiver Operating Characteristic* (ROC) curve, Figure 1.23.

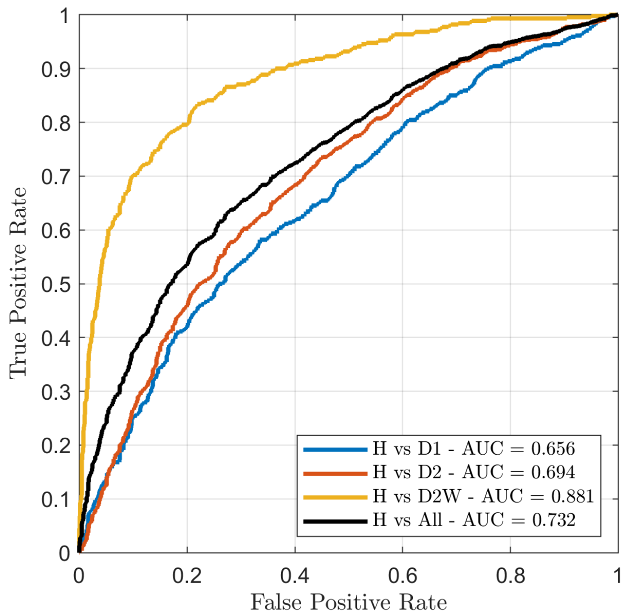

Figure 1.23: ROC curve for a graphical presentation of the TP rate versus the FP rate for the four different settings - healthy versus damage 1, healthy versus damage 2, healthy versus damage 2 with water, and healthy versus all conditions.

More pronounced the performance is measured in terms of the *Area Under the Curve* (AUC) of the given ROC curve. Desirable is 100% of TP alarms without any FP alarms, indicated by an AUC value of one. Therefore, the utility of the proposed DSF for an SHM system is investigated by a thorough analysis of the ROC curve in the ensuing chapter. Furthermore, the effect of EOV is mitigated by either the explicit method, the implicit method, or the combined method.

Results

To ease the presentation of the results, the section will be divided into main sections comprising the proposed DSF. As suggested in Section 1.3, three distinct approaches to mitigate the influence of EOV are implemented for each DSF. Furthermore, damage detection without compensating for the effect of EOV serves as a reference. The damage detection approach is build upon the one-class classifier, the squared Mahalanobis distance. Subsequently, the analysis of the ROC curve would be the baseline for a comparative analysis of the chosen DSF, as well as the proposed methods to mitigate the effect of EOV, Figure 2.1.

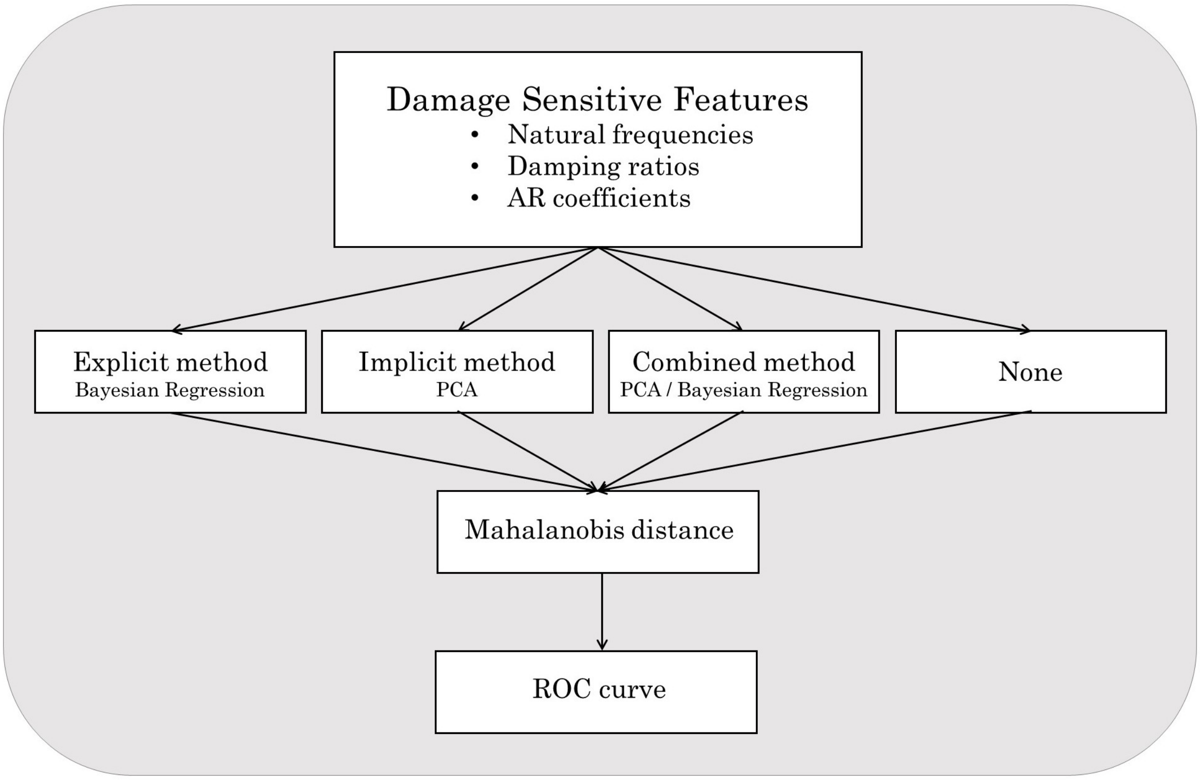

Figure 2.1: Flow chart of the presentation of the results

2.1 Natural Frequencies

To extract the estimated natural frequencies from the proposed VAR-model, Equation (1.17), reference frequencies obtained from peak-picking of the PSD were used to calculate the Euclidean distance, Equation (1.22). Subsequently, the frequencies obtained at a temperature of $0°C$ are stated in Table 1.4. This procedure is accompanied by some challenges since variability in the natural frequencies due to temperature changes are inevitable. To conquer this issue, peak-picking of the PSD for each training dataset is conducted to trace the change in reference frequencies due to temperature changes. The traced natural frequency references for each mode in Table 1.4 are shown in Appendix A.1.

2.1.1 Explicit compensation

As proclaimed in Section 1.3.1.2, by the utilization of the F-statistic it can be determined which estimated natural frequency that accepts the regression model of the variability due to the temperature changes. Although an F-statistic above the value of one should be sufficient to reject the null hypothesis, an adequate threshold should be determined.

First, through an investigation of the MSE for increasing polynomial order of the regression model, Appendix A.4, a polynomial order of three is chosen. Then, a thorough examination of the ROC curve derived an adequate threshold of one. The chosen threshold yielded the acceptance of all nine regression models obtained from training data of the healthy state without water applied, Figure 2.2.

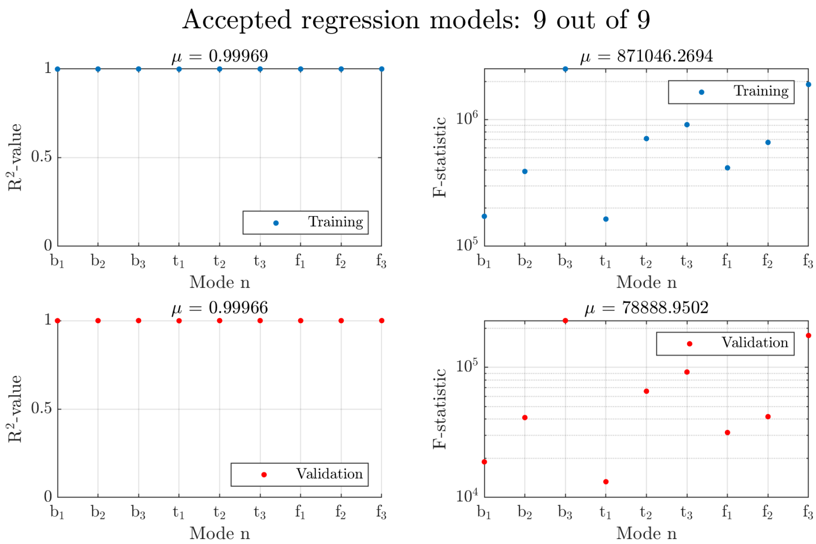

Figure 2.2: R^2 for both the training and validation data of the healthy state, Table 1.3. For both instances, the value is close to one indicating an acceptable fit. Furthermore, due to the high F-statistic, all regression models are adopted with high confidence.

Since all the estimated natural frequencies accepted their regression model, the mitigation of the influence of the EOP, namely the measured temperature, is accomplished by Equation (1.43). The compensation yields the residuals of the estimated natural frequencies, referred to as the adjusted natural frequencies, for the nine estimated natural frequencies of dataset i:

$$\tilde{\boldsymbol{f}}_i = \boldsymbol{f}_i - \hat{\boldsymbol{f}}(T) \tag{2.1}$$

Then, the estimated natural frequencies for all available datasets are adjusted and gathered in a single DSF matrix:

$$\tilde{\boldsymbol{X}} = \begin{bmatrix} \tilde{\boldsymbol{f}}_1 & \tilde{\boldsymbol{f}}_2 & \dots & \tilde{\boldsymbol{f}}_i \end{bmatrix}^T \tag{2.2}$$

Subsequently, to calculate the squared Mahalanobis distance given in Equation (1.58), the covariance of the healthy training data is calculated using the available training data (both the healthy state and the healthy state with water applied, Table 1.3):

$$\hat{\boldsymbol{\Sigma}}_u = \tilde{\boldsymbol{X}}_*^T \tilde{\boldsymbol{X}}_* \tag{2.3}$$

Where:

$\tilde{\boldsymbol{X}}_*$ = Comprises the adjusted natural frequencies obtained from the specified training data from both the healthy state and the healthy state with water applied

Then the squared Mahalanobis distance of each index of $\tilde{\boldsymbol{X}}$ can be evaluated for the purpose of damage detection, Figure 2.3. No distinct separations between the different conditions of the blade are observed complicating the process of detection damages.

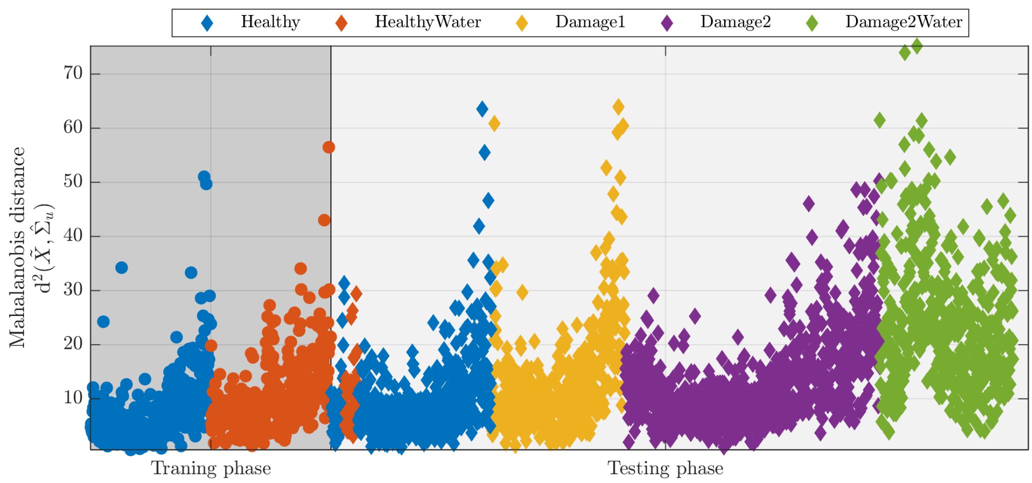

Figure 2.3: Squared Mahalanobis distances for all the adjusted natural frequencies according to Equation 2.1

Lastly is only to evaluate the ROC curve to assess the performance of the damage detection using natural frequencies estimated from VAR-models as DSF. Furthermore, explicitly compensating for the temperature change, Figure 2.4.

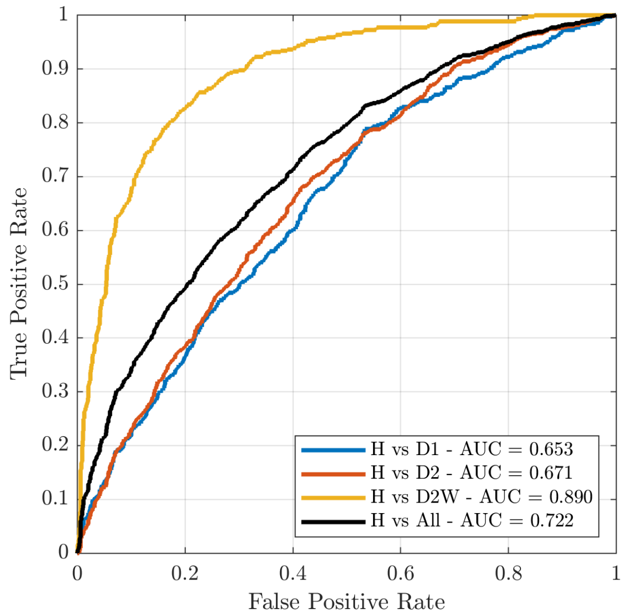

Figure 2.4: ROC curve for the explicit adjusted estimated natural frequencies obtained from VAR-modelling

The AUC for the ROC curves shown in Figure 2.4 for the healthy case versus the different introduced damages is presented in Table 2.1. Especially for the healthy state versus damage 2 with water applied an acceptable rate of TP alarms is present. Acceptable overall performance can be deduced but improvement is desirable.

Cases	AUC [%]
Healthy versus Damage 1	65.3
Healthy versus Damage 2	67.1
Healthy versus Damage 2 with water	89.0
Healthy versus All	72.2

Table 2.1: AUC for the different cases. Healthy comprises the healthy state and the healthy state with water applied during the experiment

2.1.2 Implicit compensation

While the objective of the previous section was to mitigate the influence of the temperature changes explicitly, the objective of the forthcoming section is to implicit mitigate the influence of EOV. The procedure of extracting the estimated natural frequencies is identical to the procedure in the latter section. The nine estimated natural frequencies from each dataset, $\boldsymbol{f}_i$, are gathered in a DSF matrix as:

$$\boldsymbol{X} = \begin{bmatrix} \boldsymbol{f}_1 & \boldsymbol{f}_2 & \dots & \boldsymbol{f}_i \end{bmatrix}^T \tag{2.4}$$

Then, the calculation of the transformed variables follows the methodology stated in Section 1.3.2.1 where the covariance matrix is defined similarly as Equation (2.3):

$$\hat{\boldsymbol{\Sigma}}_u = \boldsymbol{X}_*^T \boldsymbol{X}_* \tag{2.5}$$

Where:

$\boldsymbol{X}_*$ = Comprises the estimated natural frequencies obtained from the specified training data from both the healthy state and the healthy state with water applied

Then by the SVD decomposition of the training DSF matrix $\boldsymbol{X}_*$:

$$\boldsymbol{X}_* = \boldsymbol{U} \cdot \begin{bmatrix} \boldsymbol{\Lambda} \\ 0 \end{bmatrix} \cdot \boldsymbol{V}^T \tag{2.6}$$

the PCs can be obtained as:

$$\boldsymbol{Z} = \boldsymbol{X} \cdot \boldsymbol{V} = \begin{bmatrix} z_1 & z_2 & \dots & z_i \end{bmatrix}^T \tag{2.7}$$

The main objective when PCA is utilized to mitigate the influence of EOV is the removal of the first PCs since these are assumed to bear most of the variability caused by EOV. The complex aspect of this procedure is the selection of the first PCs as stated in Section 1.3.2.2. Prospectively, those PCs which constitute at least 90% of the total variance are kept. By the means of the total variance of the PCs obtained from the estimated natural frequencies, the first two PCs are rejected since the first two PCs are below the 90% threshold, Figure 2.5.

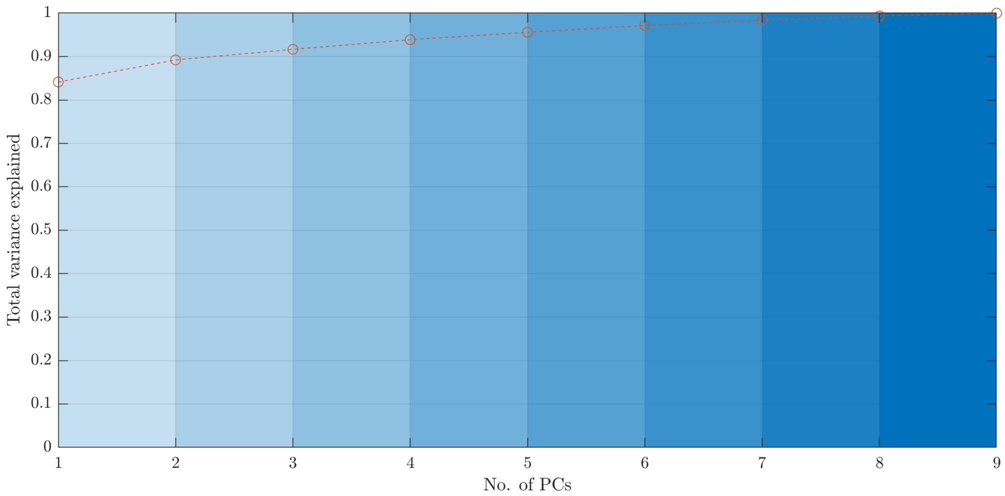

Figure 2.5: The total variance explained by the PCs obtained from the estimated natural frequencies

With the rejection of the first two PCs, the squared Mahalanobis distance would be of a vector containing the third PC up to the ninth PC for each dataset:

$$\mathbf{z}_i = \begin{bmatrix} z_3 & z_4 & \dots & z_9 \end{bmatrix}_i^T \tag{2.8}$$

The squared Mahalanobis distance of each vector, $\mathbf{z}_i$, is defined as:

$$d^2(\mathbf{z}_i) = \mathbf{z}_i^T \mathbf{\Lambda}^{-2} \mathbf{z}_i \tag{2.9}$$

where the Mahalanobis distance for the available datasets after implicitly compensating the effect of EOV in the estimated natural frequencies are presented in Figure 2.6. Similar to the latter section, no distinct clusters are observed, yet some of the damage conditions tend to have more variance compared to the healthy state.

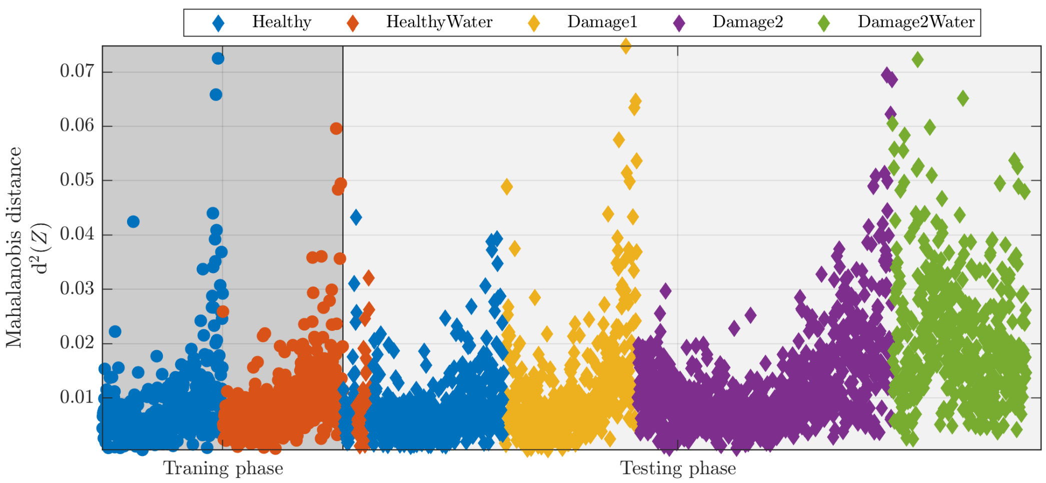

Figure 2.6: Squared Mahalanobis distance for the third PC up to the last PC obtained from the estimated natural frequencies

With the calculated squared Mahalanobis distance of each PC vector, z_i, where the first two are rejected, the graphical illustration of the FP alarms versus the TP alarms can be performed in terms of the ROC curve, Figure 2.7.

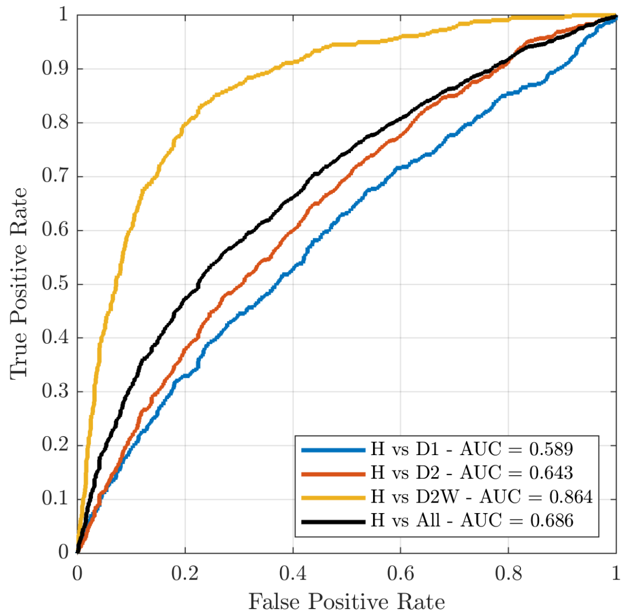

Figure 2.7: ROC curve for the estimated natural frequencies where the influence of EOV is implicit mitigated by the use of PCA

To clarify the performance of the damage detection approach the AUC of the ROC curve is presented in Table 2.2. The approach is while using estimated natural frequencies and implicit mitigate the effect of EOV.

Cases	AUC [%]
Healthy versus Damage 1	58.9
Healthy versus Damage 2	64.3
Healthy versus Damage 2 with water	86.4
Healthy versus All	68.6

Table 2.2: AUC for the different cases. Healthy comprises the healthy state and the healthy state with water applied during the experiment

A minor reduction in the performance of the damage detection method is observed, Table 2.2, compared to Table 2.1 although the utilized DSF are identical.

2.1.3 Combined compensation

To improve the performance of the damage detection, a combined approach to mitigate the effect of EOV is suggested in Section 1.3.3. The procedure is similar to the above-mentioned section except for the rejection of the first PCs. Regression models of each PC are obtained using Bayesian non-linear regression, Section 1.3.1.1, with the measured temperature as input. The polynomial order is set to eight by an examination of the MSE with an increasing polynomial order, Appendix A.4. Then, those PC which accepts their regression model are adjusted according to Equation (1.57).

The choice of an adequate threshold in the F-statistic stem from an investigation of the ROC curve with different thresholds. Subsequently, a suitable threshold in the F-statistic appears to be a value of one. With the specified threshold, all PCs accepted their regression model where the regression models are trained using training data from the healthy state without water applied, Figure 2.8. However, low R^2 values indicate either poor fits or high level of variance in the PCs. Since the F-statistics are assumed to be high enough to deduce a correlation between the measured temperatures and the variability in each PC, a vector containing the nine PCs for each dataset are adjusted using the obtained regression models:

$$\tilde{z}_i = z_i - \hat{z}(T) \tag{2.10}$$

and then gathered in one matrix as:

$$\tilde{\boldsymbol{Z}} = \begin{bmatrix} \tilde{z}_1 & \tilde{z}_2 & \dots & \tilde{z}_i \end{bmatrix}^T \tag{2.11}$$

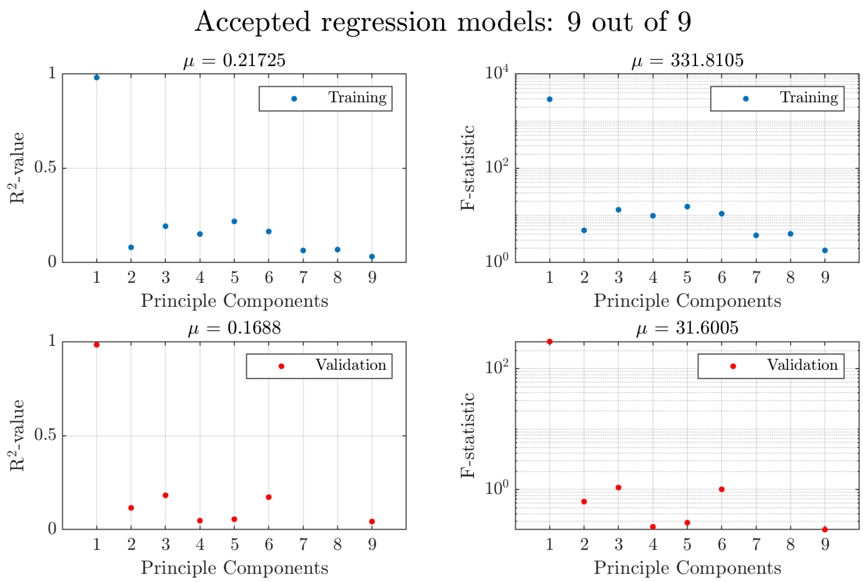

Figure 2.8: Statistics of the accepted regression models. Poor R^2 values are observed yet the F-statistic is above the specified threshold

After mitigating the influence of temperature changes in the PCs, the squared Mahalanobis distance can be calculated similarly to Equation (2.9). However, the adjusted PC vector, $\tilde{\boldsymbol{Z}}_i$, is used for each dataset:

$$d^2(\tilde{\mathbf{Z}}_i) = \tilde{\mathbf{Z}}_i^T \boldsymbol{\Lambda}^{-2} \tilde{\mathbf{Z}}_i \tag{2.12}$$

The squared Mahalanobis distances for all available datasets are presented in Figure 2.9.

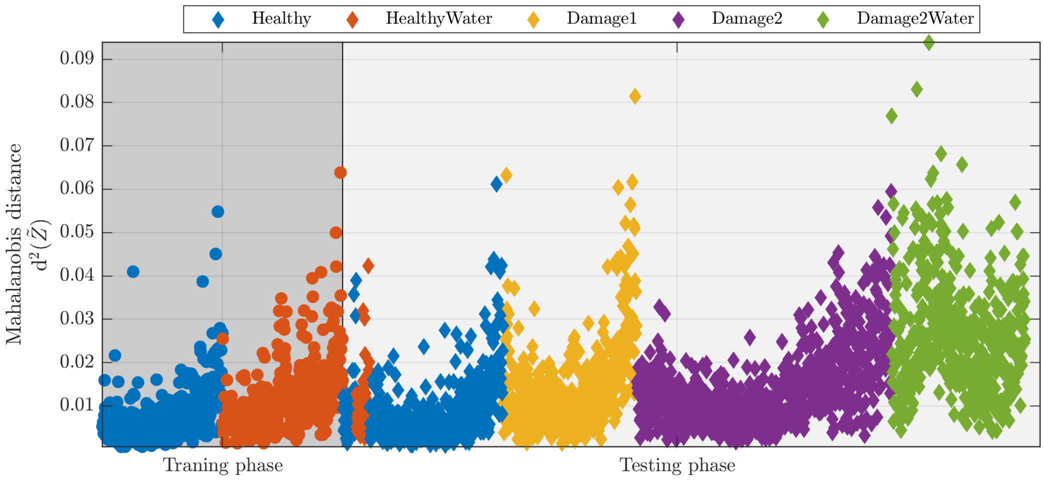

Figure 2.9: Squared Mahalanobis distance of the adjusted PCs

If the squared Mahalanobis distances, Figure 2.9, are compared to squared Mahalanobis distances for the explicit and implicit approach for mitigating the effect of EOV, Figure 2.3 and 2.6, a distinct difference is complicated to deduce. Therefore, in terms of comparative analysis, the ROC curve is presented, Figure 2.10.

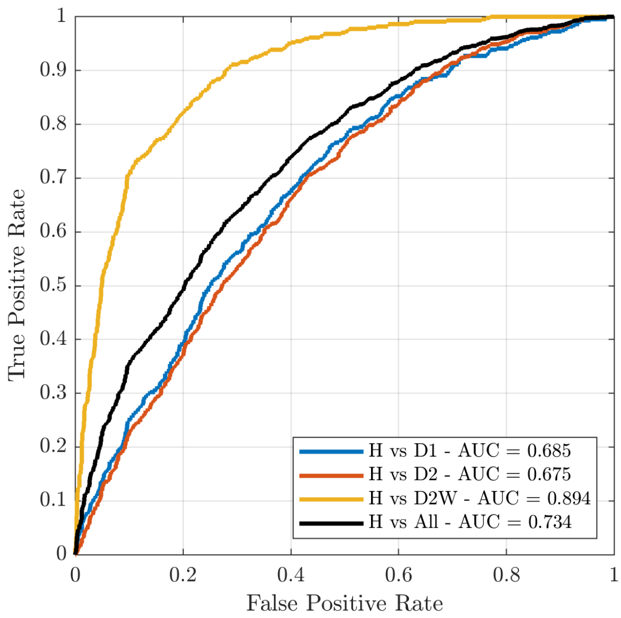

Figure 2.10: ROC curve for the estimated natural frequencies where the effect of temperature changes are compensated in the PCs, Section 1.3.3

and a clarification of the AUC of the ROC curves for the damage detection method is shown in Table 2.3. The method is based on the utilization of the natural frequencies as DSF and the effect of EOV is mitigated with a combined method.

Cases	AUC [%]
Healthy versus Damage 1	68.5
Healthy versus Damage 2	67.5
Healthy versus Damage 2 with water	89.4
Healthy versus All	73.4

Table 2.3: AUC for the different cases. Healthy comprises the healthy state and the healthy state with water applied during the experiment

Compared to the previous two sections concerning the explicit and implicit methods, in general, a minor improvement is observed indicating the advantage of the combined method where none of the PCs are rejected.

2.1.4 No compensation

To identify which of the proposed methods to mitigate the effect of EOV are most efficient for this setup, each method should be compared to a damage detection approach without any compensation. Therefore, the squared Mahalanobis distance is calculated directly from the nine estimated natural frequencies from dataset i:

$$d^2\left(\boldsymbol{f}_i, \hat{\boldsymbol{\Sigma}}_u\right) = (\boldsymbol{f}_i - \boldsymbol{\mu}_*)^T \hat{\boldsymbol{\Sigma}}_u^{-1} (\boldsymbol{f}_i - \boldsymbol{\mu}_*) \tag{2.13}$$

Where:

$\boldsymbol{f}_i$ = Vector comprising the nine estimated natural frequencies from VAR-modelling of dataset i

$\hat{\boldsymbol{\Sigma}}_u$ = Covariance matrix of the estimated natural frequencies only for the healthy training state (Both healthy state and healthy state with water applied)

$\boldsymbol{\mu}_*$ = Mean value of the estimated natural frequencies only for the healthy training state, with and without water applied

The squared Mahalanobis distances for all available datasets, Figure 2.11, do not contain any observable separation equivalent to the previous observations, Figure 2.3, 2.6 and 2.9.

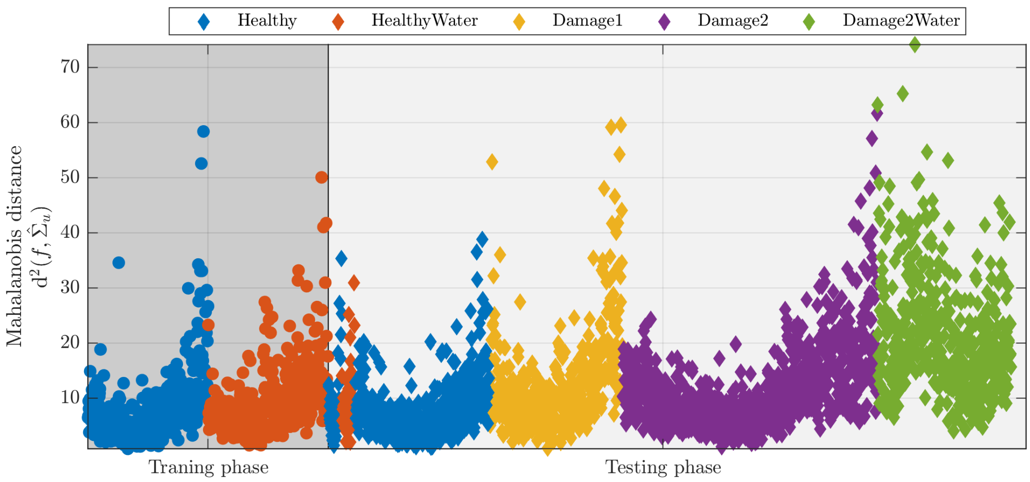

Figure 2.11: Squared Mahalanobis distance of the estimated natural frequencies

Afterwards, an analysis of the ROC curve provides a more accurate estimation of the damage detection performance. The approach is with the utility of estimated natural frequencies without any compensation, Figure 2.12.

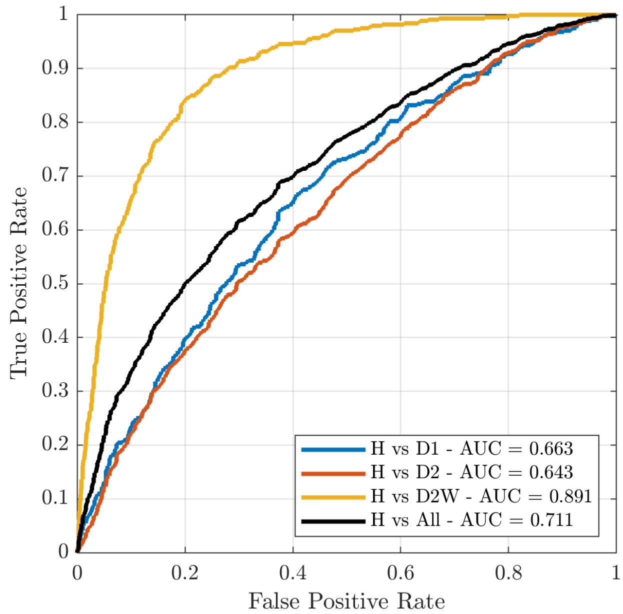

Figure 2.12: ROC curve for the squared Mahalanobis distances of the estimated natural frequencies without any compensation

and the associated AUC for each of the conditions to assess the performance of the damage detection approach, Table 2.4.

Cases	AUC [%]
Healthy versus Damage 1	66.3
Healthy versus Damage 2	64.3
Healthy versus Damage 2 with water	89.1
Healthy versus All	71.1

Table 2.4: AUC for the different cases. Healthy comprises the healthy state and the healthy state with water applied during the experiment

The AUC in Table 2.4 serves as a reference to deduce if the previous three sections improve the performance of detection damages. Both the explicit method and the combined implicit/explicit have higher AUC values than the reference. In addition, the implicit method have a reduced performance compared to the reference.

2.2 Damping Ratios

After extraction of the estimated natural frequencies, Section 2.1, the appertaining damping ratios can be determined according to Equation (1.18). The same indices of Equation (1.16) as for the estimated natural frequencies are utilized. These damping ratios are gathered in a vector containing nine damping ratios for each dataset. Then each vector is used as DSF while the proposed methods to mitigate the effect of EOV are utilized in the ensuing sections.

2.2.1 Explicit compensation

To trace the influence caused by the temperature changes, the MSE of increasing polynomial order is examined to select a suitable order for the Bayesian non-linear regression models. The examination led to a polynomial order of five, Appendix A.5. Next is to determine a suitable threshold for the F-statistic to deduce which of the estimated damping ratios accept their regression model or not. By an investigation of the ROC curve for different thresholds, a suitable threshold is set to 200. Thereby, six of the nine estimated damping ratios in total accepted their regression model. The regression models are trained using training data of the healthy state without water applied, Figure 2.13.

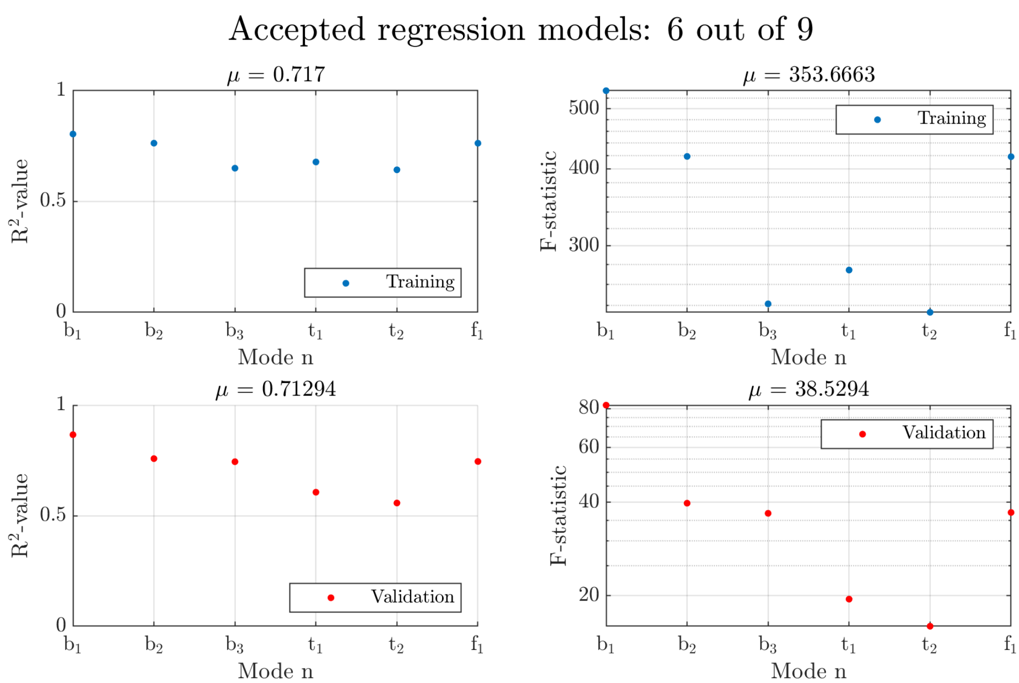

Figure 2.13: 6 out of 9 of the damping ratios accepted their regression model with the specified threshold. An acceptable R^2-value is observed both for the training and validation set (healthy state without water). Furthermore, the level of F-statistics appears to be sufficient to accept the regression models.

For those estimated damping ratios that accepted the regression model, the estimated damping ratio is compensated using the regression model. For those estimated damping ratios that rejected their regression model, the mean value is subtracted. The mean value is obtained from the training data of the healthy state without water applied. For dataset i this is expressed as:

$$\tilde{\boldsymbol{\zeta}}_i = \begin{bmatrix} \zeta_{b_1} \\ \zeta_{b_2} \\ \zeta_{b_3} \\ \zeta_{t_1} \\ \zeta_{t_2} \\ \zeta_{t_3} \\ \zeta_{f_1} \\ \zeta_{f_2} \\ \zeta_{f_3} \end{bmatrix}_i - \begin{bmatrix} \hat{\zeta}_{b_1} \\ \hat{\zeta}_{b_2} \\ \hat{\zeta}_{b_3} \\ \hat{\zeta}_{t_1} \\ \hat{\zeta}_{t_2} \\ \mu_{t_3} \\ \hat{\zeta}_{f_1} \\ \mu_{f_2} \\ \mu_{f_3} \end{bmatrix}_{(T)} \tag{2.14}$$

For the calculation of the squared Mahalanobis distances for all datasets, the approach is similar to the calculation of the squared Mahalanobis distances in Section 2.1.1. The DSF vector, $\tilde{\boldsymbol{X}}$, comprises the nine estimated damping ratios for each dataset:

$$\tilde{\boldsymbol{X}} = \begin{bmatrix} \tilde{\boldsymbol{\zeta}}_1 & \tilde{\boldsymbol{\zeta}}_2 & \dots & \tilde{\boldsymbol{\zeta}}_i \end{bmatrix}^T \tag{2.15}$$

All of the squared Mahalanobis distances are then evaluated, Figure 2.14.

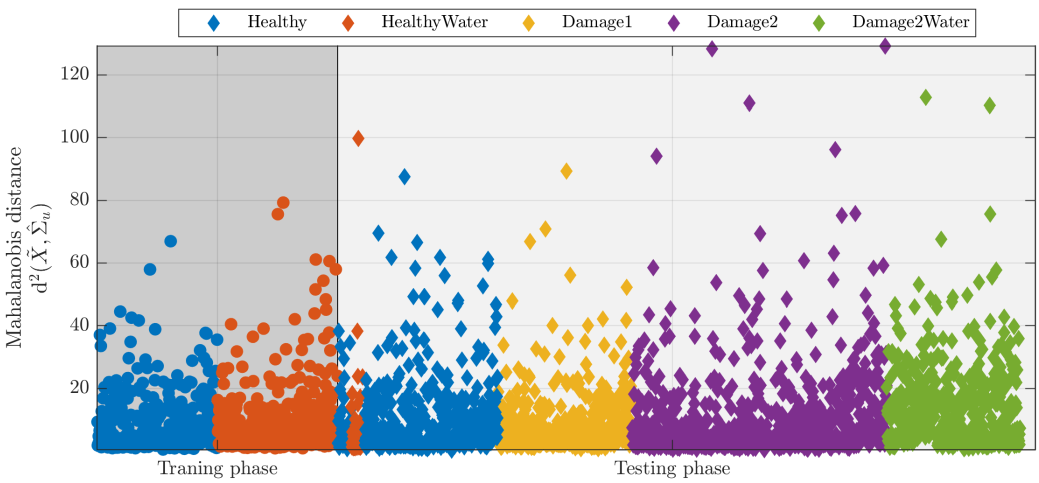

Figure 2.14: Squared Mahalanobis distances for the explicit compensated estimated damping ratios

No distinct clusters are observed between the different conditions of the blade, possibly reducing the performance of the damage detection approach. A more accurate evaluation of the performance is obtained by the ROC curve for each condition, Figure 2.15.

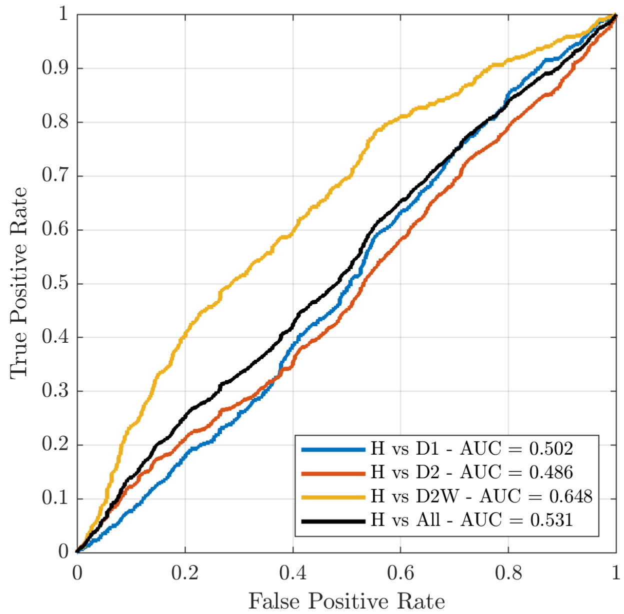

Figure 2.15: ROC curve when the damping ratios are used as DSF and the influence of temperature changes is explicit compensated in 6 out of 9 damping ratios.

Lastly, the AUC of the ROC curves are presented in Table 2.5 for clarification and to ease the accessibility. The individual and overall performances are poorly indicated by a ratio of nearly 50% FP alarms versus TP alarms.

Cases	AUC [%]
Healthy versus Damage 1	50.2
Healthy versus Damage 2	48.6
Healthy versus Damage 2 with water	64.8
Healthy versus All	53.1

Table 2.5: AUC for the different cases. Healthy comprises the healthy state and the healthy state with water applied during the experiment

2.2.2 Implicit compensation

The procedure in Section 1.3.2 to implicit mitigate the effect of EOV is utilized similarly to the implicit compensation of the estimated natural frequencies, Section 2.1.2. The only exception is the usage of the estimated damping ratios as DSF. First, the cumulative variance for each PCs is calculated to deduce the rejection process of those PCs which are assumed to bear most of the variability caused by EOV. According to the statement in Section 2.1.2, only the eighth and ninth PC are chosen due to the 90% threshold of the total variance, Figure 2.16.

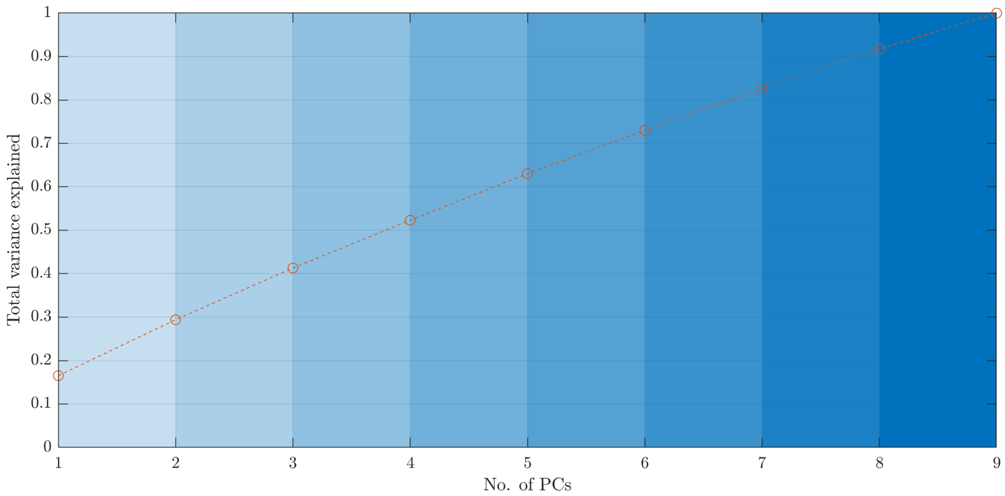

Figure 2.16: The cumulative variance of the PCs obtained from a transformation of the estimated damping ratios

With the rejection of most of the PCs, the squared Mahalanobis distance for each dataset, both testing and training, are evaluated similarly to Equation (2.9). The PC vector, z_i, comprises the eighth and ninth PC:

$$z_i = \begin{bmatrix} z_8 \\ z_9 \end{bmatrix} \tag{2.16}$$

A visual inspection of the squared Mahalanobis distances for all the available datasets reveals one common cluster rather than distinct clusters for each group of damage, Figure 2.17. This indicates poor damage detection performance similar to the aforementioned section.

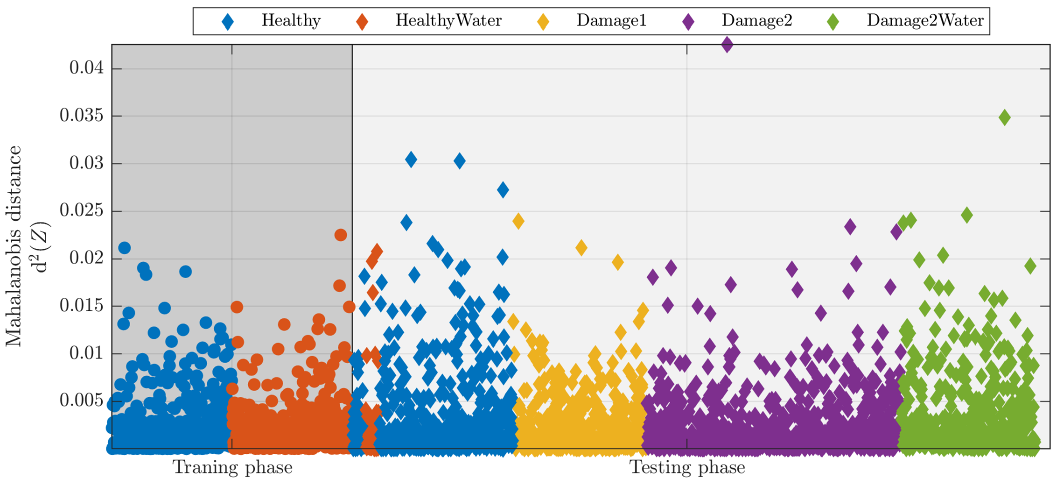

Figure 2.17: Squared Mahalanobis distances for the PCs obtained from the estimated damping ratios

To infer a poor damage detection performance while using estimated damping ratios as DSF and the effect of EOV is implicit mitigated, an analysis of the ROC curve is essential. The ability to detect damages for each condition of the blade is graphically illustrated in terms of FP alarms versus TP alarms, Figure 2.18.

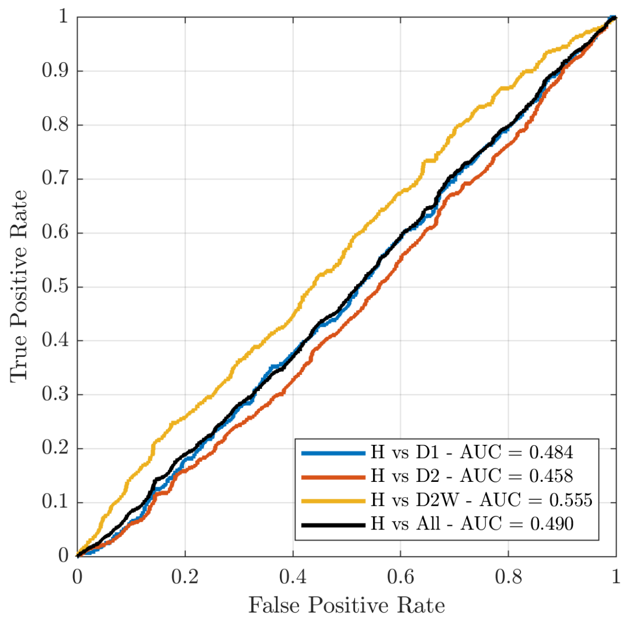

Figure 2.18: ROC curve to analyze the FP alarms versus the TP alarms

Further clarification of the performance is obtained by an analysis of the AUC for the ROC curves. The AUC for each scenario is given in Table 2.6. A minor reduction for all conditions is observed compared to Table 2.5 where the same estimated damping ratios are explicit compensated for the influence of the temperature changes. In general, the ratio of FP alarms versus TP alarms is around 50% which is inappropriate in the context of an SHM system.

Cases	AUC [%]
Healthy versus Damage 1	48.4
Healthy versus Damage 2	45.8
Healthy versus Damage 2 with water	55.5
Healthy versus All	49.0

Table 2.6: AUC for the different cases. Healthy comprises the healthy state and the healthy state with water applied during the experiment

2.2.3 Combined compensation

Since most of the PCs were rejected while following the PCA methodology, the proposed combined method, Section 1.3.3, could improve the ability to detect damages since all PCs are used. The procedure is to first transform the given variables to obtain the PCs. The SVD of the training data (both healthy state and healthy state with water) is used for this purpose. Next, instead of rejecting most of the PCs, regression models for each of PCs are trained to trace possible trends caused by temperature changes (training data for the regression models origins from the healthy state without water applied). By introducing a certain threshold in the F-statistics, each PC is adjusted if the regression model is accepted.

First, by an examination of the MSE for increasing polynomial order, a polynomial order of seven is chosen to trace the trend in the PCs, Appendix A.5. Then, by a thorough investigation of the ROC curve for different levels of threshold in the F-statistic, a threshold of one is chosen. Consequently, all nine regression models are accepted by their PC. The fit of the regression models is deficient indicated by a low R^2 although the F-statistics of the training data are above the specified threshold, Figure 2.19. This might be an indication of poor estimates. The adjustment of the nine PCs for dataset i is carried out as:

$$\tilde{z}_i = z_i - \hat{z}(T) \tag{2.17}$$

and the PCs for all available datasets are adjusted by the regression models trained using the specified training data:

$$\tilde{\boldsymbol{Z}} = \begin{bmatrix} \tilde{z}_1 & \tilde{z}_2 & \dots & \tilde{z}_i \end{bmatrix}^T \tag{2.18}$$

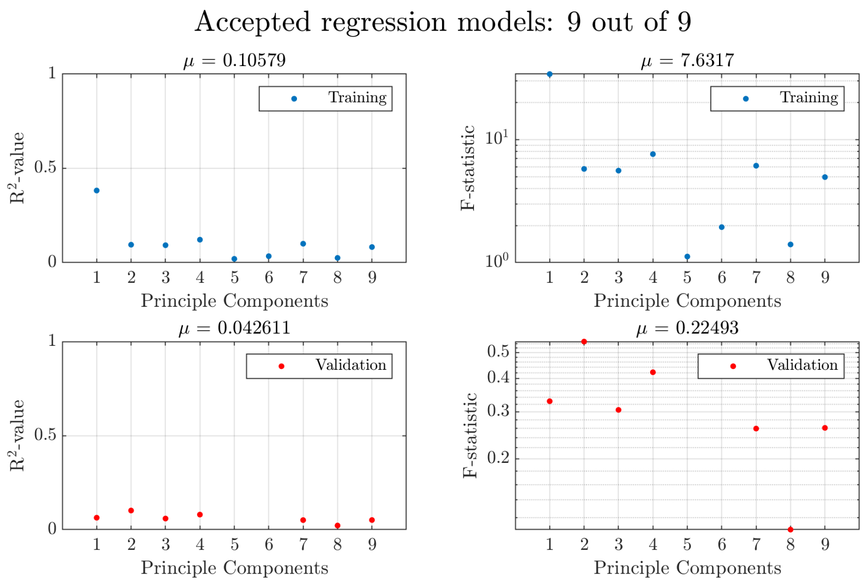

Figure 2.19: Measurements of how well the regression models fit the data utilizing the R^2 value and F-statistic

With the adjustment of the PCs for dataset i, the evaluation of the squared Mahalanobis distance can be performed similarly to Equation (2.12). The squared Mahalanobis distances for all datasets, Figure 2.20, does not indicate a proper damage detection performance using the estimated damping ratios as DSF and the proposed combined method to mitigate the effect of EOV. However, less variance is observed within each condition.

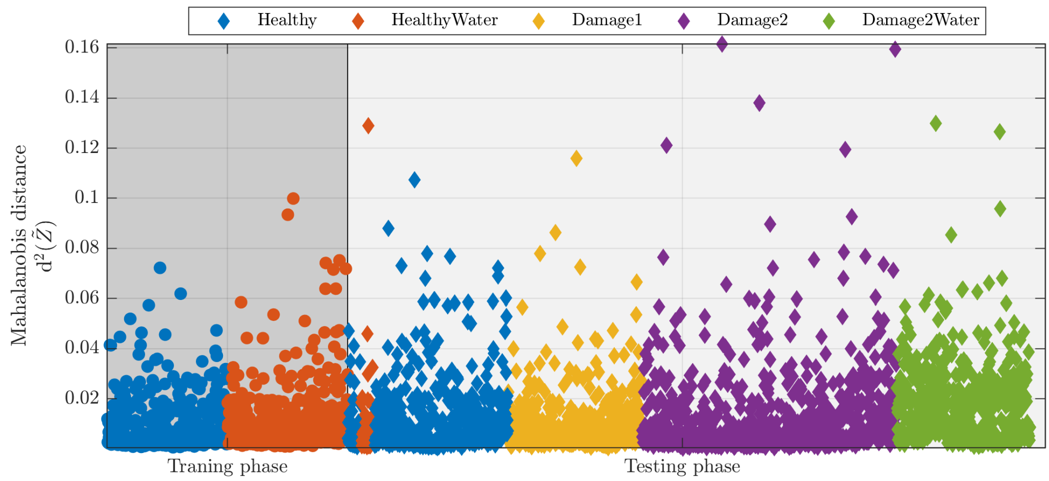

Figure 2.20: Squared Mahalanobis distance for each dataset when the estimated damping ratios as utilized as DSF and the proposed combined method to mitigate the effect of EOV is used

To analyze the damage detection performance, the ROC curve provides a better estimate of the performance. Diagonal lines indicate 50% possibility of TP alarms.

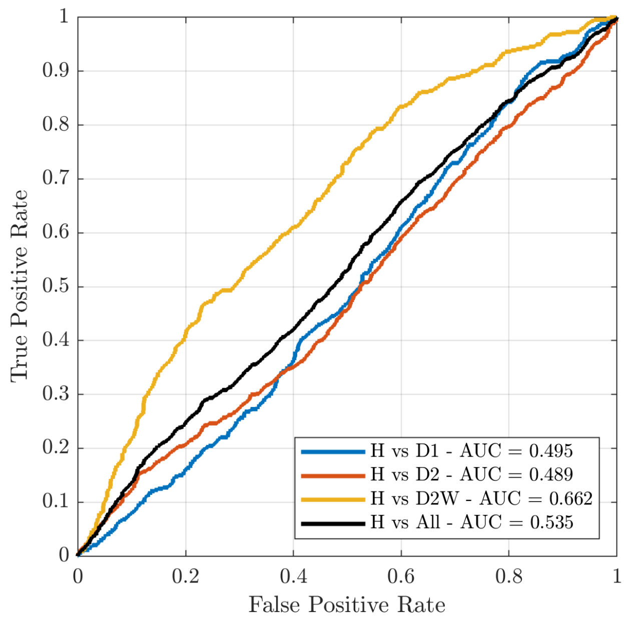

Figure 2.21: FP versus TP alarms of the damage detection technique

And lastly, the AUC of the ROC curves provides a clarification of the performance which will be used for the comparative analysis, Table 2.7. If Table 2.7 is compared to the latter section, Table 2.6, an improvement is observed using all PCs proposed in the combined methodology to mitigate the effect of EOV.

Cases	AUC [%]
Healthy versus Damage 1	49.5
Healthy versus Damage 2	48.9
Healthy versus Damage 2 with water	66.2
Healthy versus All	53.5

Table 2.7: AUC for the different cases. Healthy comprises the healthy state and the healthy state with water applied during the experiment

2.2.4 No compensation

In the aforementioned sections, the nine estimated damping ratios are used as DSF where the effect of EOV is mitigated both implicit, explicit and with a combination. To deduce the efficiency of the methods utilized to mitigate the effect of EOV, a damage detection technique straightly from the obtained DSF is performed.

The squared Mahalanobis distance can be calculated directly from the estimated damping ratios, comprised in a vector for each dataset:

$$\boldsymbol{\zeta}_i = \begin{bmatrix} \zeta_{b_1} & \zeta_{b_2} & \zeta_{b_3} & \zeta_{t_1} & \dots & \zeta_{f_1} & \dots & \zeta_{f_3} \end{bmatrix}_i^T \tag{2.19}$$

and with the mean value and covariance obtained from the training data, the squared Mahalanobis distance can be calculated as:

$$d^2(\boldsymbol{\zeta}_i, \hat{\boldsymbol{\Sigma}}_u) = (\boldsymbol{\zeta}_i - \boldsymbol{\mu}_*)^T \hat{\boldsymbol{\Sigma}}_u^{-1} (\boldsymbol{\zeta}_i - \boldsymbol{\mu}_*) \tag{2.20}$$

Where:

$\hat{\boldsymbol{\Sigma}}_u$ = Covariance matrix of the estimated damping ratios only for the healthy training state (Both healthy state and healthy state with water applied)

$\boldsymbol{\mu}_*$ = Mean value of the estimated damping ratios only for the healthy training state, with and without water applied

The squared Mahalanobis distance for each dataset, both training and testing datasets, are evaluated and illustrated in Figure 2.22. The damage detection performance can be complicated to deduce from an analysis of the squared Mahalanobis distance since no distinct separations are present.

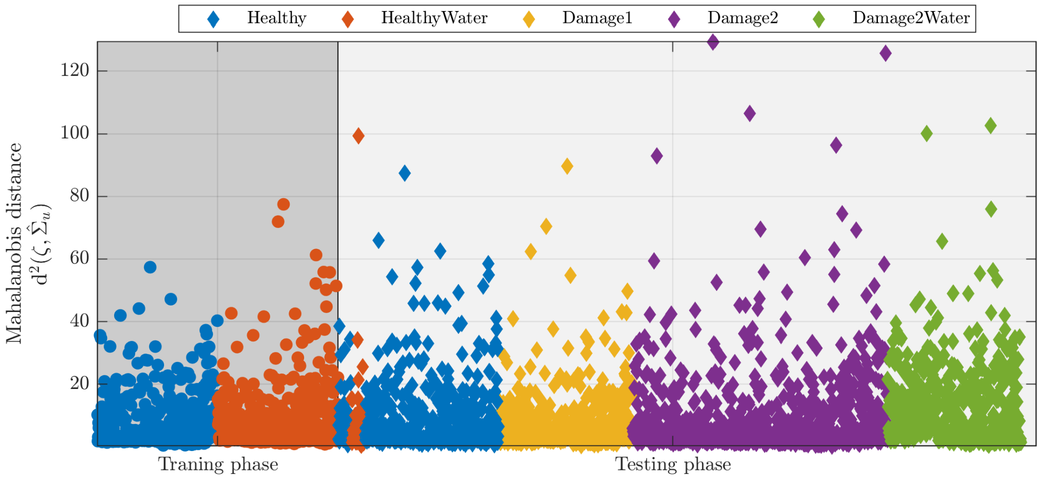

Figure 2.22: Squared Mahalanobis distance for each dataset when the estimated damping ratios are used as DSF. No compensation for the temperature changes is implemented

An estimate of the damage detection performance is more accurately obtained by an analysis of the ROC-curve, Figure 2.23. An improvement in the ability to detect the present damages is not seen.

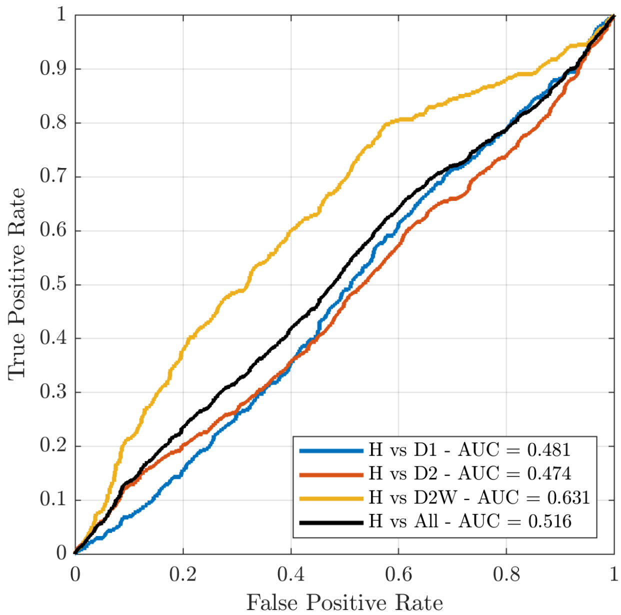

Figure 2.23: ROC curves for the different conditions of the blade using estimated damping ratios as DSF. Furthermore, no compensation for the temperature influence is done

Lastly, to clarify the performance of the damage detection technique, the AUC of the ROC curves are presented in Table 2.8. Although the ability to detect the damages is not improved, the performance is similar to previous sections, Section 2.2.1, 2.2.2 and 2.2.3, with minor variations.

Cases	AUC [%]
Healthy versus Damage 1	48.1
Healthy versus Damage 2	47.4
Healthy versus Damage 2 with water	63.1
Healthy versus All	51.6

Table 2.8: AUC for the different cases. Healthy comprises the healthy state and the healthy state with water applied during the experiment

2.3 AR coefficients

The previous sections were based on the modal parameters as DSF, namely the natural frequencies and damping ratios. The modal parameters were estimated using a VAR-model of the signals for each dataset. Specifically, the AR coefficients of the VAR-model are utilized to estimate the natural frequencies and damping ratios, Equation (1.17) and (1.18). Therefore, the AR coefficients are assumed to hold at least as much information of the damages as the estimated modal parameters derived from the coefficients. In Section 1.2.1.1 a model order of 65 is chosen for the VAR-models. Therefore, the amount of AR coefficients for each dataset is the model order, n_a, times the number of responses, n_p, squared:

$$N_\Theta = n_a \cdot n_p^2 = 65 \cdot 4^2 = 1040 \tag{2.21}$$

Whether or not the AR coefficients are affected by the temperature changes, or any other EOV, is unknown. Therefore, in the following sections the influence, if present, will be mitigated explicit, implicit and with a combination hereof to analyze the ability to detect the present damages.

2.3.1 Explicit compensation

For each AR coefficient obtained from the training datasets (healthy state without water applied), regression models are trained with the temperature as input to trace any variability. The variability is assumed to be caused by the temperature changes. If the AR coefficients accept their regression model by the means of a sufficient F-statistic, the variability is caused by the temperature changes. Consequently, the AR coefficients which have accepted their regression model are adjusted by subtracting the regression models. Furthermore, those AR coefficients that rejected their regression model are left as original except a normalization by the mean value is conducted.

By a thorough investigation of the MSE for increasing polynomial order of different AR coefficients, a polynomial order of eight is chosen for the regression models, Appendix A.6. Subsequently, a suitable threshold for the F-statistics to deduce whether or not the regression models are accepted is obtained by investigating the ROC curve for different levels of thresholds. A suitable threshold is chosen to be 350, contributing that 178 AR coefficients accepted their regression models. In general, the fit of the accepted regression models is acceptable indicated by a high R^2 value, Figure 2.24.

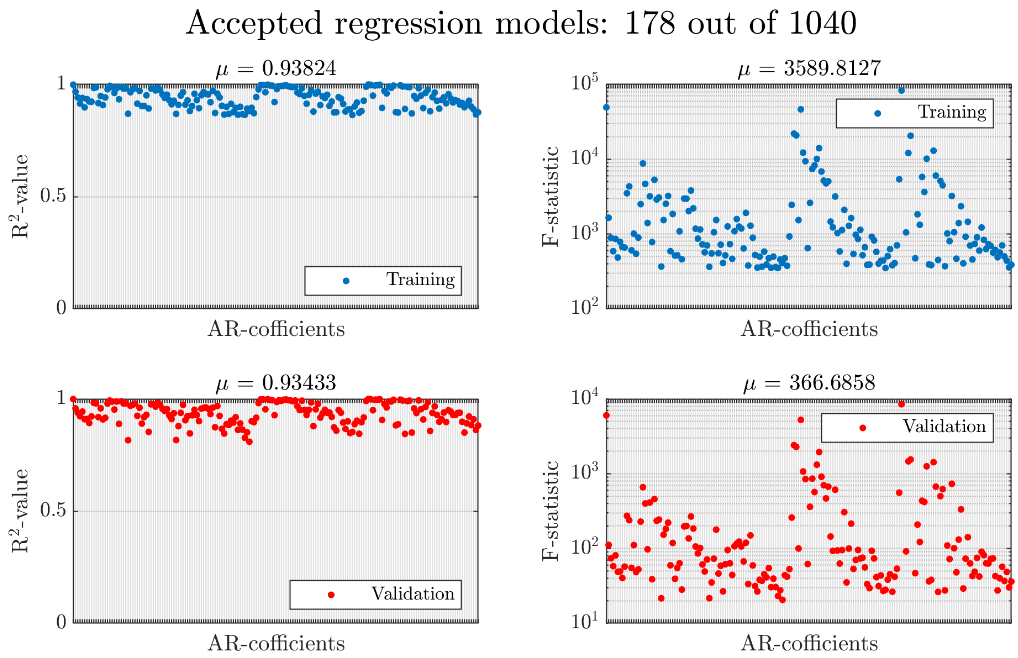

Figure 2.24: Statistics of the accepted regression models. Both the R^2 values and F-statistics indicates an acceptable fit

The indices of the AR coefficients that accepted their regression model in the training phase (using training data of the healthy state without water applied) are used to adjust the AR coefficients obtained from each dataset:

$$\tilde{\mathbf{\Theta}}_i = \mathbf{\Theta}_i - \hat{\mathbf{\Theta}}(T) \tag{2.22}$$

Where:

$\hat{\mathbf{\Theta}}(T) =$ Is a vector containing indices of all 1040 coefficients. The indices of the accepted regression models comprise the 178 accepted models. The indices of the rejected regression models are substituted by their mean value obtained from the same training data

After the adjustment of all coefficients for each dataset, the variables are gathered in a common DSF matrix:

$$\tilde{\boldsymbol{X}} = \begin{bmatrix} \tilde{\mathbf{\Theta}}_1 & \tilde{\mathbf{\Theta}}_2 & \ldots & \tilde{\mathbf{\Theta}}_i \end{bmatrix}^T \tag{2.23}$$

The covariance matrix, $\hat{\boldsymbol{\Sigma}}_u$, is calculated similar to Equation (2.3) while using the DSF matrix in Equation (2.23). The squared Mahalanobis distance of each index in $\tilde{\boldsymbol{X}}$ can be calculated as:

$$d^2(\tilde{\boldsymbol{X}}_i, \hat{\boldsymbol{\Sigma}}_u) = \tilde{\boldsymbol{X}}_i^T \hat{\boldsymbol{\Sigma}}_u^{-1} \tilde{\boldsymbol{X}}_i \tag{2.24}$$

All squared Mahalanobis distances are evaluated, Figure 2.25. Distinct clusters for each condition of the blade are observed indicating a high-performance damage detection technique.

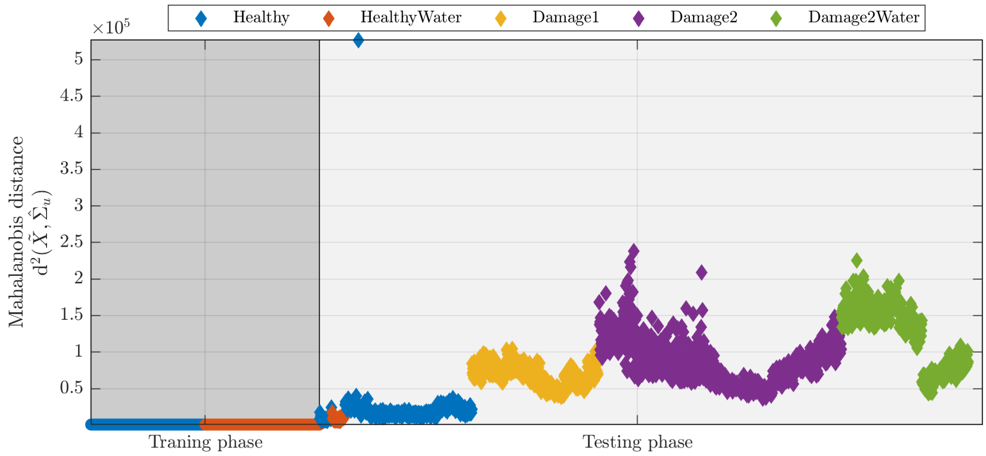

Figure 2.25: Squared Mahalanobis distances for the adjusted DSF comprised the AR coefficients

To deduce the performance of the damage detection technique where the AR coefficients are used as DSF and the influence of temperature changes are explicit compensated, the ROC curve is presented, Figure 2.26.

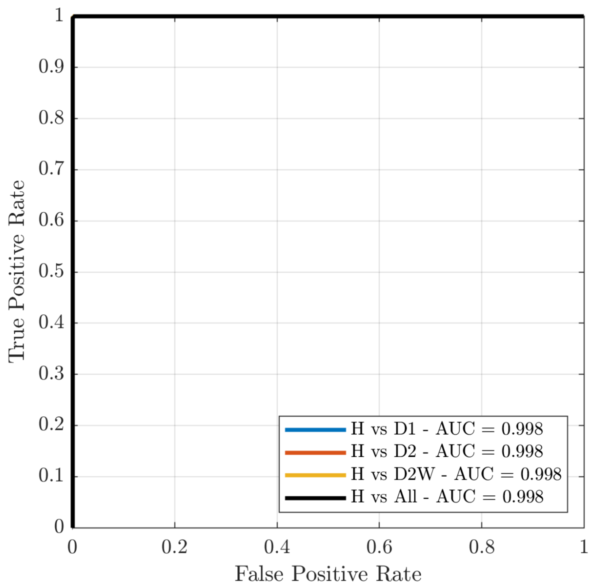

Figure 2.26: ROC curve for illustrating the performance of the damage detection technique

And lastly, the AUC of the ROC curves are presented for clarification, Table 2.9. A high TP rate is present, indicating the AR coefficients are sensible towards the introduced damages after explicit mitigate the influence of temperature changes.

Cases	AUC [%]
Healthy versus Damage 1	99.8
Healthy versus Damage 2	99.8
Healthy versus Damage 2 with water	99.8
Healthy versus All	99.8

Table 2.9: AUC for the different cases. Healthy comprises the healthy state and the healthy state with water applied

2.3.2 Implicit compensation

In the latter section, the AR coefficients were revealed to be sensitive towards the introduced damages after the influence of temperature changes is mitigated. The latter approach was with an explicit compensation. In the following section, the effect of EOV is mitigated implicit by the use of the proposed PCA methodology. The AR coefficients for each dataset are gathered in a common DSF matrix:

$$\boldsymbol{X} = \begin{bmatrix} \boldsymbol{\Theta}_1 & \boldsymbol{\Theta}_2 & \dots & \boldsymbol{\Theta}_i \end{bmatrix}^T \tag{2.25}$$

then by SVD of the training indices of $\boldsymbol{X}$ (both the healthy state and healthy state with water applied), the right singular vector matrix, $\boldsymbol{V}$, is obtained. The right singular vector matrix is then used for transformation of the DSF according to Section 1.3.2:

$$\boldsymbol{Z} = \boldsymbol{X} \cdot \boldsymbol{V} \tag{2.26}$$

To deduce the rejection of the first PCs, the cumulative variance of the PCs is evaluated, Figure 2.27. As stated in Section 2.1.2 those PCs below a threshold of 90% of the total variance are rejected. Therefore, the first 83 PCs are rejected out of 792 PCs in total for each dataset. Furthermore, the last 92 PCs are also rejected since it is assumed that they comprise noise, primarily.

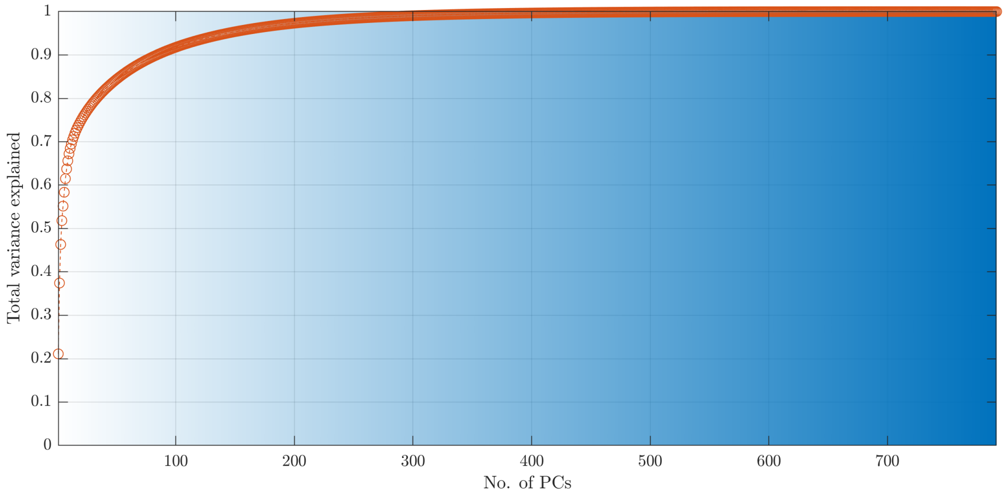

Figure 2.27: Cumulative variance of the PCs obtained from the AR coefficients

Subsequently, the vector of PCs for each dataset after rejecting those PCs that are assumed to bear most of the influence caused by EOV takes the form of:

$$\mathbf{z}_i = \begin{bmatrix} z_{84} & z_{85} & \dots & z_{700} \end{bmatrix}^T \tag{2.27}$$

and the squared Mahalanobis distance for each dataset can be evaluated similarly to Equation (2.9) with the use of $\mathbf{z}_i$. An evaluation of the distances for all available datasets, Figure 2.28, showed distinct clusters for each of the conditions. However, less distinct clusters compared to the latter section.

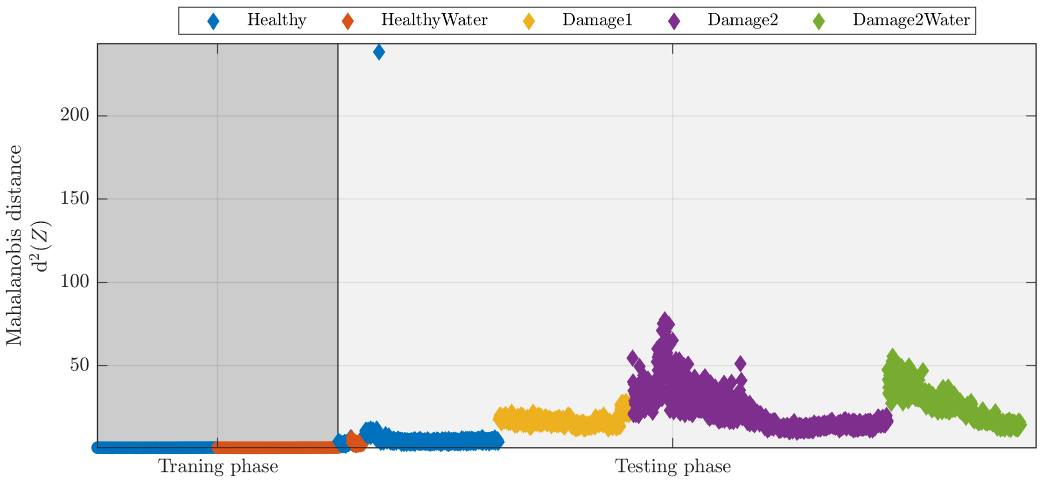

Figure 2.28: Squared Mahalanobis distances for all available data when the effect of EOV is implicit mitigated with the use of PCA

The probability of detecting damages, the TP alarms, is illustrated against the probability of detecting false damages, the FP alarms, to visualize the performance of the proposed damage detection approach, Figure 2.29. The ROC curve indicates almost perfect damage detection with a high rate of TP alarms with almost no FP alarms.

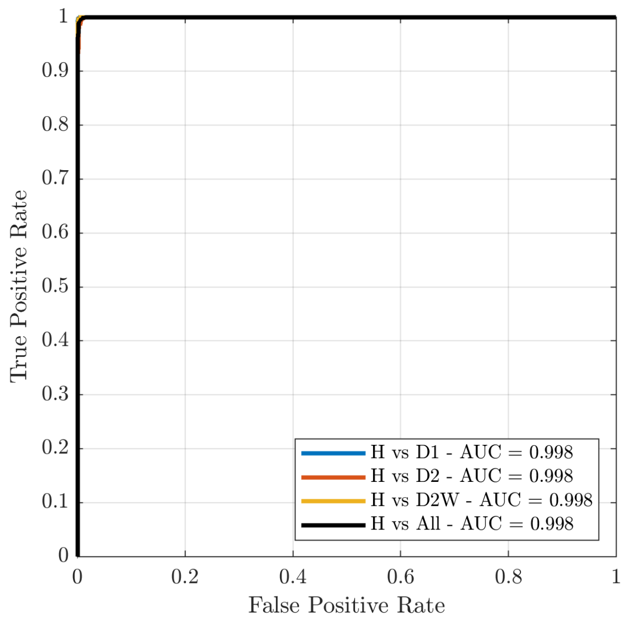

Figure 2.29: The probability of TP alarms versus the probability of FP alarms graphical illustrated by the ROC curve

Exactly how accurate the damage detection approach emerges to be is clarified by the AUC for the ROC curves, Table 2.10. For all indices of damages introduced, the AUC is close to one. A value close to one indicates TP alarms with almost no FP alarms. The performance is practically identical to the latter section. A close inspection of the upper left corner of the ROC curve indicates a slight reduction compared to the latter section, yet not significant enough to be measurable by the first decimal of the AUC-values.

Cases	AUC [%]
Healthy versus Damage 1	99.8
Healthy versus Damage 2	99.8
Healthy versus Damage 2 with water	99.8
Healthy versus All	99.8

Table 2.10: AUC for the different cases. Healthy comprises the healthy state and the healthy state with water applied

2.3.3 Combined compensation

Despite the previous sections showing accurate detection of the damaged states, the combined method to mitigate the effect of EOV is investigated. The procedure is similar to the latter section except no PCs are rejected. Instead, regression models of each PC are trained using the specified training data (healthy state without water applied). Subsequently, by a sufficient level of F-statistics, some of the regression models are accepted and thereby the respective PC is adjusted. As a consequence, the first PCs are not rejected but utilized for damage detection. However, the last PCs are rejected due to noise similar to the previous section.

For determination of the polynomial order of the regression model, the MSE for an increasing polynomial order is analysed, Appendix A.6. The analysis led to a polynomial order of 10. Afterwards, an adequate threshold in the F-statistic for acceptance of the regression models is obtained by a thorough analysis of the ROC curve for different thresholds. The threshold is set to five, leading to the acceptance of 27 regression models out of 792 models in total, Figure 2.30. It is observed that the PCs which accepted their regression models primarily consist of the first PCs. This indicates the sensitivity towards the temperature changes are high for the first PCs.

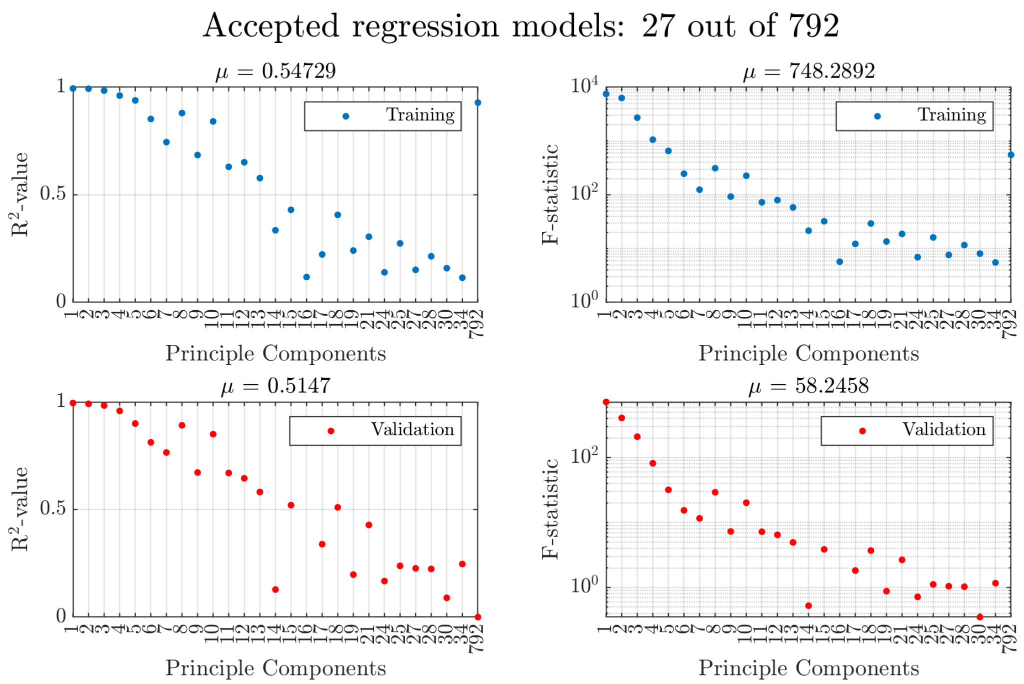

Figure 2.30: Fitness statistics of the accepted regression models by mean of the R^2 values and F-statistics

Those PCs that accepted their regression model are adjusted by subtracting the regression model leaving the residuals for further usage. Those PCs which rejected their regression model are kept as original. The PCs for dataset i then comprises 700 PCs, some adjusted and some not:

$$\tilde{z}_{i,[700\times1]} \tag{2.28}$$

which is gathered in a common DSF matrix for the PCs of all available datasets:

$$\tilde{\boldsymbol{Z}} = \begin{bmatrix} \tilde{z}_1 & \tilde{z}_2 & \ldots & \tilde{z}_i \end{bmatrix}^T \tag{2.29}$$

With the common DSF matrix, $\tilde{\boldsymbol{Z}}$, the squared Mahalanobis distance for each index of $\tilde{\boldsymbol{Z}}$ can be calculated to evaluate if the damage states can be detected by the suggested approach. The squared Mahalanobis distance for each index of $\tilde{\boldsymbol{Z}}$ can be calculated as Equation (2.12).

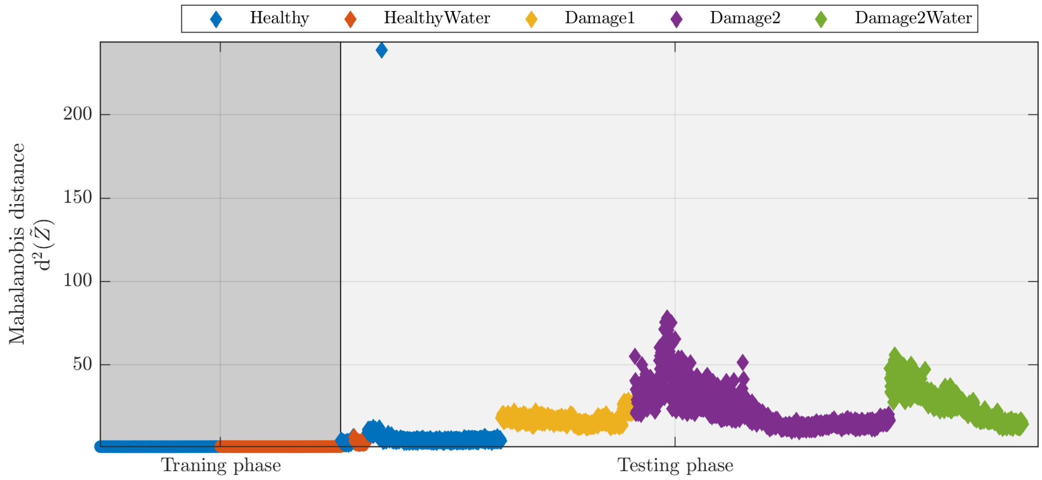

Figure 2.31: Squared Mahalanobis distances for each dataset, both training, validation and testing

The squared Mahalanobis distance for each dataset is evaluated, Figure 2.31. Evident clusters are observed similarly to the previous section where the effect of EOV was implicit mitigated. A performative analysis of the damage detection approach utilizing the ROC curve is presented in Figure 2.32.

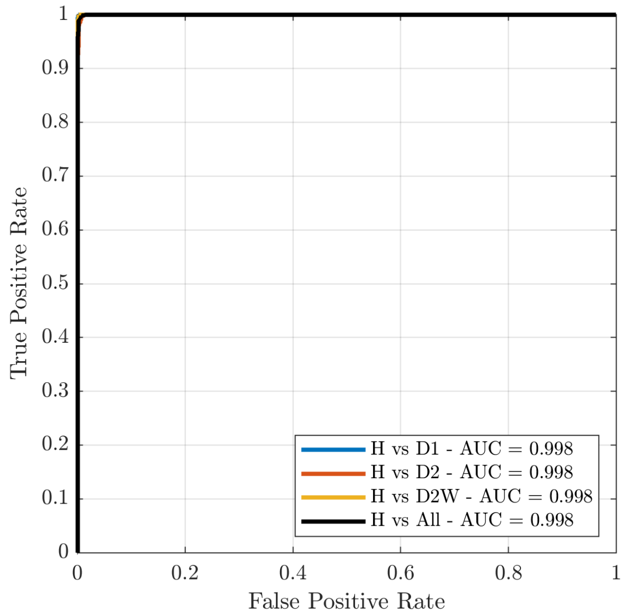

Figure 2.32: ROC curve to visualize the performance of the damage detection approach

Lastly, the AUC for the ROC curves are presented for clarification and to ease the comparative analysis of each method, Table 2.11. The ability to detect the damages is identical to the previous sections.

Cases	AUC [%]
Healthy versus Damage 1	99.8
Healthy versus Damage 2	99.8
Healthy versus Damage 2 with water	99.8
Healthy versus All	99.8

Table 2.11: AUC for the different cases. Healthy comprises the healthy state and the healthy state with water applied

2.3.4 No compensation

From a comparative perspective of the three latter methods for mitigating the effect of EOV, an approach without any compensation is implemented. Therefore, the AR coefficients for each dataset:

$$\boldsymbol{\Theta}_i = \begin{bmatrix} A_{1,1} & A_{1,2} & \dots & A_{1,4} & A_{2,1} & \dots & A_{n_a \cdot n_p, n_p} \end{bmatrix}^T \tag{2.30}$$

are gathered in a common DSF matrix containing the coefficients for all available datasets:

$$\boldsymbol{X} = \begin{bmatrix} \boldsymbol{\Theta}_1 & \boldsymbol{\Theta}_2 & \dots & \boldsymbol{\Theta}_i \end{bmatrix}^T \tag{2.31}$$

Subsequently, the squared Mahalanobis distance for each index of $\boldsymbol{X}$ is calculated using the mean value and covariance matrix obtained from the training data (healthy state and healthy state with water applied):

$$d^2(\boldsymbol{\Theta}_i, \hat{\boldsymbol{\Sigma}}_u) = (\boldsymbol{\Theta}_i - \boldsymbol{\mu}_*)^T \hat{\boldsymbol{\Sigma}}_u^{-1} (\boldsymbol{\Theta}_i - \boldsymbol{\mu}_*) \tag{2.32}$$

The squared Mahalanobis distances for all datasets are evaluated, Figure 2.33. Again, distinct clusters are observed indicating an acceptable damage detection performance.

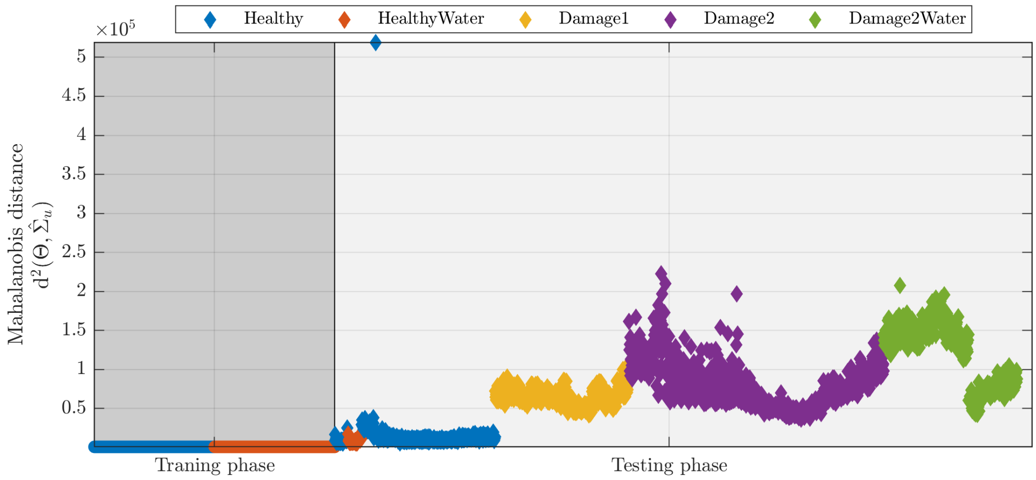

Figure 2.33: Squared Mahalanobis distances for the AR coefficients as DSF and the effect of EOV neglected

An analysis of the ability to detect the present damages is accomplished by the ROC curve where the probability of TP alarms versus the probability of FP alarms is visualized, Figure 2.34.

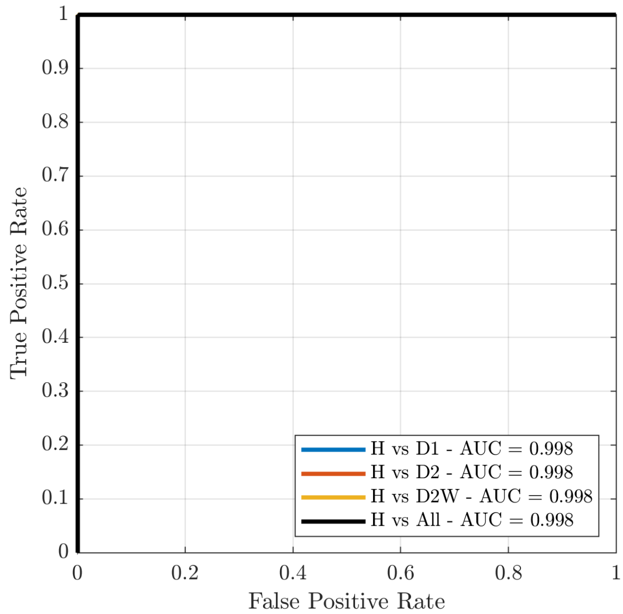

Figure 2.34: ROC curves for the different conditions of the blade versus the healthy state

A visual inspection of the ROC curve, Figure 2.34, states a well-functional damage detection technique towards the introduced damages. As a clarification, the AUC of the ROC curves are gathered and presented, Table 2.12.

Cases	AUC [%]
Healthy versus Damage 1	99.8
Healthy versus Damage 2	99.8
Healthy versus Damage 2 with water	99.8
Healthy versus All	99.8

Table 2.12: AUC for the different cases. Healthy comprises the healthy state and the healthy state with water applied

The performance for the explicit, the implicit and the combined method to mitigate the effect of EOV are identical to the approach with no compensation, at least concerning the first decimal of the AUC-values. A visual inspection of the ROC curves deduces that the explicit approach and the approach with no compensation should have the highest AUC value. At least if more decimals were used.

2.4 Overview

For further discussion, an overview of the previous results is gathered, Table 2.13. The table of results also serves as an easily accessible comparative analysis. An apparent observation of the table is the performance of detecting the damages with the use of AR coefficients as DSF. Independent of the method utilized to mitigate the effect of EOV, the performance is unchanged.

		H-D1	H-D2	H-D2w	H-All
Natural frequencies, $\hat{f}$	Explicit method	65.3%	67.3%	89.0%	72.2%
	Implicit method	58.9%	64.3%	86.4%	68.6%
	Combined method	68.5%	67.5%	89.4%	73.4%
	No compensation	66.3%	64.3%	89.1%	71.1%
Damping ratios, $\hat{\zeta}$	Explicit method	50.2%	48.6%	64.8%	53.1%
	Implicit method	48.4%	45.8%	55.5%	49.0%
	Combined method	49.5%	48.9%	66.2%	53.5%
	No compensation	48.1%	47.4%	63.1%	51.6%
AR coefficients, $\hat{\Theta}$	Explicit method	99.8%	99.8%	99.8%	99.8%
	Implicit method	99.8%	99.8%	99.8%	99.8%
	Combined method	99.8%	99.8%	99.8%	99.8%
	No compensation	99.8%	99.8%	99.8%	99.8%

Table 2.13: AUC of the ROC curves for the healthy versus all other conditions of the blade using the proposed features as DSF and different methods to mitigate the effect of EOV

Subsequently, with the presentation of the results, is only left to evaluate critically and compare each approach and outcome. These evaluations are carried out in the ensuing chapter.

Discussion

The division of the results into three main sections comprised of each DSF derives a similar split of the discussion. Therefore, the discussion will take part in three subsections comprised of each proposed DSF. In each subsection, the methods utilized to mitigate the effect of EOV are discussed. Lastly, a common discussion of the overall methodologies are conducted, Figure 3.1.

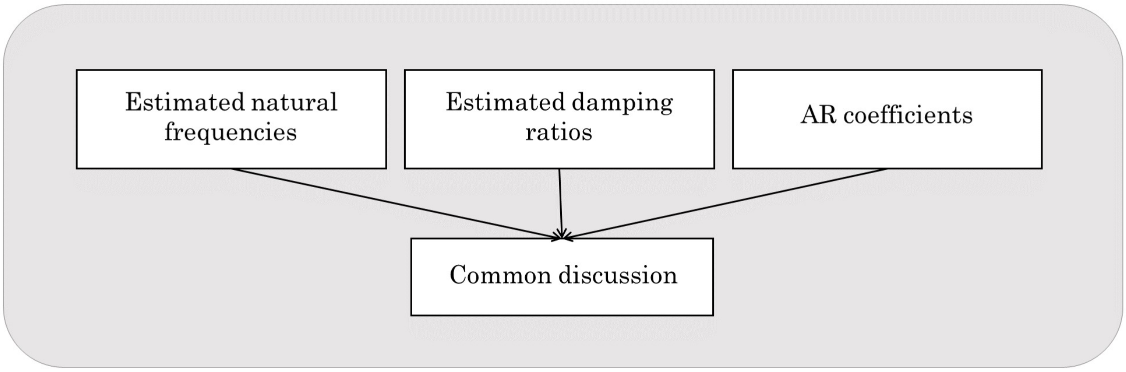

Figure 3.1: Flowchart of the division of the discussion

3.1 Natural frequencies

The estimated natural frequencies used for damage detection originate from VAR-models where the extracting process involves the Euclidean distance to a reference frequency. The reference frequencies are obtained in two main steps. First, the modes of interest are selected for a single dataset of the healthy state at $0°C$. This is accomplished by picking all possible resonances observed in the PSD of the specific dataset, Figure 1.7. These resonances are utilized as references to extract all possible modes of the VAR model. By an analysis of the mode shapes hereof, Figure 1.9, nine modes are selected which are assumed to be physical modes due to their behaviour. Next, reference models of the nine modes variability due to temperature changes in the training data are obtained by peak-picking in the PSD for each temperature setting in the range of $[-20°C; 4°C; 20°C]$. The variability is then traced by the use of Bayesian non-linear regression, Appendix A.1. These regression models comprise the reference frequencies. One disadvantage of using the Euclidean distance is the risk of extracting spurious modes with the belief of extracting physical modes. If the damaged state of the blade alters the estimated frequencies from the VAR model, a possibility that the Euclidean distance to the frequency of interest increases. Thereby, the frequency of interest may not be the one with the minimum distance anymore. Therefore, the estimated frequencies used as DSF might hold spurious modes following the trend of the reference frequencies instead of the trend of the damaged state. If so, it would decrease the ability to detect the damages. Therefore, an increment of the AUC-values is assumed if the accuracy of the estimated natural frequencies is increased. Such enhancement could be obtained by using reference mode shapes instead of reference frequencies, assumably. The reference mode shapes are given by the analysis in Section 1.2.1.2. Another possibility could be to extract stable poles in a range of model orders similar to the frequency stabilization plot, Figure 1.4. Yet this method increases the complexity significantly since the VAR-models should be calculated with increasing model orders instead of a single model order.

With the utility of the estimated frequencies as DSF, three methods to mitigate the effect of EOV are investigated. Additionally, a damage detection approach with no compensation is conducted as a reference. Generally, the explicit method to mitigate the effect of EOV increases the detectability. However, only a small increment is observed compared to the reference with no compensation. In Section 1.3.1.4 a variability in the estimated natural frequencies due to temperature changes is observed. Therefore, it was expected that the explicit approach should have had a higher performance of damage detection than observed since the regression models traced this trend with an accurate fit, Figure 2.2. If the squared Mahalanobis distances, Figure 2.3, are analyzed, the variance of the distances within each condition of the blade is significant. Significant variance within each condition might indicate high variance between the multivariate DSF vectors for each dataset. If the accuracy of the estimated natural frequencies is enhanced, the ability to detect damages should also improve.

The implicit approach to mitigate the effect of EOV was based on the PCA methodology. A decision of rejecting those PCs below a threshold of 90% of the total variance yielded the rejection of the first two PCs for each dataset. Since the data origins from an experimental setup, it is expected that the temperature changes account for most of the variability. Yet the advantage of following the PCA methodology to mitigate the effect of EOV is among others that any unknown EOPs (unknown comprise non-measured) are mitigated likewise the known EOPs. Despite this expected advantage, a decrease in the AUC-values is observed compared to the reference with no compensation. The aforementioned variance of the estimated natural frequencies should not decrease the AUC-values more than observed for the reference. Therefore, it might indicate that the first two PCs hold information concerning the damages. If so, that information has been lost due to the rejection part of the PCA methodology.

The contention of the first PCs holds information regarding the damaged state is the essence of the combined method. For the implicit approach of mitigating the influence of EOV, the first two PC was rejected. The rejection hereof worsens the performance of the damage detection. Following the combined methodology, a suggestion of lowering the threshold for the PCA methodology can be made. The fit of the regression models indicates which PCs are correlated to the effect of temperature changes. If the fit of the regression models is analyzed, Figure 2.8, the first PC is highly correlated with the temperature as the only PC reasoned by a high R^2 value. Therefore, a presumption of increased AUC-values if only the first PC is rejected following the PCA methodology appears to be valid. Succeeding the proposed combined method all nine PCs are adjusted according to the respective regression model. Despite the same high variance for the squared Mahalanobis distances within the conditions of the blade, Figure 2.9, the AUC-values are elevated. Therefore, some information regarding damages must be held by the first PCs.

3.2 Damping ratios

As discussed in the previous section, Section 3.1, the process of extracting the modal parameters might conflict with the presumption of rejecting spurious modes. Moreover, statements of the complicated aspects associated with the estimation of damping insinuate the usage of damping ratios as DSF can be arduous. Significant variance in three out of nine estimated damping ratios shown are observed, Figure 1.14. The vast amount of outliers due to the high variance affects the regression models to some extent leading to poor compensation. Yet the performance of the damage detection approach when the temperature changes are explicitly compensated does not differ significantly from the approach with no compensation. This indicates either that the estimated damping ratios are not influenced by the temperature changes or that the regression models do not trace the trend sufficiently. Due to the high variance observed, it is most likely the regression models do not trace the trend. Additionally, the high variance observed in the estimated damping ratios is also present in the squared Mahalanobis distances, Figure 2.14. In the latter section, the explicit compensation while using the estimated natural frequencies showed acceptable functionality. Therefore, the poor detectability using the estimated damping ratios as DSF and explicitly compensating for the temperature changes seems to be caused by poor estimates.

To implicitly compensate for the effect of EOV, the PCA methodology is pursued with the rejection of those PCs that are below the 90% threshold of the cumulative variance plot. The rejection process led to the rejection of seven out of nine PCs. With only two PCs for each dataset the squared Mahalanobis distances showed no distinct clusters of the conditions, Figure 2.17. Observably, the same amount of variance for the explicit compensation approach is present even with some increment. Analyzing the ROC curves and the associated AUC-values indicates an unsuitable technique for damage detection since the probability of TP and FP alarms is nearly equal, Figure 2.18. Moreover, lower values of the AUC compared to both the reference approach and the explicit compensation approach are noticed. The reduced AUC-values indicate some information about the damages is removed in the rejection process of the PCs. A similar assumption was made in the latter section. However, it is assumed that the detectability will increase if more accurate estimates of the damping ratios can be conducted.

The statement of some information regarding the damages being lost in the process of rejecting PCs is endorsed by analyzing the proposed combined methodology while using the estimated damping ratios. The regression models of the nine PCs have a poor fit indicated by a low R^2 value and low F-statistics. Furthermore, the F-statistics of the validation data are below one. It is arguable whether or not the null hypothesis can be rejected when the F-statistics of the validation data are below one. Yet the null hypothesis is chosen to be rejected since high variance were present in the estimated damping ratios leading to poor fits of the PCs, assumably. The fit of the regression model of the first PC appears to have a minor increment yielding some dependency towards the temperature changes. Therefore, lowering the threshold of the PCA methodology to implicitly mitigate the effect of EOV might improve the ability to detect damages. The usage of the proposed combined method to mitigate the influence of EOV did show the best performance in detecting the introduced damages, yet unsuitable due to AUC-values near 50%. However, the improvement using the combined method where all PCs are included provides some validation for the statement regarding the loss of information about the damages following the PCA methodology.

3.3 AR coefficients

The two aforementioned sections are based on building a damage detection approach using modal parameters as DSF, namely the estimated natural frequencies and estimated damping ratios. The estimation of natural frequencies and damping ratios origins from a VAR-model of each dataset. Prior to the eigenvalue decomposition, Equation (1.16), the AR coefficients are determined and utilized for the eigenvalue decomposition through a state space representation. Therefore, the information regarding the damages held by the estimated modal parameters was expected not to be any greater than the information held by the AR coefficients. Thus an expectation of improved ability to detect damages using the AR coefficients as DSF appeared correctly. The expectation is fulfilled if the damage detection approach with no compensation regarding the effect of EOV is analyzed, Table 2.13. Despite the approach with no compensation yielded high AUC-values, it was still investigated whether or not the explicit, implicit, or combined method to mitigate the influence of EOV could increase the AUC-values. However, no significant improvements were observed. Still, different observations of interest were conducted, clarified in the following discussion.

Pursuing the proposed explicit method to mitigate the effect of temperature changes led to the acceptance of 178 regression models out of 1040 possible, Figure 2.24. The majority of the coefficients rejected their regression model, which can be caused for several reasons. One possible cause could be that the majority of the coefficients are insensitive towards temperature changes. However, this is assumed to be incorrect since some affecting is observed in the squared Mahalanobis distances of the reference with no compensation, 2.33. The presentation of the squared Mahalanobis distances is sorted from the lowest temperature to the highest for each group. Another possibility is that the coefficients comprise noise or other variability which cannot be predicted by regression models where the temperature is utilized as input. The statement of some of the coefficients comprise noise and other variability inexplicable by the temperature appears reasonable. Reasonableness originates from analyzing the implicit and combined approach to mitigate the effect of EOV. The last 92 PCs were rejected by the assumption of containing noise. This removal is assumed to cause the more levelled trends observed, Figure 2.28 and 2.31. Therefore, it is assumed that the rejection of the majority of the regression models was due to variability inexplicable by the temperature changes. If the squared Mahalanobis distances of the explicit approach, Figure 2.25, are compared to the distances of the reference approach no distinct difference is observed. Consequently, the effect of the explicit compensation might have been of minor importance. However, for the healthy testing state, some increased variance is observed. The majority of the healthy testing state originates from the temperatures in between the training data, namely in the temperature range of $[-18°C; 4°C; 18°C]$. Therefore, this increased variance can be caused by the regression models. The regression models are trained with the use of temperatures different from the healthy testing data. Therefore, some unseen tendency in the testing data might have been compensated poorly.

The PCA methodology to implicit mitigate the effect of EOV resulted in the rejection of the first 83 PCs due to the assumption of bearing most of the variability caused by EOV. Furthermore, the last 92 PCs were also rejected with the assumption of containing noise mostly. Leaving 617 PCs for each dataset the squared Mahalanobis distances, Figure 2.28, are observably more levelled as those of the reference approach, Figure 2.33. The more levelled trends can be caused by two possibilities. Either the rejection of the first 83 PCs which are assumed to bear the effect of EOV or the rejection of the last 92 PCs which are assumed to bear noise mostly. Since most of the regression models were rejected in the explicit approach, it seems reasonable to assume that the levelled trends originate from the removal of noise. Following the PCA methodology to implicit mitigate the effect of EOV did show acceptable effectiveness. Yet, some affecting due to the temperature is still observed in the squared Mahalanobis distances. However, distinct clusters are present using the squared Mahalanobis distance for simple classification. Therefore, the performance of the damage detection approach is acceptably high yet similar to the reference approach with no compensation.

The implicit approach to mitigate the effect of EOV yielded highly accurate damage detection similar to the explicit approach and the reference. Since the proposed combined method showed an increased ability to detect damages while using the modal parameters as DSF, it was expected to perform similarly using the AR coefficients as DSF. The adopted regression models contribute 27 out of 792 where mainly the first PCs accepted their regression model, Figure 2.30. The first few PCs adopted the regression models with both high fit and confidence in terms of high R^2 value and F-statistics. Therefore, the first PCs are assumed to have some correlation with the temperature changes. Despite the inclusion of all PCs, some adjusted by regression models, the squared Mahalanobis distances, Figure 2.31, are similar to those obtained by the PCA methodology. Due to the similarity, the cause of levelling trends origins from the assumption of noise held by the last 92 PCs.

The use of the AR coefficients as DSF proved to be applicable. Furthermore, the statement of damage information held by the modal parameters is no greater than the information held by the coefficients shown to be valid. The AUC-values for the different proposed methods to mitigate the effect of EOV are equal, at least to the first decimal, Table 2.13. The high-performance damage detecting approach independent of the method to mitigate the effect of EOV might be caused by the simplicity of the setup. If the introduced damages are significant enough to be detected independent of the influence caused by temperature changes, equal performances independent of the different methods to mitigate the effect of EOV will be present. Furthermore, most of the variability is caused by temperature changes different from an operational environment where many parameters constitute the variability. Thus, the effect of mitigating the influence of EOV should be more significant than the approach with no compensation.

3.4 Common discussion

An individual discussion regarding each choice of DSF and the proposed methods to mitigate the effect of EOV derived different observations yet also some mutual observations. Prior to the conclusion the mutually shared observations are emphasized and discussed.

The increased performance in detecting damages using the proposed combined implicit-explicit method is mutually shared, except while using the AR coefficients. The assumed risk regarding rejecting information concerning damages following the PCA methodology where the first PCs are rejected appears reasonable. The reasonableness is endorsed by adjusting the first PCs according to their adopted regression model and included in the damage detecting approach. The endorsement origins from the increased AUC-values. Moreover, a comparative analysis of the combined method, the explicit approach and the implicit approach proved the assumed functionality of the combined method. Throughout the comparative analysis, a proposal of lowering the threshold of the total variance utilized for the rejection of PCs is assumed to improve the PCA methodology. The proposal is attributed to the revelation of fewer PCs adopted their regression model than the PCA methodology rejected.

A single significant outlier is observed in the squared Mahalanobis distances while using the AR coefficients as DSF, Figure 2.25, 2.28, 2.31 and 2.33. Such outliers can rather easily be removed since the distance of the outlier is greater than the clustering observed. Therefore, such outliers should be removed to increase the detectability. The main objective of removing outliers before damage detection is mutually shared with the estimation of natural frequencies, damping ratios and AR coefficients, Figure 1.15, 1.17 and 1.16. The utilization of Bayesian non-linear regression was with the assumption of being less prone to outliers. Yet some proneness is observed, especially for the estimated damping ratio of the first bending mode shown. Therefore, it is ought to assume the accuracy of the regression models would increase if outliers are removed before training. Regression models affected by outliers do not solely trace the trend of the environmental parameters used as input, namely the temperature. Therefore, the explicit compensation is assumed to improve if possible outliers are removed.

Independent of the choice of DSF distinct variations in the AUC-values between the different approaches to mitigate the effect of EOV is not present, Table 2.13. In general, the difference is within 4% variation. Whether or not the minor improvement is of specific relevance is arguable. Yet the observations during the investigation and the comparative analysis of the methods to mitigate the influence of EOV are advantageous. Especially the main proposition of the combined method where some PCs are adjusted according to the adopted regression models instead of being rejected as the PCA methodology proposes. Furthermore, the study is based on experimental data where the temperature is controlled and constitutes the main variability. Operating wind turbines are affected by numerous parameters, some measured and some not. With the presence of multiple measured parameters, the regression models should be built as multiple non-linear regression to trace the observed trend in the output. Consequently, the outcome might be altered relative to this study. However, the functionality of the combined method is still believed to be superior. The belief is based on the observation regarding the first PCs held information useful to detect the damages.

The choice of suitable DSF for this setup is the AR coefficients, indisputably. As discussed, the estimation of accurate modal parameters can be challenging and time-consuming. The awareness of improved damage detection if the accuracy of the estimated modal parameters is increased does not obscure the easy accessibility of the AR coefficients. Furthermore, the AR coefficients showed high sensitivity towards the damages while minor affection of temperature changes since the damage detection with no compensation showed great performance. Different observations might be observed in an operational environment. Yet the belief of the AR coefficients being highly applicable to detect damages is maintained.

Conclusion

Through a thorough state of the art investigation, the physical quantities utilized as DSF comprised estimations of the natural frequencies and damping ratios. These modal parameters were estimated by *Vector Auto-Regressive* (VAR) models due to the alleged accuracy in the former study. Furthermore, non-physical quantities utilized as DSF comprised the AR coefficients of the VAR models. These physical and non-physical DSFs were investigated with three different EOV compensation methodologies, an explicit, implicit and a joint implicit/explicit methodology. The explicit methodology was based on Bayesian non-linear regression utilizing the temperature changes as input. Regression models were trained and used for compensation if accepted. The acceptance was derived from a sufficient high F-statistic. The implicit methodology followed the *Principle Component Analysis* (PCA) methodology to implicit mitigate the effect of EOV. The mitigation process was to transform the DSF into a new set of coordinates, *Principle Components* (PCs). The effect of EOV was removed by introducing a threshold to reject the first PCs since the first PCs bear most of the variability, assumably. Lastly, the combined implicit-explicit approach aimed to explicit compensate the PCs utilizing Bayesian non-linear regression. In this sense, no PCs were rejected. A comparative analysis against an uncompensated approach was conducted for each of the three DSFs. The analysis constituted the framework for selecting a suitable DSF with an effective mitigation methodology. The effectiveness was measured in terms of the rate of correctly detected damages with various thresholds (*True Positive Rate* (TPR)). The TPR of the three mentioned approaches to mitigate the effect of EOV are presented in Table 3.1.

	Natural frequencies, $\hat{f}$	Damping ratios, $\hat{\zeta}$	AR coefficients, $\hat{\Theta}$
Explicit method	72.2%	53.1%	99.8%
Implicit method	68.6%	49.0%	99.8%
Combined method	73.4%	53.5%	99.8%
No compensation	71.1%	51.6%	99.8%

Table 3.1: TPR for each method to mitigate the effect of EOV. The classification is either the healthy state or any other damaged state.

Independent of the mitigation methodology utilized, the choice of AR coefficient as DSF did proved to be superior. The estimated damping ratios was associated with high variance. The high variance obscured the damaged states to an undetectable extent. Therefore, the estimated damping ratios are unsuitable in the context of a damage detection algorithm. The estimated natural frequencies did showed reasonable applicability for an damage detection algorithm. However, improved estimates can be crucial to establish an well-functional SHM system.

The comparative analysis regarding the proposed mitigation methodologies led to several findings. The decreased TPR of the implicit method were found to originate from the rejection of too many PCs. The combined method accepted fewer regression models than the PCA methodology rejected, proving fewer PCs being correlated to temperature changes than rejected. Therefore, the reliability of the PCA methodology heavily depends on the rejection process. The dependency complicates the process of mitigating the effect of EOV without compromising the level of detected damages. These conflicting aspects were overcome utilizing the combined method. The usability was proved to be superior with beneficial TPR. The minor difference between the explicit method and the combined method was expected to be caused by the consequence of the controlled environment. In the controlled environment, the temperature changes account for most of the variability. The disadvantages of the explicit method should be manifested by the presence of many unmeasured EOPs since no compensation hereof can be conducted. Differently, the otherwise rejected PCs of the PCA methodology can to some extent be compensated using those EOP(s) available to enhance the mitigation process of the PCA methodology. Thus enhancing the ability to detect damages and validating the essence of the combined implicit-explicit method.

The utilization of the combined implicit-explicit method to mitigate the influence of EOV proved to be the most efficient method among the methods investigated. Therefore, the proposed SHM system employed to detect the introduced damages in this setup should involve the combined implicit-explicit method to mitigate the present effect of EOV. Additionally, the choice of DSF should be based on parameters originating from a parametric representation of the signal; the AR coefficients in this study. The choice is based on easy accessibility and high damage sensitivity. The utility of modal parameters as DSF did not show any superiority. The lack of superiority is due to the information utilized to detect damages held by the extracted modal parameters being no greater than the information held by the parameters of the parametric method. Furthermore, the process of extracting the modal parameters of a parametric model involves several time-consuming processes.

The proposed SHM system for this setup is accompanied by several possible improvements which remained for further study. The combined implicit-explicit methodology utilize Bayesian non-linear regression models. These regression models were trained and used to compensate those PCs which accepted their regression model. If the basis of the regression models is improved, the compensation process is improved, allegedly. Suggested improvement is among others the choice of polynomial order and the presumed behaviour of $\boldsymbol{Y}$ in Equation (1.29). The polynomial order was fixed at a chosen value during the training phase. Training the regression models with different polynomial orders dependent on which AR coefficient constitutes the output could yield an improvement. The assumed behaviour of the AR coefficients is modelled as a global polynomial tendency. These polynomials are then based on Legendre polynomials for stability. Another approach could be to assume local behaviours utilizing splines. Generally, global tendencies were observed in the AR coefficients, Figure 1.13. However, some regions of the AR coefficients could have a local tendency. If so, splines are expected to improve the regression models.

Remarks

Due to the origination of the data from a controlled environment, the outcome of this study is likely to be altered in an operational environment. Considerations regarding the adaptability of the proposed methods for the existence of multiple known EOPs were discussed yielding several remarks. Mainly, the regression models using Bayesian non-linear regression should be altered into multiple Bayesian non-linear regression since multiple inputs can be present. The polynomial expression in Equation (1.29) should be written into the following assuming a global polynomial tendency:

$$\boldsymbol{Y} = \beta_0 + \beta_1 \boldsymbol{X}_1 + \beta_2 \boldsymbol{X}_2 + \ldots + \beta_n \boldsymbol{X}_n + \beta_{n+1} \boldsymbol{X}_1^2 + \beta_{n+2} \boldsymbol{X}_2^2 + \ldots + \beta_{p \cdot n} \boldsymbol{X}_n^p \tag{3.1}$$

Where:

$n =$ Number of EOPs
$p =$ Polynomial order

The efficiency of using the explicit method to mitigate the effect of measured EOPs is assumed to be dependent on the level of inexplicable variability. The efficiency is expected to decrease as the level of inexplicable variability increases since the essence of the explicit method is to mitigate variability caused by measured EOP(s). With a significant level of inexplicable variability, which is assumed to occur in an operational environment, an implicit method to mitigate the effect of EOV is assumed to be advantageous. Yet the risk of rejecting information about damages while following an implicit procedure like the PCA methodology is prevailing, based upon the observations throughout this study. Consequently, the superior efficiency of the proposed combined implicit-explicit methodology is believed to exist. Yet the rejection of some of the first PCs might still be necessary depending on the level of inexplicable variability.

As the amount of EOPs increases the complexity regarding estimating the modal parameters is assumed to increase. The modal parameters can be obscured by the effect of EOV, increasing this complexity. This support the usage of the parameters from a parameterized representation of the signal as DSF instead of the modal parameters. A similar conclusion is deduced for this study. Throughout this study with the usage of coefficients originating from VAR-models as DSF the effect of the proposed methods to mitigate the influence of EOV was absent. As discussed, the severity of the damages introduced is of high enough level to be detected properly or is not obscured by the temperature changes to an undetectable extent, allegedly. However, the effect of the proposed methods to mitigate the influence of EOV might be measured by analyzing the squared Mahalanobis distances. First by comparing the distance between the healthy state and damaged states. Then by comparing the scattering of each condition. The scattering of each condition is assumed to increase in an operational environment, which should inflict the TPR. Therefore, the high TPR is assumed to decrease in an operational environment. Additionally, the effect of the proposed methods to mitigate the influence of EOV is assumed to be more profound.

Bibliography

[1] Casper Aaskov Drangsfeldt. *Automated Modal Analysis of an airfoil*. preprint. Dec. 15, 2022. DOI: 10.31224/2735. URL: https://engrxiv.org/preprint/view/2735/version/3932 (visited on 12/16/2022).

[2] I. Antoniadou et al. "Aspects of structural health and condition monitoring of offshore wind turbines". In: *Philosophical Transactions of the Royal Society A: Mathematical, Physical and Engineering Sciences* 373.2035 (Feb. 28, 2015), p. 20140075. ISSN: 1364-503X, 1471-2962. DOI: 10.1098/rsta.2014.0075. URL: https://royalsocietypublish org/doi/10.1098/rsta.2014.0075 (visited on 12/05/2022).

[3] Luis David Avendaño-Valencia. *Parametric time-series methods for identification of LTI systems*. (Visited on 05/18/2022).

[4] Luis David Avendaño-Valencia, Eleni N. Chatzi, and Dmitri Tcherniak. "Gaussian process models for mitigation of operational variability in the structural health monitoring of wind turbines". In: *Mechanical Systems and Signal Processing* 142 (Aug. 2020), p. 106686. ISSN: 08883270. DOI: 10.1016/j.ymssp.2020.106686. URL: https://linkinghub.elsevier.com/retrieve/pii/S0888327020300728 (visited on 10/24/2022).

[5] Anela Bajrić, Jan Høgsberg, and Finn Rüdinger. "Evaluation of damping estimates by automated Operational Modal Analysis for offshore wind turbine tower vibrations". In: *Renewable Energy* 116 (Feb. 2018), pp. 153–163. ISSN: 09601481. DOI: 10.1016/j.renene.2017.03.043. URL: https://linkinghub.elsevier.com/retrieve/pii/S0960148117302355 (visited on 11/16/2022).

[6] Andrea Bellavia. *Statistical Methods for Environmental Mixtures*. www.bookdown.org. Nov. 18, 2021. URL: https://bookdown.org/andreabellavia/mixtures/principal-component-analysis.html (visited on 11/18/2022).

[7] Anders Brandt. *Noise and vibration analysis: signal analysis and experimental procedures*. OCLC: ocn664324149. Chichester: Wiley, 2011. 438 pp. ISBN: 978-0-470-74644-8.

[8] Rune Brincker and Carlos Ventura. *Introduction to operational modal analysis*. Chichester, West Sussex: John Wiley and Sons, Inc, 2015. 1 p. ISBN: 978-1-118-53515-8 978-1-118-53516-5.

[9] M S Cao et al. “Structural damage identification using damping: a compendium of uses and features”. In: *Smart Materials and Structures* 26.4 (Apr. 1, 2017), p. 043001. ISSN: 0964-1726, 1361-665X. DOI: 10.1088/1361-665X/aa550a. URL: https://iopscience.iop.org/article/10.1088/1361-665X/aa550a (visited on 11/16/2022).

[10] Kartik Chandrasekhar et al. “Damage detection in operational wind turbine blades using a new approach based on machine learning”. In: *Renewable Energy* 168 (May 2021), pp. 1249–1264. ISSN: 09601481. DOI: 10.1016/j.renene.2020.12.119. URL: https://linkinghub.elsevier.com/retrieve/pii/S0960148120320590 (visited on 05/05/2022).

[11] Kai-Chun Chang and Chul-Woo Kim. “Modal-parameter identification and vibration-based damage detection of a damaged steel truss bridge”. In: *Engineering Structures* 122 (Sept. 2016), pp. 156–173. ISSN: 01410296. DOI: 10.1016/j.engstruct.2016.04.057. URL: https://linkinghub.elsevier.com/retrieve/pii/S0141029616301845 (visited on 11/07/2022).

[12] Shashank Chauhan, A Phillips, and R Allemang. “Damping Estimation using Operational Modal Analysis”. In: *Conference Proceedings of the Society for Experimental Mechanics Series* (Jan. 1, 2008).

[13] E. J. Cross et al. “Features for damage detection with insensitivity to environmental and operational variations”. In: *Proceedings of the Royal Society A: Mathematical, Physical and Engineering Sciences* 468.2148 (Dec. 8, 2012), pp. 4098–4122. ISSN: 1364-5021, 1471-2946. DOI: 10.1098/rspa.2012.0031. URL: https://royalsocietypublishing.org/doi/10.1098/rspa.2012.0031 (visited on 12/05/2022).

[14] R.O. Curadelli et al. “Damage detection by means of structural damping identification”. In: *Engineering Structures* 30.12 (Dec. 2008), pp. 3497–3504. ISSN: 01410296. DOI: 10.1016/j.engstruct.2008.05.024. URL: https://linkinghub.elsevier.com/retrieve/pii/S014102960800206X (visited on 12/02/2022).

[15] C. R. Farrar and K. Worden. *Structural health monitoring: a machine learning perspective*. Chichester, West Sussex, U.K. ; Hoboken, N.J: Wiley, 2013. 631 pp. ISBN: 978-1-119-99433-6.

[16] Siemens Gamesa. *The winds of change have never been stronger*. www.siemensgamesa.com. URL: https://www.siemensgamesa.com/products-and-services/offshore (visited on 12/05/2022).

[17] David García Cava et al. “On Explicit and Implicit Procedures to Mitigate Environmental and Operational Variabilities in Data-Driven Structural Health Monitoring”. In: *Structural Health Monitoring Based on Data Science Techniques*. Ed. by Alexandre Cury et al. Vol. 21. Series Title: Structural Integrity. Cham: Springer International Publishing, 2022, pp. 309–330. ISBN: 978-3-030-81715-2 978-3-030-81716-9. DOI: 10.1007/978-3-

030-81716-9_15. URL: https://link.springer.com/10.1007/978-3-030-81716-9_15 (visited on 10/25/2022).

[18] A. Gómez González and S.D. Fassois. “A supervised vibration-based statistical methodology for damage detection under varying environmental conditions & its laboratory assessment with a scale wind turbine blade”. In: *Journal of Sound and Vibration* 366 (Mar. 2016), pp. 484–500. ISSN: 0022460X. DOI: 10.1016/j.jsv.2015.11.018. URL: https://linkinghub.elsevier.com/retrieve/pii/S0022460X15009153 (visited on 10/27/2022).

[19] J.B. Hansen et al. “A new scenario-based approach to damage detection using operational modal parameter estimates”. In: *Mechanical Systems and Signal Processing* 94 (Sept. 2017), pp. 359–373. ISSN: 08883270. DOI: 10.1016/j.ymssp.2017.03.007. URL: https://linkinghub.elsevier.com/retrieve/pii/S0888327017301206 (visited on 11/16/2022).

[20] Gareth James et al. *An Introduction to Statistical Learning: with Applications in R*. Springer Texts in Statistics. New York, NY: Springer US, 2021. ISBN: 978-1-07-161417-4 978-1-07-161418-1. DOI: 10.1007/978-1-0716-1418-1. URL: https://link.springer.com/10.1007/978-1-0716-1418-1 (visited on 11/14/2022).

[21] Erwin Kreyszig, Herbert Kreyszig, and E. J. Norminton. *Advanced engineering mathematics*. 10th ed. Hoboken, NJ: John Wiley, 2011. 1 p. ISBN: 978-0-470-45836-5.

[22] Fatma Nur Kudu et al. “Estimation of damping ratios of steel structures by Operational Modal Analysis method”. In: *Journal of Constructional Steel Research* 112 (Sept. 2015), pp. 61–68. ISSN: 0143974X. DOI: 10.1016/j.jcsr.2015.04.019. URL: https://linkinghub.elsevier.com/retrieve/pii/S0143974X15001339 (visited on 11/16/2022).

[23] MATLAB. *damp*. https://se.mathworks.com. URL: https://se.mathworks.com/help/ident/ref/lti.damp.html (visited on 11/17/2022).

[24] Suzi Mein. *Wind Farm Maintenance Planning*. URL: https://www.firetrace.com/fire-protection-blog/wind-farm-maintenance (visited on 04/24/2022).

[25] Alexander Mendler, Michael Döhler, and Carlos E. Ventura. “A reliability-based approach to determine the minimum detectable damage for statistical damage detection”. In: *Mechanical Systems and Signal Processing* 154 (June 2021), p. 107561. ISSN: 08883270. DOI: 10.1016/j.ymssp.2020.107561. URL: https://linkinghub.elsevier.com/retrieve/pii/S088832702030947X (visited on 12/06/2022).

[26] Peter Moser and Babak Moaveni. “Environmental effects on the identified natural frequencies of the Dowling Hall Footbridge”. In: *Mechanical Systems and Signal Processing* 25.7 (Oct. 2011), pp. 2336–2357. ISSN: 08883270. DOI: 10.1016/j.ymssp.

2011.03.005. URL: https://linkinghub.elsevier.com/retrieve/pii/S0888327011001233 (visited on 11/16/2022).

[27] Carlo Rainieri and Filipe Magalhaes. “Challenging aspects in removing the influence of environmental factors on modal parameter estimates”. In: *Procedia Engineering* 199 (2017), pp. 2244–2249. ISSN: 18777058. DOI: 10.1016/j.proeng.2017.09.210. URL: https://linkinghub.elsevier.com/retrieve/pii/S187770581733658 (visited on 10/25/2022).

[28] Zhengru Ren et al. “Offshore wind turbine operations and maintenance: A state-of-the-art review”. In: *Renewable and Sustainable Energy Reviews* 144 (July 2021), p. 110886. ISSN: 13640321. DOI: 10.1016/j.rser.2021.110886. URL: https://linkinghub.elsevier.com/retrieve/pii/S1364032121001805 (visited on 12/05/2022).

[29] Koushik Roy, Bishakh Bhattacharya, and Samit Ray-Chaudhuri. “ARX model-based damage sensitive features for structural damage localization using output-only measurements”. In: *Journal of Sound and Vibration* 349 (Aug. 2015), pp. 99–122. ISSN: 0022460X. DOI: 10.1016/j.jsv.2015.03.038. URL: https://linkinghub.elsevier.com/retrieve/pii/S0022460X15002771 (visited on 10/26/2022).

[30] Matti Scheu et al. “Maintenance Strategies for Large Offshore Wind Farms”. In: *Energy Procedia* 24 (2012), pp. 281–288. ISSN: 18766102. DOI: 10.1016/j.egypro.2012.06.110. URL: https://linkinghub.elsevier.com/retrieve/pii/S1876610212011502 (visited on 12/06/2022).

[31] Chathurangi Shyalika. *Understanding Principal Components Analysis(PCA)*. medium.datadriveninvesto May 24, 2019. URL: https://medium.datadriveninvestor.com/principal-components-analysis-pca-71cc9d43d9fb (visited on 11/09/2022).

[32] Hoon Sohn. “Effects of environmental and operational variability on structural health monitoring”. In: *Philosophical Transactions of the Royal Society A: Mathematical, Physical and Engineering Sciences* 365.1851 (Feb. 15, 2007), pp. 539–560. ISSN: 1364-503X, 1471-2962. DOI: 10.1098/rsta.2006.1935. URL: https://royalsocietypublishing.org/doi/10.1098/rsta.2006.1935 (visited on 12/05/2022).

[33] Wikipedia. *Bayesian Linear Regression*. en.wikipedia.org. URL: https://en.wikipedia.org/wiki/Bayesian_linear_regression (visited on 10/20/2022).

[34] Wikipedia. *Ordinary Least Square*. en.wikipedia.org. URL: https://en.wikipedia.org/wiki/Ordinary_least_squares (visited on 10/20/2022).

[35] Mingqiang Xu et al. “Structural damage detection using low-rank matrix approximation and cointegration analysis”. In: *Engineering Structures* 267 (Sept. 2022), p. 114677. ISSN: 01410296. DOI: 10.1016/j.engstruct.2022.114677. URL: https://linkinghub.elsevier.com/retrieve/pii/S0141029622007714 (visited on 11/16/2022).

[36] A.-M. Yan et al. “Structural damage diagnosis under varying environmental conditions—Part I: A linear analysis”. In: *Mechanical Systems and Signal Processing* 19.4 (July 2005), pp. 847–864. ISSN: 08883270. DOI: 10.1016/j.ymssp.2004.12.002. URL: https://linkinghub.elsevier.com/retrieve/pii/S0888327004001785 (visited on 11/16/2022).

Appendix

A.1 Natural frequency references

For each of the nine modes of interest, Table 1.4, peak-picking in the PSD for each temperature setting have been conducted. The main objective is to trace the variability caused by temperature changes to have a suitable reference. A suitable reference should increase the estimates of natural frequencies from the VAR-models. Figure A.1 illustrate the peak-picked frequencies and Figure A.2 illustrates the traced variability.

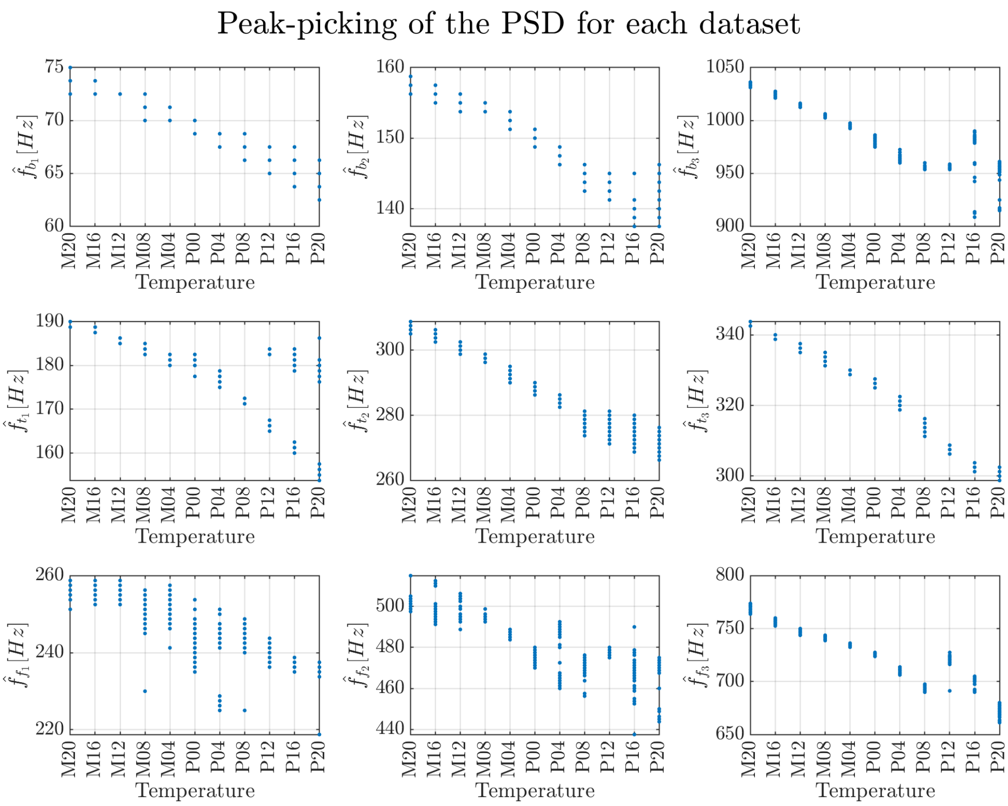

Figure A.1: Peak-picked frequencies from the PSD

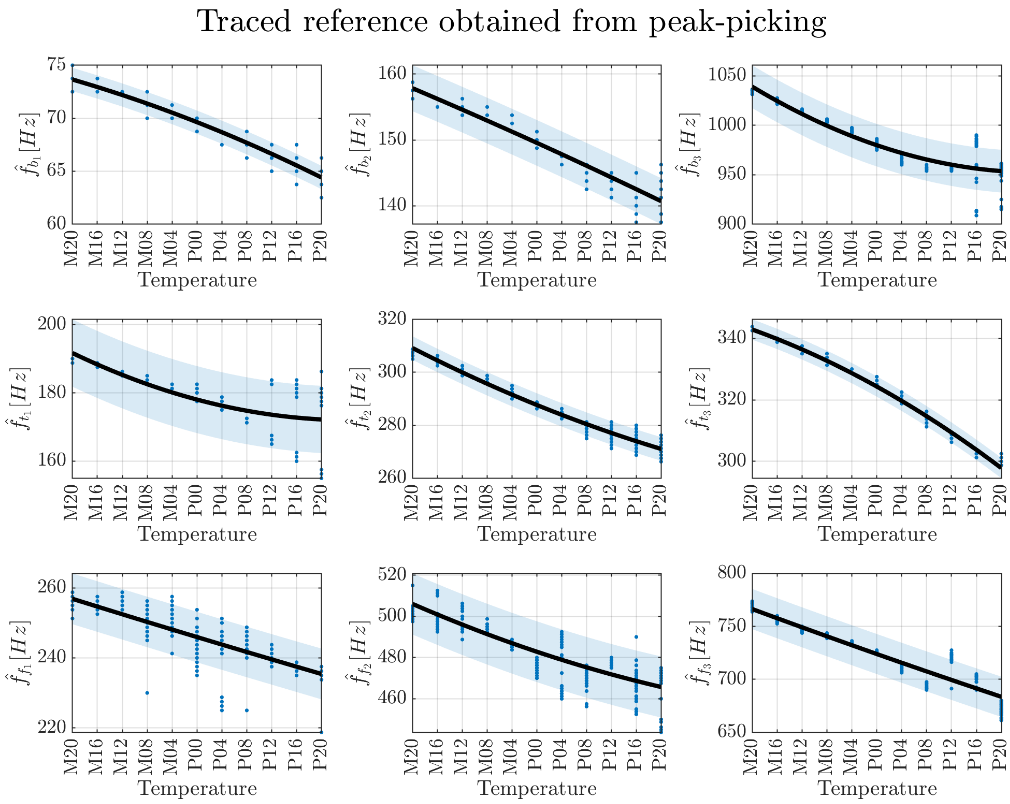

Figure A.2: Traced trend in the peak-picked frequencies from the PSD

A.2 Estimated natural frequencies

Nine estimated natural frequencies extracted from the VAR-models are utilized as DSF. To ease the presentation in the study only three have been shown. This is due to the three shown showing the same tendency as all nine. Yet the presentation of all nine estimated frequencies can be conducted, and is shown in Figure A.3. Furthermore, the traced variability using Bayesian non-linear regression models with the temperature as input is shown in Figure A.4.

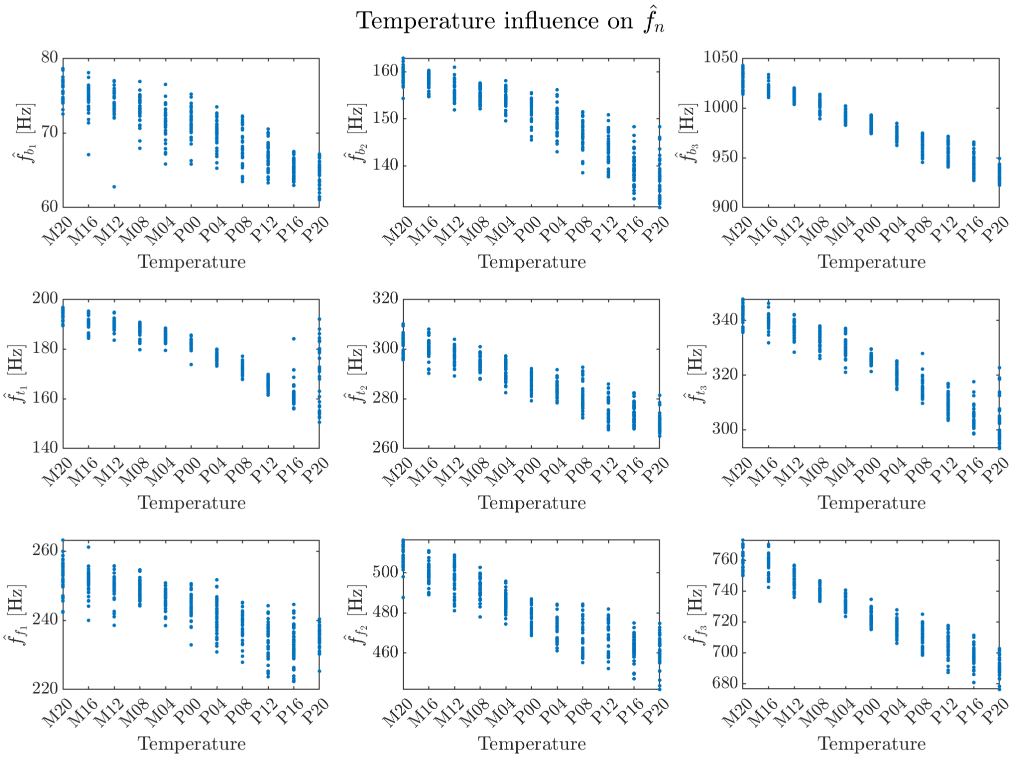

Figure A.3: Temperature influence on the estimated natural frequencies

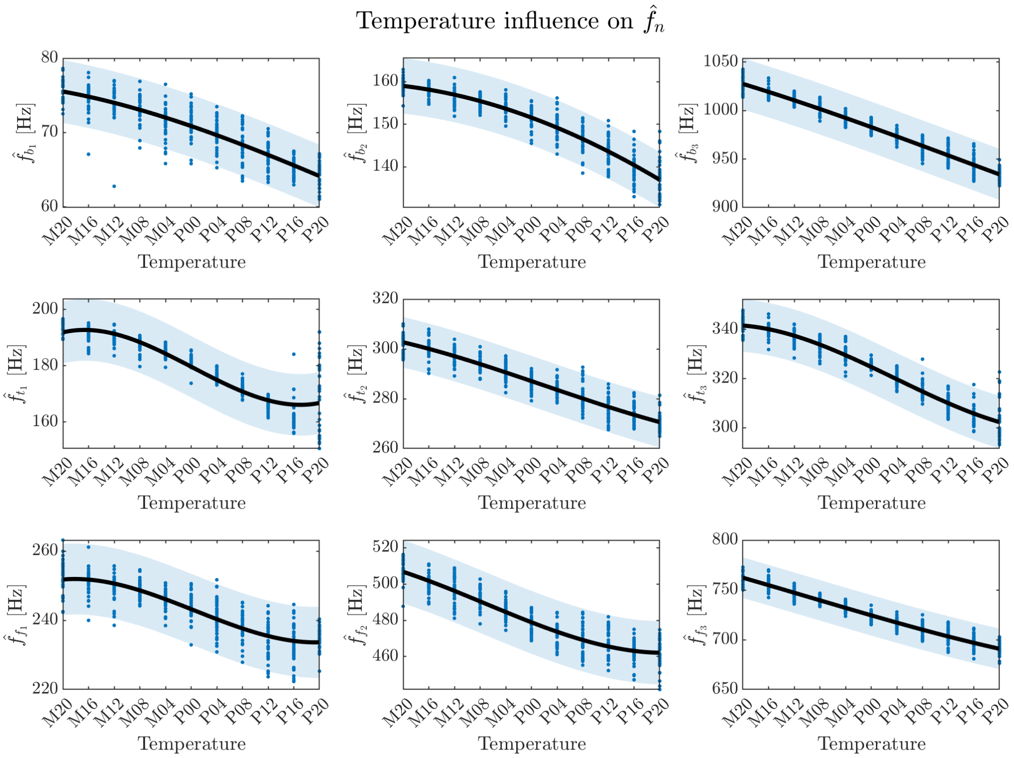

Figure A.4: Training regression models to capture the temperature influence on the estimated natural frequencies

A.3 Estimated damping ratios

The process of extracting the modal parameters of the VAR-models is based on the minimum distance to a reference frequency and then extracting that mode. Therefore, the associated damping ratios to the estimated natural frequencies in Figure A.3 are presented in Figure A.5. Furthermore, the traced variability due to temperature changes is traced using Bayesian non-linear regression models, Figure A.6.

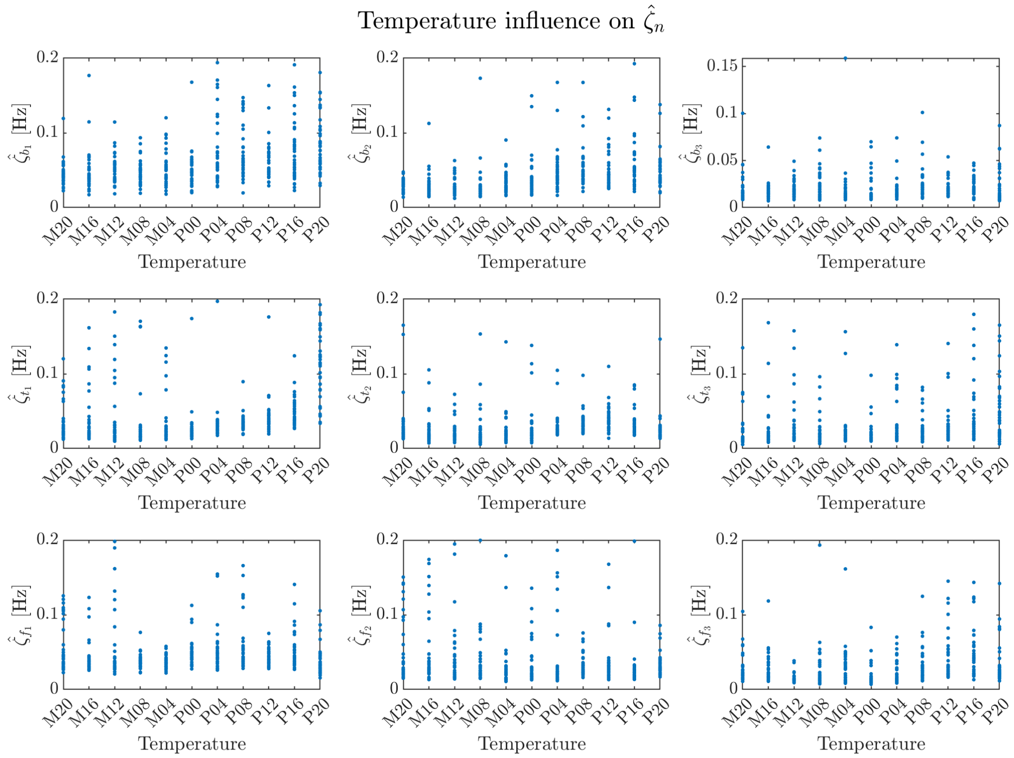

Figure A.5: Temperature influence on the estimated damping ratios

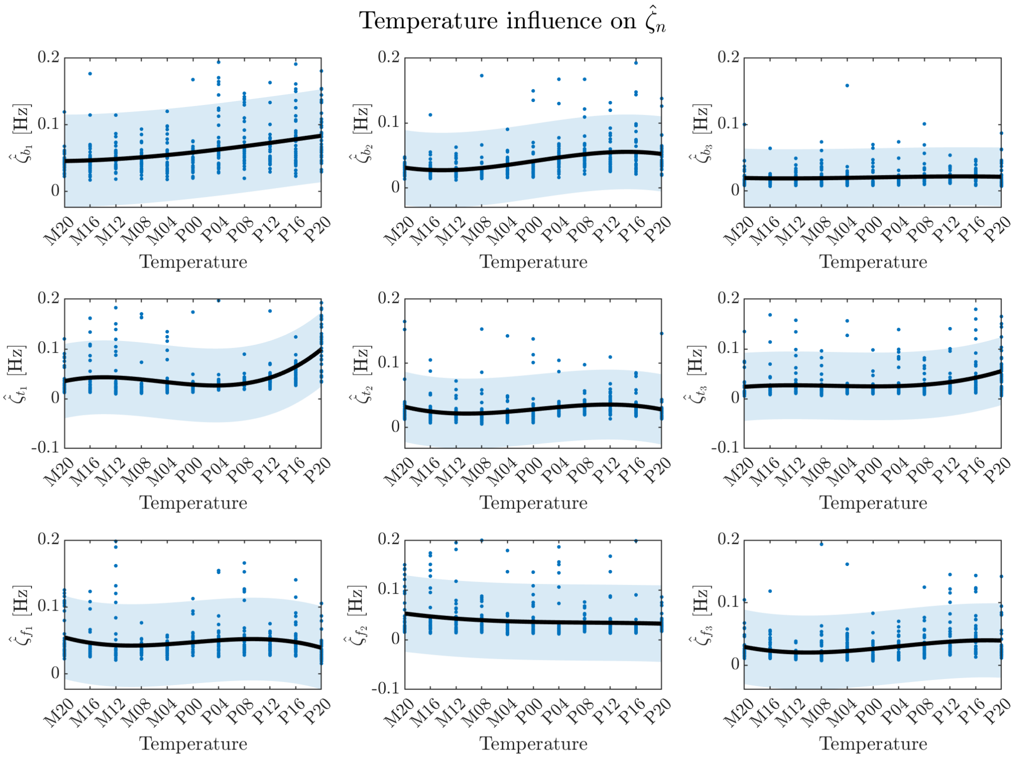

Figure A.6: Training regression models to capture the temperature influence on the estimated damping ratios

A.4 Estimated natural frequencies as DSF

To determine the polynomial order of the regression models to trace the variability caused by temperature changes sufficiently, the MSE for increasing order is analyzed. The MSE is analyzed for each of the nine estimated natural frequencies of PCs hereof. Yet, due to simplicity, only the most distinct MSE for increasing order are shown, Figure A.7 and A.8. The MSE not shown contained the same tendency. Therefore, the approach for choosing a sufficient polynomial order is assumed to be valid.

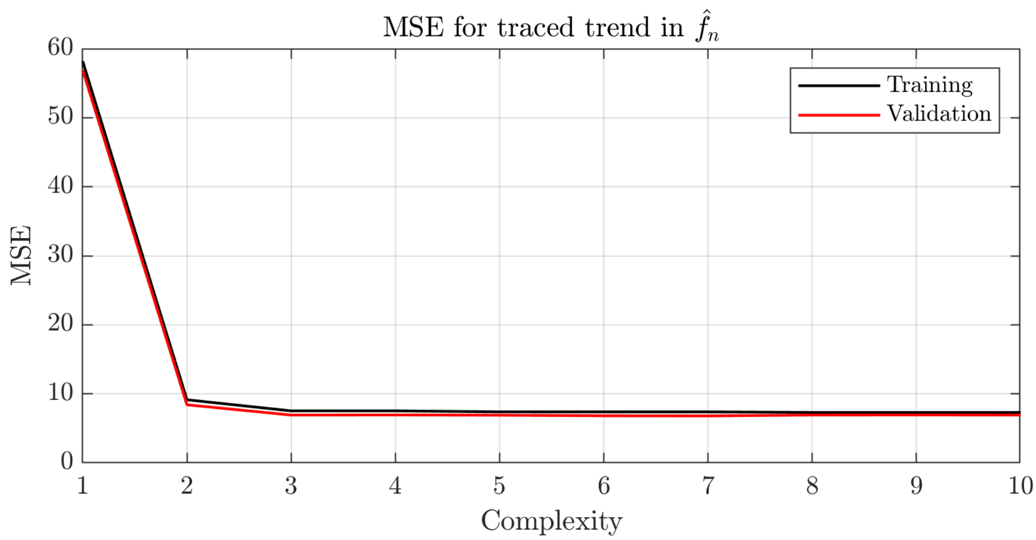

Figure A.7: MSE of the estimated natural frequencies at different polynomial orders

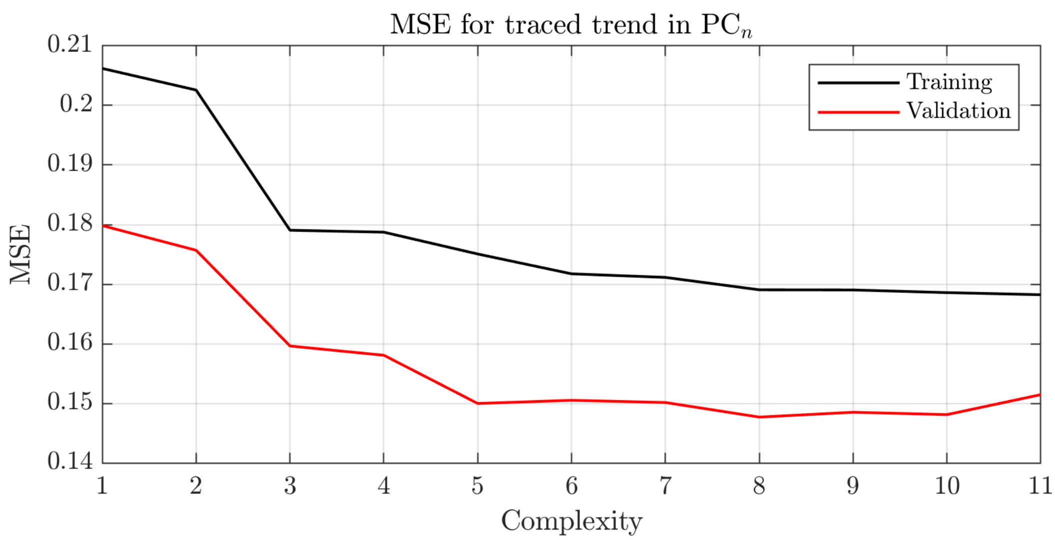

Figure A.8: MSE of the PCs obtained from transformations of the estimated natural frequencies

A.5 Estimated damping ratios as DSF

A similar approach as in Section A.4 is utilized for the damping ratios. The polynomial order is chosen by analyzing the MSE of increasing order for each of the estimated damping ratios or PCs hereof. The most distinct MSE for increasing order is shown for the damping ratio and the PC hereof, Figure A.9 and A.10.

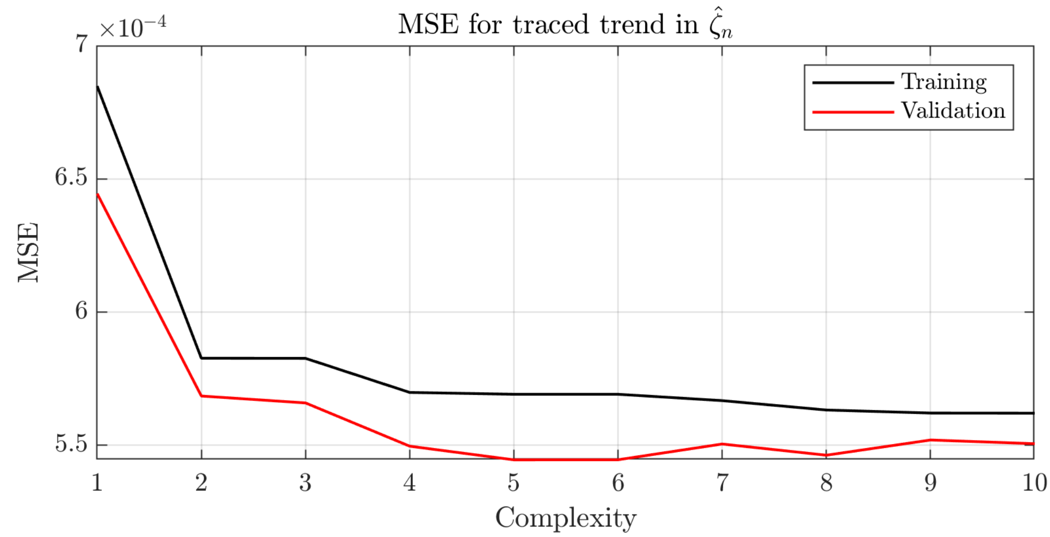

Figure A.9: MSE of the estimated damping ratios at increasing polynomial order

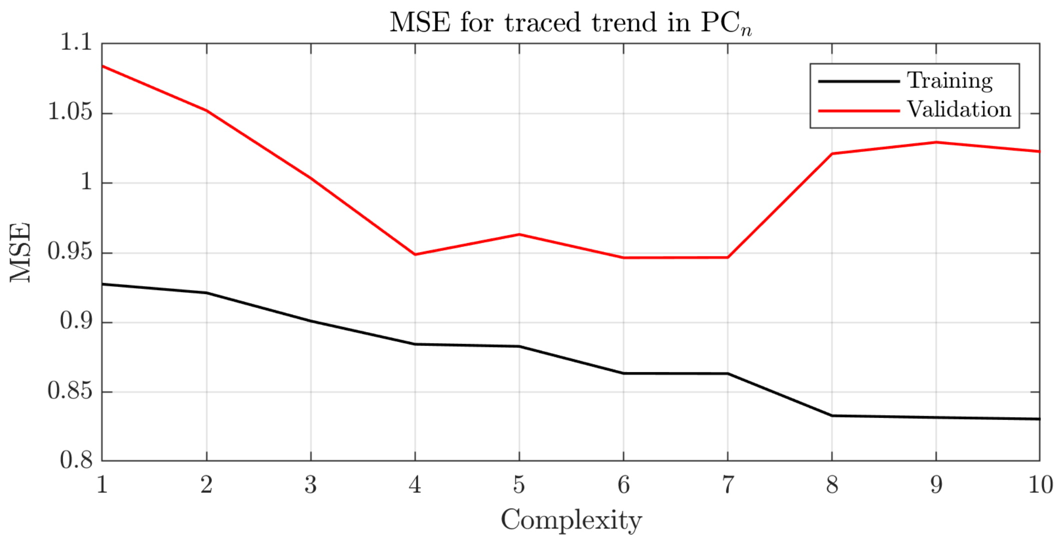

Figure A.10: MSE of the PCs obtained from a transformation of the estimated damping ratios

A.6 Estimated AR coefficients as DSF

The approach for choosing a suitable polynomial order utilized in Section A.4 and A.5 are adopted to choose a polynomial order to trace the variability in the AR coefficients. Due to the vast amount of AR coefficients, the MSE for increasing order is not analyzed for all coefficients. The most profound MSE for increasing model order is shown in Figure A.11 and is used to choose the polynomial order. The polynomial order of the PCs of the coefficients is chosen from Figure A.12.

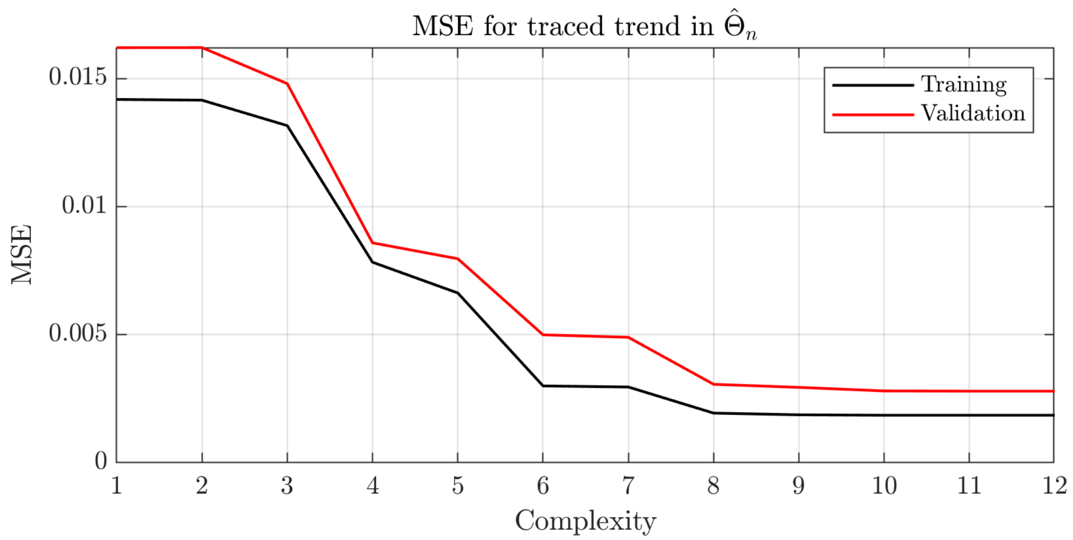

Figure A.11: MSE of the estimate AR coefficients at increasing polynomial order.

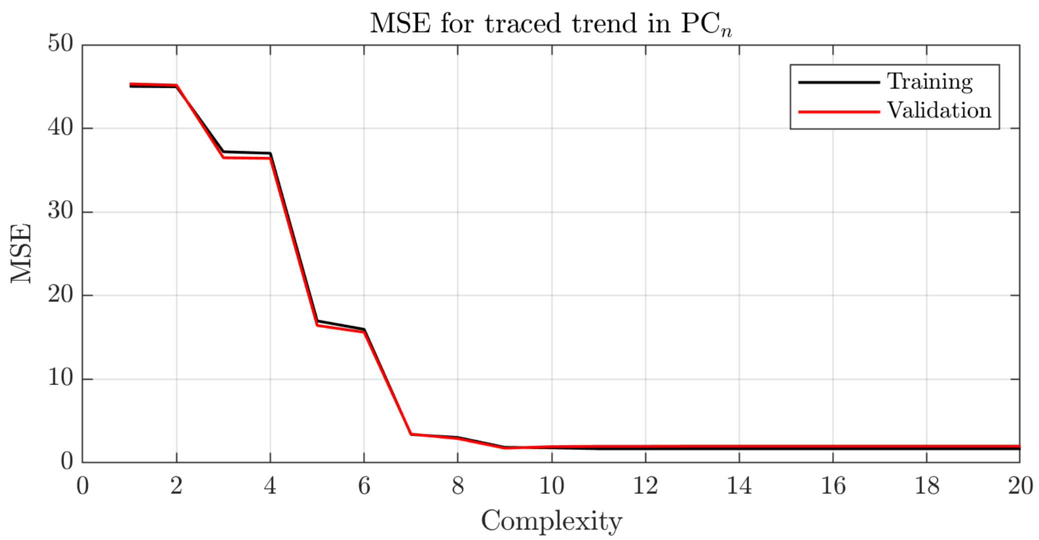

Figure A.12: MSE of the PCs that are obtained from the estimated AR coefficients. MSE for increasing polynomial order to deduce a suitable order